

## **Copyright Warning & Restrictions**

The copyright law of the United States (Title 17, United States Code) governs the making of photocopies or other reproductions of copyrighted material.

Under certain conditions specified in the law, libraries and archives are authorized to furnish a photocopy or other reproduction. One of these specified conditions is that the photocopy or reproduction is not to be “used for any purpose other than private study, scholarship, or research.” If a user makes a request for, or later uses, a photocopy or reproduction for purposes in excess of “fair use” that user may be liable for copyright infringement,

This institution reserves the right to refuse to accept a copying order if, in its judgment, fulfillment of the order would involve violation of copyright law.

**Please Note: The author retains the copyright while the New Jersey Institute of Technology reserves the right to distribute this thesis or dissertation**

Printing note: If you do not wish to print this page, then select “Pages from: first page # to: last page #” on the print dialog screen

The Van Houten library has removed some of the personal information and all signatures from the approval page and biographical sketches of theses and dissertations in order to protect the identity of NJIT graduates and faculty.

## **ABSTRACT**

### **STRUCTURAL HEALTH MONITORING OF BRIDGES USING WIRELESS SENSOR NETWORKS**

**by**  
**Seyed Behrad Ghazi Sharyatpanahi**

Structural Health Monitoring, damage detection and localization of bridges using Wireless Sensor Networks (WSN) are studied in this thesis. The continuous monitoring of bridges to detect damage is a very useful tools for preventing unnecessary costly and emergent maintenance. The optimal design aims to maximize the lifetime of the system, the accuracy of the sensed data, and the system reliability, and to minimize the system cost and complexity.

Finite Element Analysis (FEA) is carried out using LUSAS Bridge Plus software to determine sensor locations and measurement types and effectively minimize the number of sensors, data for transmission, and volume of data for processing. In order to verify the computer simulation outputs and evaluate the proposed optimal design and algorithms, a WSN system mounted on a simple reinforced concrete frame model is employed in the lab. A series of tests are carried out on the reinforced concrete frame mounted on the shaking table in order to simulate the existing extreme loading condition. Experimental methods which are based on modal analysis under ambient vibrational excitation are often employed to detect structural damages of mechanical systems, many of such frequency domain methods as first step use a Fast Fourier Transform estimate of the Power Spectral Density (PSD) associated with the response of the system. In this study it is also shown that higher order statistical estimators such as Spectral Kurtosis (SK) and Sample to Model Ratio (SMR) may be successfully employed to more reliably

discriminate the response of the system against the ambient noise and better identify and separate contributions from closely spaced individual modes. Subsequently, the identified modal parameters are used for damage detection and Structural Health Monitoring.

To evaluate the preliminary results of the project's prototype and quantify the current bridge response as well as demonstrate the ability of the SHM system to successfully perform on a bridge, the deployment of Wireless Sensor Networks in an existing highway bridge in Qatar is implemented. The proposed technique will eventually be applied to the new stadium that State of Qatar will build in preparation for the 2022 World Cup. This monitoring system will help permanently record the vibration levels reached in all substructures during each event to evaluate the actual health state of the stadiums. This offers the opportunity to detect potentially dangerous situations before they become critical.

**STRUCTURAL HEALTH MONITORING OF BRIDGES  
USING WIRELESS SENSOR NETWORKS**

**by  
Seyed Behrad Ghazi Sharyatpanahi**

**A Thesis  
Submitted to the Faculty of  
New Jersey Institute of Technology  
in Partial Fulfillment of the Requirements for the Degree of  
Master of Science in Civil Engineering**

**John A. Reif Jr. Department of Civil and Environmental Engineering**

**May 2015**

Blank Page

**APPROVAL PAGE**

**STRUCTURAL HEALTH MONITORING OF BRIDGES  
USING WIRELESS SENSOR NETWORKS**

**Seyed Behrad Ghazi Sharyatpanahi**

---

Dr. Mohamad Ala Saadeghvaziri, Thesis Advisor  
Professor of Civil and Environmental Engineering, NJIT

Date

---

Dr. Mohamed Mahgoub, Thesis Co-Advisor  
Associate Professor of Engineering Technology, NJIT

Date

---

Dr. Sunil Saigal, Committee Member  
Distinguished Professor of Civil and Environmental Engineering, NJIT

Date

## **BIOGRAPHICAL SKETCH**

**Author:** Seyed Behrad Ghazi Sharyatpanahi

**Degree:** Master of Science

**Date:** May 2015

### **Undergraduate and Graduate Education:**

- Master of Science in Civil Engineering,  
New Jersey Institute of Technology, Newark, NJ, 2015
- Bachelor of Science in Civil Engineering,  
University of Tehran, Tehran, Iran, 2012

**Major:** Civil Engineering

### **Presentations and Publications:**

G.M. Nita, M. Mahgoub, S. Sharyatpanahi, N. Cretu, T. M. El-Fouly, “Higher Order Statistical Frequency Domain Decomposition for Operational Modal Analysis,” 7<sup>th</sup> International Conference on Structural Health Monitoring of Intelligent Infrastructure, Torino, Italy, July 2015.



## **DEDICATION**

I dedicate this thesis work to my family. A special feeling of gratitude to my loving parents, Zia and Manzar whose words of encouragement and push for tenacity ring in my ears. My sister Vardnoosh has never left my side and is very special. I could not have accomplished as much as I have without their support and understanding. Words cannot describe how much I love and appreciate you.

## ACKNOWLEDGMENT

I would like to thank all the people who contributed in some way to the work described in this thesis. First and foremost, I thank my thesis advisors, Dr. Mohamad Ala Saadeghvaziri and Dr. Mohamed Mahgoub, for giving me intellectual freedom in my work, engaging me in new ideas, and demanding a high quality of work in all my endeavors. I am grateful to Dr. Mahgoub for his help since the beginning of the research project and his friendly and supportive environment in which to conduct the coursework. I appreciate the valuable suggestions from Dr. Saadeghvaziri and his guidance in the analytical aspects of the work during the research project. Without their guidance, support and patience I would not have been able to reach this stage.

Additionally, I would like to thank my committee member Professor Sunil Saigal for his interest in my work, support, suggestions, and motivation. When I took the Applied Finite Element Methods course, he was a great help in finite element modeling of bridges.

I was fortunate to have the chance to work with Dr. Gelu M. Nita, who patiently taught me his method for Higher Order Statistical Frequency Domain Decomposition for Operational Modal Analysis, and worked closely with me in the damage identification method I present in this thesis. He was an extremely reliable source of practical scientific knowledge.

Special thanks to Tarek Elfouly and Dr. Khaled Abdulsaid from Qatar University for providing me data of the shaking table for my research. I also would like to thank Maher Abdelghani for providing public open access to the experimental data used in this

study ([ftp://ftp.esat.kuleuven.be/pub/SISTA/data/mechanical/flexible\\_structure.dat.gz](ftp://ftp.esat.kuleuven.be/pub/SISTA/data/mechanical/flexible_structure.dat.gz)).

This research was made possible by NPRP 6-150-2-0597 grant from the Qatar National Research Fund (a member of The Qatar Foundation).

Last but not least, I'd like to express my deepest gratitude to my parents and friends who have always encouraged and supported me over so many years. Your encouragement has been greatly appreciated.

## TABLE OF CONTENTS

Chapter	Page
1 INTRODUCTION.....	1
1.1 Structural Health Monitoring .....	1
1.2 Vibration Based Damage Detection Strategy .....	4
1.3 Operational Modal Analysis .....	6
1.4 Research Objectives .....	10
1.5 Thesis Overview .....	11
2 FINITE ELEMENT ANALYSIS .....	13
2.1 Introduction .....	13
2.2 Lusas Bridge Software .....	13
2.3 Analysis of a Reinforced Concrete Frame .....	18
2.3.1 Modeling Description .....	19
2.3.2 Natural Frequency Analysis Results .....	26
2.4 Analysis of 3-Span Concrete Box Beam Bridge of Varying Section .....	31
2.4.1 Bridge Description .....	31
2.4.2 Modeling Description .....	32
2.4.3 Moving Load Analysis .....	39
2.4.4 Seismic Response Analysis .....	41
2.4.5 Natural Frequency Analysis Results .....	43
2.4.6 Moving Load Analysis Results .....	49
2.4.7 Seismic Response Analysis results .....	53

**TABLE OF CONTENTS**  
**(Continued)**

<b>Chapter</b>	<b>Page</b>
2.5 Analysis of 6-Span Precast Segmental Box Girder Bridge .....	55
2.5.1 Description of the Bridge .....	55
2.5.2 Modeling Description .....	58
2.5.3 Geometry .....	58
2.5.4 Material .....	67
2.5.5 Defining the Loads.....	68
2.5.6 Analysis Results .....	72
2.5.7 Natural Frequency Analysis Results .....	77
2.6 Conclusions .....	82
3 EXPERIMENTAL WORK .....	83
3.1 Introduction .....	83
3.2 Reinforced Concrete Frame .....	83
3.3 Experiment Setup .....	85
3.3.1 Shaking Table .....	86
3.3.2 Measurement Sensors .....	80
3.4 Experimental Results .....	91
3.5 Conclusions .....	93
4 IMPLEMENTATION OF HEALTH MONITORING SYSTEM ON AN IN-SERVICE HIGHWAY BRIDGE .....	95
4.1 Introduction .....	95
4.2 Structural Health Monitoring Systems .....	97

**TABLE OF CONTENTS**  
**(Continued)**

<b>Chapter</b>	<b>Page</b>
4.3 Sensors and Sensing Technology .....	99
4.3.1 Wind Measurement Sensors .....	100
4.3.2 Seismic Sensors .....	100
4.3.3 Weigh-in-motion Stations .....	101
4.3.4 Thermometers .....	101
4.3.5 Strain Gauges .....	102
4.3.6 Displacement Measurement Sensors .....	104
4.3.7 Accelerometers .....	105
4.3.8 Weather Stations .....	106
4.3.9 Fiber Optic Sensors .....	106
4.4 Wireless Sensors and Wireless Monitoring .....	108
4.4.1 Basic Architectures and Features of Wireless Sensors .....	110
4.4.2 Sustainable Operation of the Wireless Sensor Network .....	112
4.5 The Structural Health Monitoring System of an In-service Highway Bridge ....	116
4.5.1 Accelerometers .....	116
4.5.2 Strain Gauges .....	117
4.5.3 Temperature Sensors .....	118
4.5.5 Weigh-in-motion (WIM) Stations .....	119
4.5 Conclusions .....	119
5 OPERATIONAL MODAL ANALYSIS .....	121

**TABLE OF CONTENTS**  
**(Continued)**

<b>Chapter</b>	<b>Page</b>
5.1 Fundamentals of Operational Modal Analysis .....	121
5.2 Basic Concepts of Stationary Random Data and Processes .....	123
5.2.1 Spectral Density Functions .....	125
5.2.2 Fundamentals of Matrix Algebra .....	130
5.2.3 Inverse Problems .....	134
5.3 Classification of OMA Techniques .....	139
5.4 Operational Modal Analysis in the Frequency Domain .....	140
5.4.1 The Basic Frequency Domain (Peak-Picking) Method .....	140
5.4.2 The (Enhanced) Frequency Domain Decomposition .....	144
5.5 Spectral Kurtosis Estimation of Harmonic Excitations .....	149
5.5.1 Theoretical Background .....	149
5.5.2 The Experimental Data Set .....	153
5.5.3 Data Analysis .....	160
5.6 A Maximum Likelihood Curve Fitting Method for Frequency Domain Decomposition .....	164
5.6.1 Theoretical Background .....	164
5.6.2 Algorithm Implementation and Validation .....	168
5.7 Conclusions .....	172
6 CONCLUSIONS AND FUTURE WORK .....	174
6.1 Conclusions .....	174
6.2 Recommendations for Future Work .....	176

**TABLE OF CONTENTS**  
**(Continued)**

<b>Chapter</b>	<b>Page</b>
APPENDIX A CONSTRUCTION OF REINFORCED CONCRETE FRAME .....	178
APPENDIX B CHARACTERISTICS OF THE IRIS MOTE PLATFORMS AND THE MEASUREMENT SENSORS EMBEDDED IN THE MTS400 CROSSBOW BOARD.....	180
APPENDIX C 1940 EL CENTRO EARTHQUAKE RECORD .....	183
REFERENCES .....	184



## LIST OF TABLES

<b>Table</b>	<b>Page</b>
2.1 Options Available in Lusas Bridge Plus Software .....	14
2.2 Design Material Properties .....	19
2.3 3D Flat Thin Shell Elements TTS3 Description .....	21
2.4 3D Thick Beam Element BTS3 Description.....	22
2.5 Modal Frequencies of RC frame .....	30
2.6 Modal Frequencies of Concrete Box Section .....	48
2.7 3D Solid Continuum Elements TH4 and PN6 description .....	66
2.8 Modal Frequencies of Concrete Box Section .....	81
3.1 M437A Shaker Properties .....	87
3.2 BT500M Slip Table Properties .....	88
3.3 Characteristics of Microaccelerometer ADXL202 .....	90
4.1 Major Bridges Equipped with Health Monitoring Systems .....	96
5.1 Comparison Between the Modal Parameters .....	172
B.1 Technical Specifications of the IRIS mote platforms .....	180
B.2 Characteristics of the Humidity and Temperature Sensor .....	181
B.3 Characteristics of the Barometric Pressure and Temperature Sensor .....	181
B.4 Characteristics of the Light Sensor .....	181
B.5 Characteristics of the Accelerometer Sensor .....	182

## LIST OF FIGURES

<b>Figure</b>	<b>Page</b>
2.1 The investigated RC Frame .....	18
2.2 Position of steel reinforcement in RC Frame .....	18
2.3 RC Frame geometry defined in Lusas .....	20
2.4 RC Frame supports.....	20
2.5 Geometric properties of the reinforcement for beam element .....	22
2.6 Mesh Reinforcement Bars and Mesh Properties .....	23
2.7 Mesh Concrete and Mesh Properties.....	24
2.8 Steel material properties.....	25
2.9 Concrete elastic and plastic properties.....	25
2.10 Eigenvalue Controls.....	26
2.11 The 1 <sup>st</sup> mode shape .....	27
2.12 The 2 <sup>nd</sup> mode shape .....	27
2.13 The 3 <sup>rd</sup> mode shape .....	28
2.14 The 4 <sup>th</sup> mode shape .....	28
2.15 The 5 <sup>th</sup> mode shape .....	28
2.16 The 6 <sup>th</sup> mode shape .....	29
2.17 The 7 <sup>th</sup> mode shape .....	29
2.18 The 8 <sup>th</sup> mode shape .....	29
2.19 The 9 <sup>th</sup> mode shape .....	30
2.20 The 10 <sup>th</sup> mode shape .....	30

**LIST OF FIGURES**  
**(Continued)**

<b>Figure</b>	<b>Page</b>
2.21 3-Span Concrete Box Beam bridge .....	31
2.22 Elevation and cross sections of the bridge .....	32
2.23 Geometric lines and supports of the varying section bridge .....	33
2.24 Concrete material properties .....	33
2.25 Voided span section properties .....	34
2.26 Voided intermediate section properties.....	34
2.27 Properties of the voided section adjacent to the pier .....	35
2.28 Solid span section properties .....	35
2.29 Solid pier section properties.....	36
2.30 Column section properties .....	36
2.31 Multiple varying section line properties for the Left Span .....	37
2.32 Multiple varying section line properties for the Right Span .....	37
2.33 Multiple varying section line properties for the Centre Span.....	38
2.34 Damaged section properties .....	38
2.35 Location of the damage .....	39
2.36 Eigenvalue controls .....	39
2.37 HS-20 truck load .....	40
2.38 IMDPlus modal force properties .....	40
2.39 IMDPlus moving load analysis control .....	41
2.40 IMDPlus Seismic Analysis control dialog .....	42

**LIST OF FIGURES**  
**(Continued)**

<b>Figure</b>	<b>Page</b>
2.41 IMDPlus Seismic output control .....	42
2.42 The 1 <sup>st</sup> mode shape .....	43
2.43 The 2 <sup>nd</sup> mode shape .....	44
2.44 The 3 <sup>rd</sup> mode shape .....	44
2.45 The 4 <sup>th</sup> mode shape .....	45
2.46 The 5 <sup>th</sup> mode shape .....	45
2.47 The 6 <sup>th</sup> mode shape .....	46
2.48 The 7 <sup>th</sup> mode shape .....	46
2.49 The 8 <sup>th</sup> mode shape .....	47
2.50 The 9 <sup>th</sup> mode shape .....	47
2.51 The 10 <sup>th</sup> mode shape .....	48
2.52 Displacement time history of the mid-span for truck speed of 15 m/s .....	49
2.53 Acceleration of the mid-span for truck speed of 15 m/s .....	49
2.54 Peak vertical displacement response of the mid-span .....	50
2.55 Peak vertical acceleration response of the mid-span .....	50
2.56 Displacement time history of the mid-span for truck speed of 15 m/s .....	51
2.57 Acceleration of the mid-span for truck speed of 15 m/s .....	51
2.58 Peak vertical displacement response of the mid-span .....	52
2.59 Peak vertical acceleration response of the mid-span .....	52
2.60 Displacement time history of the mid-span under El Centro earthquake .....	53

**LIST OF FIGURES**  
**(Continued)**

<b>Figure</b>	<b>Page</b>
2.61 Peak displacements output .....	54
2.62 Aerial Photo of the bridge .....	55
2.63 Side view of the bridge.....	56
2.64 Geometry of the bridge.....	57
2.65 Precast Segmental Box Girder Bridge modeled in Lusas Bridge Plus software...	59
2.66 Properties of A_A section adjacent to the abutments .....	60
2.67 Voided B_B section properties .....	60
2.68 Voided C_C section properties .....	61
2.69 Voided D_D section properties .....	61
2.70 Solid section properties at abutments .....	62
2.71 Solid section properties at piers .....	62
2.72 Varying section of the bridge .....	63
2.73 Multiple varying section line properties for 5th span .....	64
2.74 Multiple varying section line properties for 5th span .....	64
2.75 Bridge piers geometry .....	65
2.76 Bridge piers Mesh .....	66
2.77 Typical uniaxial compressive and tensile stress-strain curve for concrete .....	67
2.78 Concrete material properties .....	68
2.79 AASHTO LRFD design lane load description .....	69
2.80 AASHTO LRFD design lane load applied to the bridge model .....	69

**LIST OF FIGURES**  
**(Continued)**

<b>Figure</b>	<b>Page</b>
2.81 Moving load generator .....	70
2.82 AASHTO LRFD HS-20 truck load .....	70
2.83 Moving HS-20 truck on the bridge FE model .....	71
2.84 Eigenvalue controls .....	71
2.85 Deformed mesh under gravity Load .....	72
2.86 Deformed mesh under Lane Load .....	72
2.87 Deformed mesh under HS-20 truck load .....	73
2.88 Deformed Mesh for positive displacement envelope under HS-20 truck load.....	73
2.89 Deformed Mesh for negative displacement envelope under HS-20 truck load.....	73
2.90 Moment Diagram under gravity load .....	74
2.91 Moment Diagram under lane load .....	74
2.92 Moment Diagram under HS-20 truck load .....	74
2.93 Positive Moment Diagram envelope under HS-20 truck moving load .....	75
2.94 Negative Moment Diagram envelope under HS-20 truck moving load .....	75
2.95 Stress Contour $S(x)$ of bridge deck under gravity load .....	75
2.96 Stress Contour $S(x)$ of bridge deck under lane load .....	76
2.97 Stress Contour $S(x)$ of bridge deck under moving HS-20 truck load .....	76
2.98 Stress Contour $S(z)$ of bridge piers under gravity load .....	76
2.99 The 1 <sup>st</sup> mode shape .....	77
2.100The 2 <sup>nd</sup> mode shape .....	78

**LIST OF FIGURES**  
**(Continued)**

<b>Figure</b>	<b>Page</b>
2.101 The 3 <sup>rd</sup> mode shape .....	78
2.102 The 4 <sup>th</sup> mode shape .....	79
2.103 The 5 <sup>th</sup> mode shape .....	79
2.104 The 6 <sup>th</sup> mode shape .....	79
2.105 The 7 <sup>th</sup> mode shape .....	80
2.106 The 8 <sup>th</sup> mode shape .....	80
2.107 The 9 <sup>th</sup> mode shape .....	80
2.108 The 10 <sup>th</sup> mode shape .....	81
3.1 The investigated RC frame .....	84
3.2 Position of steel reinforcement in RC frame .....	84
3.3 Sine excitation of shaking table .....	85
3.4 Wireless sensors arrangement mounted on RC frame .....	86
3.5 RC frame mounted on the shaking table .....	86
3.6 IRIS mote board top and bottom view .....	88
3.7 MIB520 USB interface board .....	89
3.8 Front and back view of the MTS400 sensors' board .....	90
3.9 Acceleration data recorded under 5 Hz excitation .....	91
3.10 Acceleration data recorded under 13 Hz excitation .....	92
3.11 Acceleration data recorded under 20 Hz excitation .....	92
4.1 Advantages and Disadvantages of strain gauges .....	103

**LIST OF FIGURES  
(Continued)**

<b>Figure</b>	<b>Page</b>
4.2 Fiber optic versus vibrating wire Sensors .....	107
4.3 Wireless network topology .....	111
4.4 Schematic Layout of the Accelerometers .....	116
4.5 Distribution of strain gauges in the bridge .....	117
4.6 Locations of Temperature sensors for long-term monitoring .....	118
5.1 Discrete Fourier Transform of a rectangular window .....	129
5.2 SK expectations as function of duty-cycle .....	152
5.3 Data set without background noise .....	154
5.4 Data in the presence of added noise .....	154
5.5 Decimated time series and PSD for 1024 samples without damage .....	155
5.6 Decimated time series and PSD for 1024 samples with damage .....	155
5.7 Damaged detected using both SK analysis and classical spectrum analysis .....	156
5.8 SK-S1 diagram without and with damage based on the bridge dynamic response	157
5.9 SK-S1 diagram based on the bridge dynamic response due to the moving truck ..	158
5.10 SK-S1 diagram based on the bridge dynamic response due to earthquake .....	159
5.11 SK estimators corresponding to the two input force data channels .....	160
5.12 SK estimators corresponding to the first two response data channels .....	161
5.13 Automatic harmonic line identification .....	162
5.14 Illustration of the automated ML FDD algorithm steps .....	169
A.1 Reinforcement assembly .....	178



**LIST OF FIGURES**  
**(Continued)**

<b>Figure</b>	<b>Page</b>
A.2 The wood works and reinforcement for the RC frame .....	178
A.3 Preparation of the concrete .....	179
A.4 Pouring the concrete .....	179
A.5 Curing of the frame .....	179
C.1 Ten second sample of the ground motion accelerograms .....	183

# CHAPTER 1

## INTRODUCTION

### 1.1 Structural Health Monitoring

All structures, including critical civil infrastructure facilities like bridges and highways, deteriorate with time. This deterioration is due to various reasons including fatigue failure caused by repetitive traffic loads, effects of environmental elements, and extreme events such as earthquake, tornados and sever wind. In recent years, the situation of aging infrastructure has become a global concern. This is especially true in the case of highway bridges in the United States, because a large number of structures in the current bridge inventory were built decades ago and are now considered structurally deficient [1]. According to December 2011 data reported by U.S. Department of Transportation-Federal highway administration (FHWA), among total of 605,086 bridges all over the United States more than 23% of the bridges are classified as deficient. Among which 11.15% of them are structurally deficient and 12.62% functionally obsolete. In another report prepared by the American Society of Civil Engineers (ASCE) in 2013[2], there was approximately \$20.5 billion of total investment estimated for full restoration of bridges annually. This number is expected to grow as more than 30 percent of the existing bridges have exceeded their 50-year theoretical design life and are in various levels of repair, rehabilitation, replacement or even decommissioned [3].

In order to maintain the safety of these “lifeline” structures, each state has been mandated by the National Bridge Inspection (NBI) program to periodically inventory and inspect all highway bridges on public roads. Implemented in 1971, The National Bridge Inspection Standards prescribe minimum requirements for the inspection of highway

bridges in the United States [4]. A substantial amount of research has been conducted in this area in order to improve the speed and reliability of such inspections. According to another survey performed by the Federal Highway Administration [5], visual inspection is still the primary tool used to perform these inspections. The implementation of these inspections consists of scheduled field trips to bridge sites at routine intervals, usually once every two years. If a significant increase in distress between inspections is noted, the period between inspections is decreased and the level of inspection is increased till such time that the distress has been corrected by repair or replacement. Research has shown that such inspections have limited accuracy and efficiency [6]. This method of time-based inspection is inefficient in terms of resources, because all bridges are inspected with the same frequency, regardless of the condition of the bridge. Moreover, there is a potential danger that serious damage could happen to the bridge in between two inspections which pose a great hazard to public safety. Visual inspections are highly variable, lack resolution, and fail to detect damage unless it is visible [7]. Furthermore, rapid assessment of structural conditions after major events such as earthquakes is not possible using such approach. As a result, structurally deficient and functionally obsolete bridges may be left undiscovered, potentially putting the public at risk. Therefore, more automated and reliable methods of inspection are necessary.

Over the past decade, the implementation of Structural Health Monitoring (SHM) systems has enhanced as a potential solution to the above challenges. SMH is a mature research field that investigates the current condition of structures by measurement, modal analysis, and condition assessment. It refers to implementation of damage identification strategies to the civil engineering infrastructures [8]. Damage means the degradation of the

performance of the structure which is mainly due to change in material and geometric properties, boundary conditions and system connectivity. SHM strives toward the ideal of not only be able to monitor a structure in such a way that any damage or any growth of fault would be immediately detectable, but also assessing the severity so that decisions can be easily made about what actions need to be taken.

These global objectives for SHM are generally structured into the following levels:

- Damage detection: the method that gives a qualitative indication that damage might be present in the structure.
- Damage Location: The method that gives information about the probable position of the damage.
- Damage Classification: The method that gives information about the type of damage.
- Damage Assessment: The method that gives an estimate of the extent of the damage.
- Damage Prediction: The method that offers information about the safety of the structure, e.g., life span estimate.

Structures are designed to perform well under certain loading and environmental conditions with certain lifespan. However, the actual situation might not always be the same. Performance of structures degrades with time and moreover, there might be some uncertainties involved, such as seismic events, tsunamis or explosions. Structural Health Monitoring helps us to keep track of the performance level of the structures by improving safety and maintaining its functionality. After the occurrence of any catastrophic events such as an earthquake or explosions there is no quantifiable method to check whether the buildings are safe to reoccupy or the bridges are safe to use [8]. The continuous automated

SHM can be a solution for the above mentioned problem. With automated monitoring systems in place on critical life-line structures, the condition of these structures can be monitored and evaluated shortly after an extreme event has occurred. This rapid evaluation would not be possible using traditional inspection techniques. Necessary decisions to best utilize the remaining intact life-lines can be made based on these evaluations. This could potentially give the authority faster access to the affected areas and thus improving public safety. As the principles of SHM and its applications is not only in the inspection of existing infrastructure but also lifetime monitoring of future construction projects [9]. There has been an increase interest in SHM by infrastructure stakeholders due to its high potential for the economic benefits and life safety of the users. Numerous SHM methods have been proposed in recent years; detailed reviews are provided by [10, 11].

### **1.2 Vibration Based Damage Detection Strategy**

The various disciplines utilize different approaches in SHM. The first successful attempts have been taken by the mechanical engineers using analysis of vibrations for the prediction of damage of machinery during the late 1970s. Few years later, the automobile and aerospace industry discovered the advantages of diagnosis systems. In these disciplines, SHM profits from the very well-defined material properties and geometries. Also, the objectives are very similar from case to case and stable routines was developed. The practice has focused on the detection of crack and fatigue indicators in aircraft bodies and machinery.

Bridges are structures that have very little in common with each other. Almost any new bridge is a prototype. The combination of facts, use, properties, boundary conditions and geometry create a huge number of unknowns. As a result, a uniform monitoring

process is not feasible. There is an extensive difference between civil engineering and all the other disciplines. In mechanical engineering, automotive or aeronautics monitoring systems are designed to work permanently over the lifetime of a structure or component. In civil engineering, this is not feasible financially. Most of civil structures already exist with a widely unknown history. Therefore, considerable educational effort is necessary to support the requirements of realistic damage detection and assessment.

During the last three decades, a great deal of research has been conducted in the field of Vibration-Based Structural Health Monitoring. A broad range of techniques, algorithms and methods were developed to solve damage identification problems in structures, from basic structural components such as beams and plates to complex structural systems like bridges and high-rise buildings.

Most non-destructive damage identification methods can be categorized as either local or global damage identification techniques [10]. Local damage identification techniques, such as ultrasonic methods and X-ray methods, require a priori information of damage locations. Locating procedure using these methods is often time consuming and expensive and cannot be guaranteed for most cases in civil engineering. Furthermore, Nondestructive Evaluation requires detailed scanning of each structure member; which is not feasible for large scale structures. Hence, the dynamic-based damage identification method, as a global damage identification technique was developed to overcome these difficulties. The dynamic-based damage identification is based on the idea that damage causes changes in structural parameters such as mass, damping, stiffness and flexibility. This will lead to changes in the dynamic structure's properties and vibration modal parameters such as natural frequency, modal damping and mode shapes. Therefore,

damage can be identified by analyzing the changes in dynamic features of the structure. This makes the vibration-based method suitable for SHM system for large civil infrastructures.

### **1.3 Operational Modal Analysis**

From the discussion in the previous Section, it becomes clear that the measurement of structural dynamic properties such as modal parameters is an important step in vibration-based structural health monitoring. The use of experimental tests to gain knowledge about the dynamic response of civil structures is a well-established practice. The experimental identification of the modal parameters can be dated back to the middle of the Twentieth Century [12]. As mentioned before, that the dynamic behavior of the structure can be demonstrate as a combination of modes that each one characterized by a set of parameters such as natural frequency, damping ratio and mode shapes whose values depend on the structure's geometry, material properties and boundary conditions. Traditional Experimental Modal Analysis (EMA) identifies those parameters from measurements of the applied force and the vibration response. EMA makes use of measured input excitation as well as output response and has made substantial progress in the past three decades. Numerous modal identification algorithms have been developed and applied in various fields such as vibration control, structural dynamic modification, and analytical model validation, as well as vibration-based structural health monitoring in mechanical, aerospace and civil applications. However, Traditional Experimental Modal Analysis suffers some Limitations such as:

- Need of an artificial excitation in order to measure Frequency Response Functions (FRF) or Impulse Response Functions (IRF);

- Operational conditions often different from those ones applied in the lab environment tests;
- Simulated boundary conditions, since tests are carried out on components instead of complete systems.

The identification of the modal parameters by EMA techniques becomes more challenging in the case of civil engineering structures because of their large size and low frequency range. It is typically very difficult to excite the structure using controlled input and requires expensive and heavy devices which increases the risk of damaging the structures. As a consequence, since early 1990's Operational Modal Analysis (OMA) has drawn significant attention in the field of civil engineering with applications on several structures (buildings, bridges, off-shore platforms, etc.).

OMA utilizes only response measurements of the structure under operational or ambient conditions to identify modal parameters. The idea behind OMA is to take advantage of the natural and freely available excitation due to ambient forces and operational loads (wind, traffic, micro-tremors, etc.) which makes it particularly attractive for vibration-based bridge health monitoring applications because the bridge does not need to be closed to traffic to perform the modal parameter identification. In other words, the identified modal parameters are representative of the actual behavior of the structure in its operational conditions, since they refer to levels of vibration actually present in the structure and not to artificially generated vibrations. Due to these reasons, it has become the method of choice for identification of structural modal parameters in long-term Vibration-based Structural Health Monitoring applications. OMA is also known under



different names, such as ambient vibration modal identification or output-only modal analysis.

Over the years, Operational Modal Analysis advanced as an independent discipline, but most of the OMA methods have been derived from EMA procedures, so they share a common theoretical background. The main difference is the formulation of input which is known in EMA while it is random and not measured in OMA. EMA procedures are developed in a deterministic framework while OMA methods are based on random response and stochastic approach. In Operational Modal Analysis input is assumed to be a Gaussian white noise and characterized by a flat spectrum in frequency domain. In this way, all nodes are assumed to be equally excited in the frequency range of interest and extracted by appropriate procedure. Both EMA and OMA techniques can be categorized in frequency domain or time domain methods.

Despite of the differences in terms of excitation, modal analysis is always based on the following steps:

- planning and execution of tests: this step concerns the definition of the experimental setup such as: proper location of sensors and the data acquisition parameters.
- data processing and identification of modal parameters (filtering, decimation, windowing; extraction of modal parameters); this step concerns the validation and pre-treatment of the acquired data, and the estimation of the modal parameters.
- validation of the modal parameter estimates.

The final objective of the test is not the estimation of modal parameters. In fact, these parameters can be used as input or reference for a number of applications. Model updating is probably the most common [13]. Since the modal parameters estimates provided by Finite Element models are not often reliable, the numerical model is not the

representative of the actual dynamic behavior of the structure. As a result, the experimental modal properties are used to enhance a FE model of the structure in order to make it more adherent to the structure's actual behavior.

Additionally, the identified modal parameters are sometimes used for troubleshooting by using the identified vibrational properties to find out the cause of problems often encountered in real life such as excessive noise or vibrations. Also the estimated modal parameters can be used for sensitivity analyses to evaluate the effect of changes on the dynamics without actually modifying the structure [12]. Furthermore, some applications concern force identification. In this case, the known modal parameters are used to solve an inverse problem for the identification of the unknown forces that produced a given measured response [14].

Another relevant application of the identified modal parameters is damage detection and structural health monitoring. Indications of presence of damage on the structure can be obtained after comparing current modal parameters of the structure with the modal parameters at a reference state. With the developments of methods in the last few years not only the damage can be detected, but also it can be located and quantified. Extensive reviews about these techniques are available in these literatures [10, 11, 15].

The main drawback of damage detection techniques based on the analysis of the changes in the estimated modal properties is that significant changes in modal frequencies cannot imply presence of damage due to the influence of boundary conditions and operational and environmental factors on the estimates. However, in recent years a number of techniques have been developed by monitoring environmental conditions together with the structural response, which enables them to remove the influence of environmental

factors on modal parameter estimates [16, 17]. As a result, raising interest towards vibration-based damage detection has been renewed. Another relevant limitation to the extensive application of these damage detection techniques was the lack of fully automated procedures for the estimation of the modal parameters of the monitored structure. This issue has determined large research efforts in the last few years to develop reliable and robust automated OMA techniques [13].

#### **1.4 Research Objectives**

The previous section presents the state-of-the-art in the technical background of the Structural Health Monitoring. The research proposes a development of a long term monitoring system for damage detection and real-time monitoring. In this research three main aspects are considered. The first one is the development of an improved method for damage localization, identification, and detection in SHM. The second one is the optimal design of Wireless Sensor Networks for SHM monitoring. Finally, the third one is the improvement of the reliability of the monitoring and predict the capacity and remaining life of the structure.

This research provides deeper insight into the utilization of WSNs for SHM including the sensing techniques, optimization of WSNs design particularly for SHM monitoring and damage detection techniques. The proposed system will not only aim to detect damage after it happens but it will also aim to predict damage before it takes place. The data obtained from the research will result in a reduction in the lifecycle costs and risks related to bridge structures.

The proposed technique will eventually be applied to the new stadium that State of Qatar will build in preparation for the 2022 World Cup. This monitoring system will help permanently record the vibration levels reached in all substructures during each event to evaluate the actual health state of the stadiums. This offers the opportunity to detect potentially dangerous situations before they become critical.

### **1.5 Thesis Overview**

This thesis consists of six chapters. The layout of the thesis document is presented as follows:

Chapter 1, the current chapter, presents the introduction of the work referring the motivation, the general background of Structural Health Monitoring topics as well as the objectives of this research.

Chapter 2 presents Finite Element Analysis (FEA) of a scaled down Reinforced Concrete Frame, 3-Span Bridge and an In-service 6-Span Precast Segmental Box Girder Bridge. The mode shapes of all structures are obtained from eigenvalue frequency analysis. For the 3-Span Bridge, Moving Load analysis has been carried out and Seismic Response of the bridge under El Centro earthquake ground motion is presented. The later sections of the chapter provides Static and Dynamic Finite Element analysis of 6-Span Concrete Box Girder Bridge. Analysis results for each model thoroughly demonstrated in each section.

Chapter 3 is dedicated to a preliminary study in designing and setting up a test-bed for the research on Structural Health Monitoring utilizing Wireless Sensor Networks. The design and setup of the physical model are presented in detail. Three different excitation cases has been investigated to evaluate the performance of the developed wireless sensing system under actual experimental conditions.

Chapter 4 outlines the design criteria of SHM for a large-scale bridge. The available technologies on measurement sensors and data acquisition equipment for performing long term monitoring is then introduced. Special emphasis is given to the wireless based systems presenting their state of the art and their current and past applications for monitoring civil engineering structures. In this chapter, a long-term Structural Health Monitoring System using Wireless Sensor Networks (WSNs) for an in-service highway bridge is also devised.

Chapter 5 presents the theoretical basis of the Operational Modal Analysis. Here, it is shown that higher order statistical estimators such as Spectral Kurtosis (SK) and Sample to Model Ratio (SMR) can be successfully employed to more reliably discriminate the response of the system against the ambient noise fluctuations and to better identify and separate contributions from closely spaced individual modes. Moreover, it is shown that a SMR-based Maximum Likelihood curve fitting algorithm improves the accuracy of the spectral shape and location of the individual modes.

Chapter 6 presents the conclusions of the thesis as well as the proposal of future developments.

## **CHAPTER 2**

### **FINITE ELEMENT ANALYSIS**

#### **2.1 Introduction**

The Lusas Bridge Plus finite element program, operating on Windows 8, was used in this study to simulate the behavior of an experimental frame, 3-Span Bridge and an in-service 6-Span Precast Segmental Box Girder Bridge. In general, the conclusions and methods would be very similar using other nonlinear Finite Element Analysis programs. Each program, however, has its own nomenclature and specialized elements and analysis procedures that need to be used properly. Which requires the analyst to be thoroughly familiar with the finite element tools being used, and progress from simpler to more complex problems in order to gain confidence in the use of new techniques.

This chapter discusses model development for aforementioned structures. Element types used in the models are covered along with the constitutive assumptions and parameters for the various materials in each Section. Besides, Geometry of the models, loading and boundary conditions are presented. The reader can refer to a wide variety of finite element analysis textbooks for a more formal and complete introduction to basic concepts if needed.

#### **2.2 Lusas Bridge Software**

LUSAS Bridge is a world-leading finite element analysis software for the analysis, design and assessment of all types of bridge structures. LUSAS Bridge provides all the facilities needed to carry out from a straightforward linear static analysis of a single span road bridge, to a dynamic analysis of a slender ‘architectural’ steel movable footbridge, or a detailed

geometrically nonlinear staged erection analysis of a major cable stayed structure involving concrete creep and shrinkage. LUSAS Bridge is available in a choice of software levels; Bridge LT, Bridge, and Bridge Plus to suit different analysis needs. Bridge Plus version has been selected to use in this research which has outstanding range of analysis facilities for linear static, fundamental frequency, seismic, dynamic, soil-structure interaction, large deflection, staged construction, creep, pre-stress, post tensioning and fatigue analysis. Moreover, Plus versions allow for more advanced analyses to be undertaken and include an extended high-performance element library. A list of software options available in Lusas Bridge plus version is given in Table 2.1. In order to facilitate the discussion in the later parts of this chapter, it is necessary to provide a brief review of some of the features of Lusas Bridge Plus that have been utilized in this research.

**Table 2.1** Options Available in Lusas Bridge Plus Software

<b>LUSAS Bridge Plus Software Option</b>
Fast Solvers
Vehicle Load Optimization
Steel and Composite Deck Designer
IMDplus Analysis
Nonlinear Analysis
Dynamic Analysis
Thermal / Field Analysis
Heat of Hydration Analysis
Rail Track Analysis

Two types of fast solvers implemented in this software which are Multifrontal Direct Solver and Multifrontal Block Lanczos EigenSolver. The Fast Multifrontal Direct Solver is an implementation of the multifrontal method of Gaussian Elimination, and uses

the modern sparse matrix technology of assembling a global stiffness matrix where only the non-zero entries are stored. The solver can be used for almost all types of analysis, and has extensive pivoting options to ensure numerical stability, especially for symmetric problems. As a result, it is particularly fast at solving large 3D solid models and the disk space requirements are typically 75% less than that of the standard frontal direct solvers. Additionally, a data check facility with the standard Frontal Direct solver which enables rerunning linear analyses with different load cases without having to eliminate the stiffness matrix. The Fast Multifrontal Block Lanczos Eigensolver is based on the Shift and Inverse Block Lanczos algorithm and solves natural frequency, vibration and buckling problems with real, symmetric matrices. It is fast, robust, and ensures that convergence is almost always achieved. For instance, the lowest, highest or a range of eigenvalues can be specified to be returned, along with the normalized eigenvectors and error norms which are currently given with the standard Frontal Eigensolvers. In other words, you can specify combinations of eigenvalues to be returned in the same analysis, as for example, the highest three eigenvalues can be specified, followed by the lowest ten, and all those in the range 0 to 50. The complex eigensolver is non-symmetric eigensolver based on an implicitly restarted Arnoldi method. It provides solutions to damped natural frequency problems for both solid and fluid mechanics. It can solve large scale problems with real, non-symmetric input matrices (in particular, those involving non-proportional damping), and gives solutions that consist of complex numbers where appropriate.

Vehicle Load Optimization software complements and extends the in-built static and moving vehicle loading capabilities of LUSAS Bridge and helps to significantly simplify the evaluation of worst load position for various load configurations. It is used to



identify critical vehicle loading patterns on bridges and apply these loading patterns to LUSAS analysis models. It reduces the amount of time spent generating models and leads to more efficient and economic design, assessment or load rating of bridge structures.

Vehicle Load Optimization works with numerous country design codes such as:

- United States of America: AASHTO LFD, LRFD
- United Kingdom: EN1991-2, BD21/97, BD21/01, BD37/88, BD37/01 (Road+Rail), BS5400 Rail Railtrack document RT/CE/025
- Europe: EN1991-2
- Canada CAN/CSA-S6-06

The IMDPlus option extends the Interactive Modal Dynamics (IMD) techniques available in LUSAS software. While, IMD models a single loading event in a single direction, IMDPlus allows multiple loading events with more advanced loading conditions to be solved. IMDPlus is applicable to both 2D and 3D structures and has three primary uses:

- Moving load analysis of structures, such as bridges subjected to moving vehicle or train loads, where the magnitude and configuration of the loading remains constant throughout the analysis.
- Moving mass and moving sprung mass analysis of structures, such as bridges subjected to moving vehicle or train loads, where mass-spring-damper systems are used to represent the vehicle. The configuration of the systems remains constant throughout the analysis but, as they move across the structure, the dynamic response of the unsprung and sprung masses affects the applied loading due to inertia effects.
- Seismic Response analysis of structures subjected to acceleration time histories of support motion.

An IMDPlus analysis uses conventional eigenvalue analyses to obtain the undamped modes of vibration for a structure over the frequency range of interest. The modal response in the form of frequencies, participation factors and eigenvectors, together with the seismic accelerations or moving load/moving mass vehicle loads, enable IMDPlus to compute the dynamic response for each mode of vibration. The assumption of linear structural behavior allows the IMDPlus facility to utilize linear superposition methods to calculate the total response of the structure from each of the contributing frequencies.

The LUSAS Dynamics Option contains the facilities required to solve a wider range of dynamic problems in both the time and frequency domains. By combining the LUSAS Dynamic and LUSAS Nonlinear options, both high and low velocity nonlinear impact problems can be solved using either implicit or explicit solution techniques. By combining the LUSAS Dynamic and LUSAS Thermal options, time-domain analyses such as Transient Field can be carried out.

LUSAS Bridge is used by structural engineers worldwide for all types of bridge analysis, design and load rating. There are numerous Case studies in the literature which provide a number of uses of Lusas Bridge software[18].

### 2.3 Analysis of a Reinforced Concrete Frame

The Reinforced Concrete Frame modeled in this section had span of 32.5 cm (12.8 in) and height of 24.5 cm (9.6 in) as shown in Figure 2.1. The frame properties are: The modulus of elasticity  $E_c = 31.58\text{MPa}$  (4500 psi), mass per unit volume  $M = 2400\text{ kg/m}^3$  (150 lb/scf), cross-section dimensions  $5 \times 5\text{ cm}$  for an area  $A = 25\text{ cm}^2$ , #2 (6 mm diameter) for Steel rebar, for stirrups diameter of 3 mm and 1 cm concrete cover. Figure 2.2 shows the frame dimensions and the location of the rebar. Table 2.2 shows the material properties used for analysis.



**Figure 2.1** The investigated RC Frame.

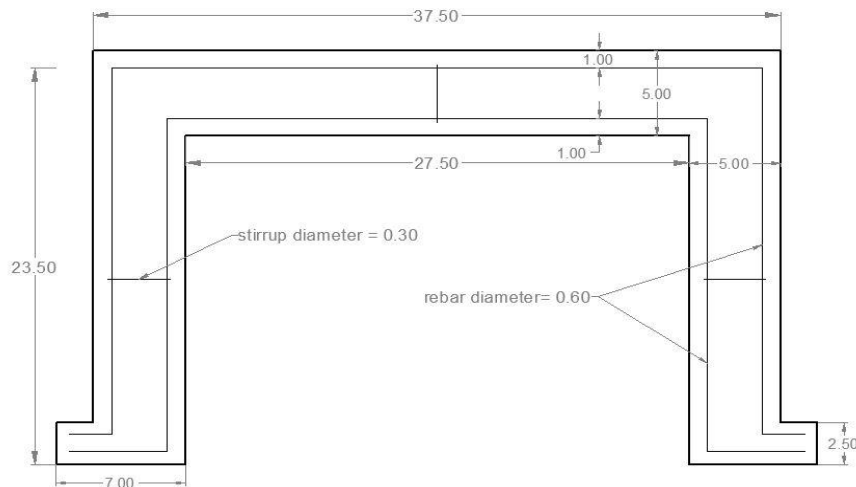


**Figure 2.2** Position of steel reinforcement in RC Frame (Dimensions are in cm).

**Table 2.2** Design Material Properties.

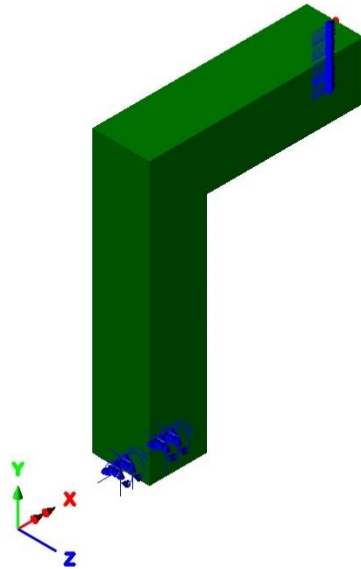
<b>Material</b>	<b>Limiting Stress</b>	<b>Limiting Strain</b>	<b>Limit State</b>	<b>Elastic Modulus</b>
Concret (Compression)	4500 psi (31.58 MPa )	0.003	Crushing	6000 <i>ksi</i> <sup>1</sup> (42 GPa)
Steel Reinforcement	60 ksi (414 MPa)	0.002	Yielding	29,000(200 GPa)

<sup>1</sup> Design elastic modulus from  $E_c = 57,000(f_c')^{1/2}$ .

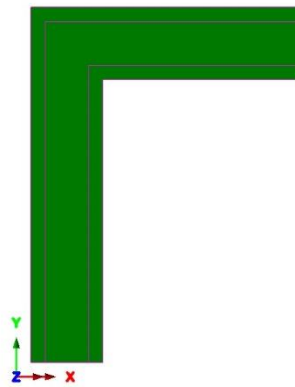
### 2.3.1 Modeling Description

A Natural Frequency Analysis is to be carried out on a model of a Reinforced Concrete Frame. As mentioned before, the reinforcement is provided in the beam and columns has a total cross-sectional area of  $1.13 \text{ cm}^2$  ( $0.444 \text{ in}^2$ ). The superposition of nodal degrees of freedom assumes that the concrete and reinforcement are perfectly bonded. It is assumed that the effects of any shear reinforcement can be ignored.

Due to the symmetrical nature of the problem, only the left-hand span of the frame is modelled (see Figure 2.3). The column support is fixed at the left-hand of the frame with a symmetry support at the right-hand axis of symmetry as shown in Figure 2.4.



**Figure 2.3** RC Frame geometry defined in Lusas.

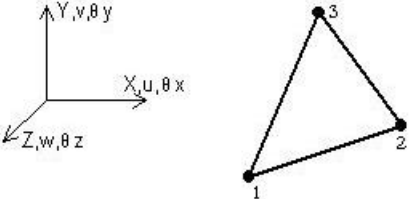


**Figure 2.4** RC Frame supports.

No static structural loading is required for this analysis because only the dynamic loading is considered during the results processing based on the results from the natural frequency analysis. The concrete section is represented by Thick Shell (TTS3) elements, and the reinforcement bars are represented by nonlinear Beam (BTS3) elements and then as presented in Figure 2.5 the actual geometric properties of the reinforcement has been applied to the element, See Tables 2.3 and 2.4 for more element details. A nonlinear

concrete cracking material model is applied to the thick shell elements and a von Mises plastic material is applied to the reinforcement bars. Units of N, mm, t, s, C are used throughout the finite element modeling of this frame.

**Table 2.3** 3D Flat Thin Shell Elements TTS3 Description

<p><b>General</b></p>	
<p><b>Element Group</b></p>	<p>Thick Shells</p>
<p><b>Element Description</b></p>	<p>A family of shell elements for the analysis of arbitrarily thick and thin curved shell geometries, including multiple branched junctions. The quadratic elements can accommodate generally curved geometry while all elements account for varying thickness. Anisotropic and composite material properties can be defined. These degenerate continuum elements are also capable of modelling warped configurations. The element formulation takes account of membrane, shear and flexural deformations. This elements use an assumed strain field to define transverse shear which ensures that the element does not lock when it is thin.</p>
<p><b>Number Of Nodes</b></p>	<p>3, numbered anticlockwise.</p>
<p><b>Freedoms</b></p>	<p>Default: 5 degrees of freedom are associated with each node U, V, W, <math>\theta\alpha</math>, <math>\theta\beta</math>. To avoid singularities, the rotations <math>\theta\alpha</math> and <math>\theta\beta</math> relate to axes defined by the orientation of the normal at a node. Degrees of freedom relating to global axes: U, V, W, <math>\theta x</math>, <math>\theta y</math>, <math>\theta z</math> may be enforced using the Nodal Freedom data input, or for all shell nodes by using option 278.</p>
<p><b>Notes</b></p>	<p>For TTS3 elements all moments and shears are constant for the element.</p>

**Table 2.4** 3D Thick Beam Element BTS3 Description

<b>General</b>	
<b>Element Group</b>	Thick Beams
<b>Element Description</b>	A straight beam element in 3D for which shear deformations are included. The geometric properties are constant along the length.
<b>Number Of Nodes</b>	3 with end release conditions. The third node is used to define the local xy-plane.
<b>Freedoms</b>	U, V, W, $\theta_x$ , $\theta_y$ , $\theta_z$ : at end nodes.

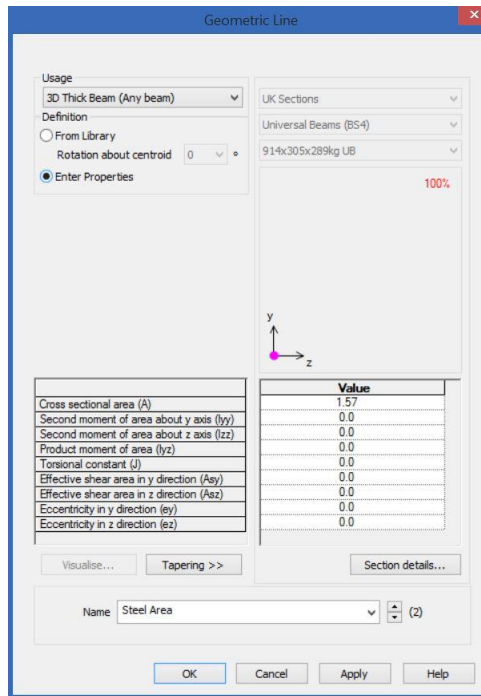


**Figure 2.5** Geometric properties of the reinforcement for beam element.

As a crucial step, a finite element analysis requires meshing of the model. In other words, the model is divided into a number of small elements, and after loading, stress and

strain are calculated at integration points of these small elements [19]. In this FE model, Separate mesh datasets need to be defined for the reinforcement bars and the concrete. The reinforcement bars are modelled using Line meshes. As shown in Figure 2.6 a graded mesh is used for the reinforcement bars. The concrete is modelled using a Surface mesh with Line mesh divisions to control the mesh density (see Figure 2.7)

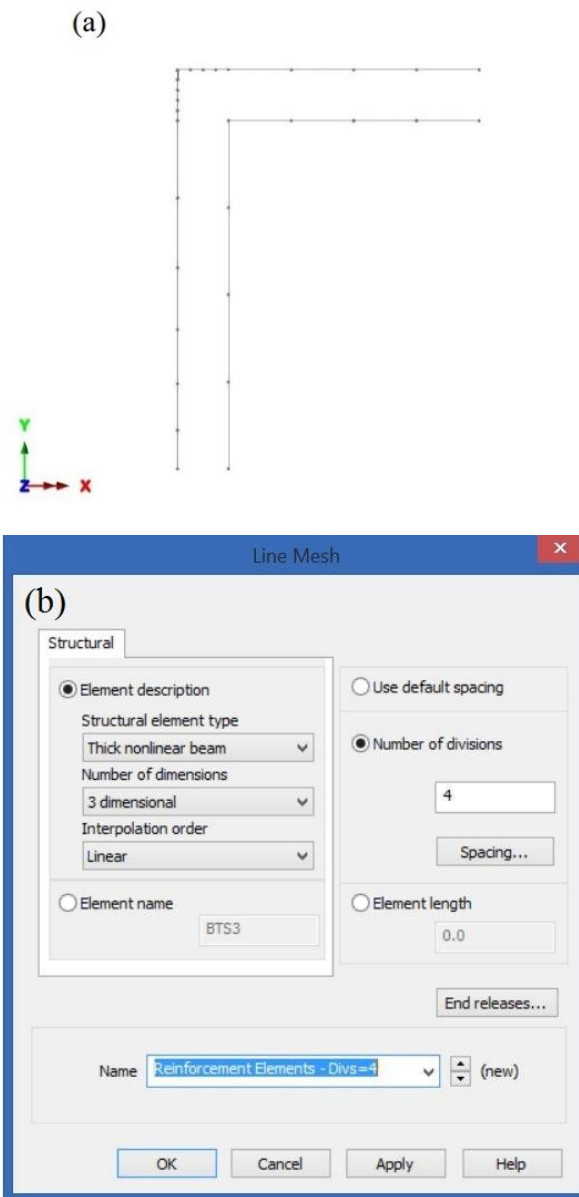


**Figure 2.6** Mesh Reinforcement Bars (a), Mesh Properties (b).



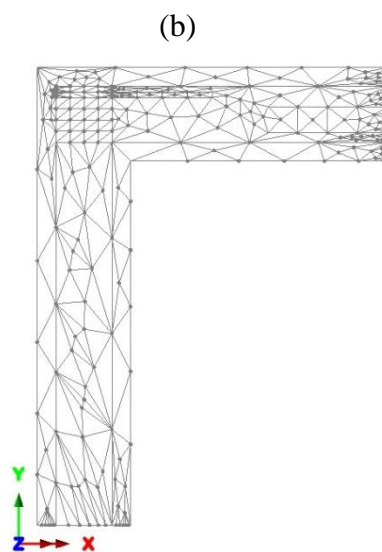
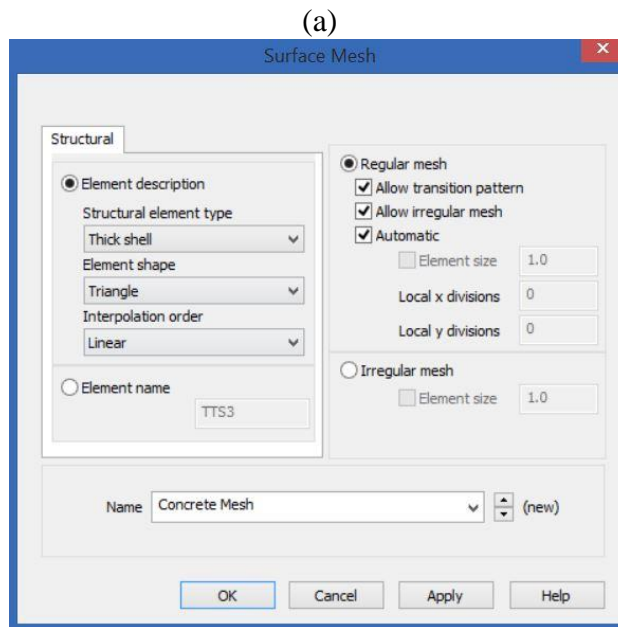


**Figure 2.7** Mesh Concrete (a), Mesh Properties (b).

Nonlinear steel properties has been defined for the reinforcing Bar elements and nonlinear concrete material properties for the Surface elements representing the concrete as illustrated in Figures 2.8 and 2.9 respectively.

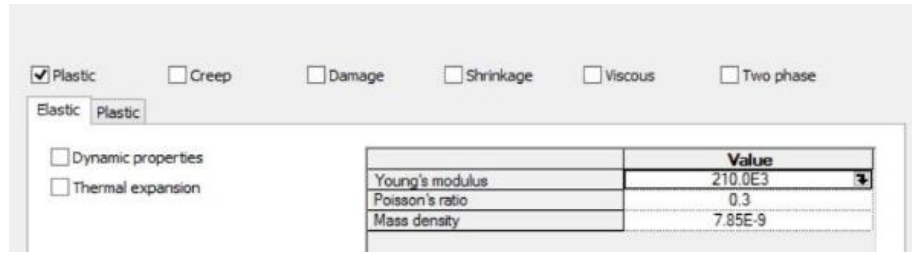
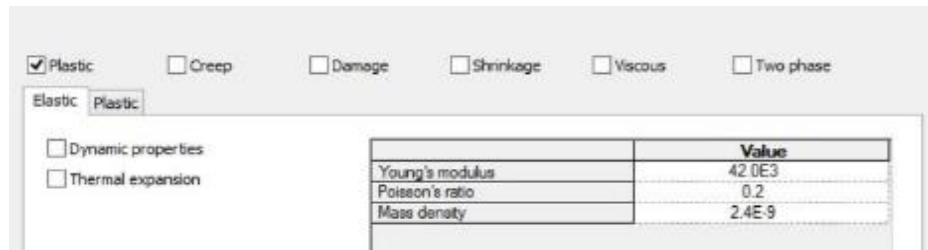


**Figure 2.8** Steel material properties.

(a)



(b)

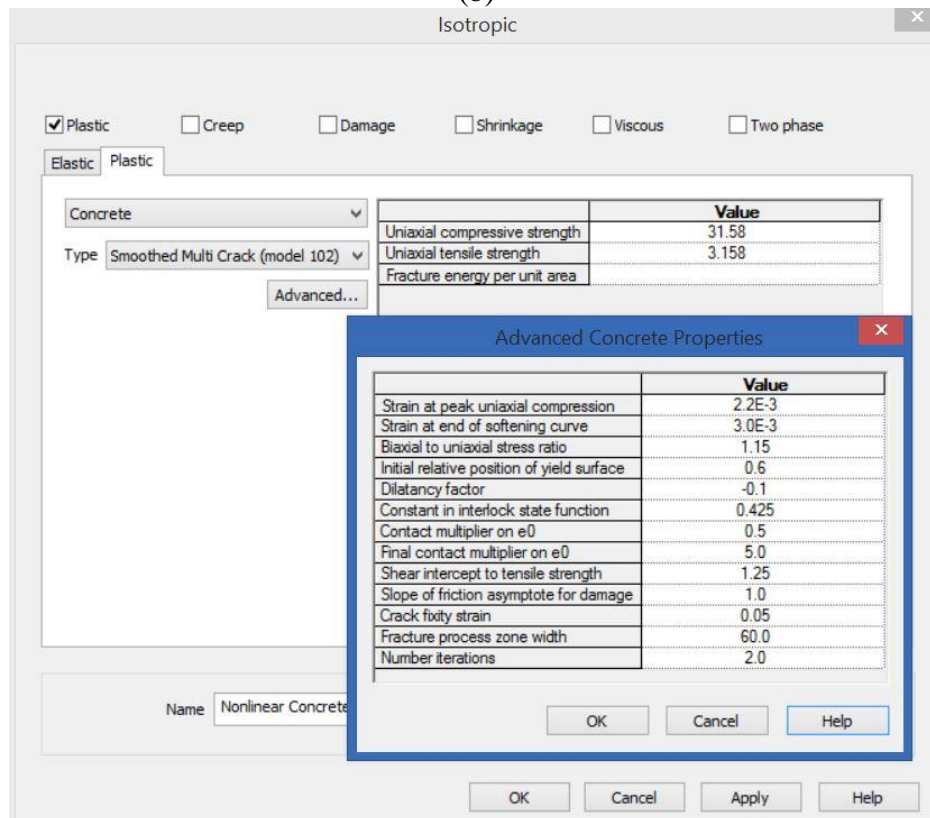


**Figure 2.9** Concrete elastic (a) and plastic (b) properties.

The modelling is completed by defining the controls necessary to extract the natural frequencies. Eigenvalue controls are defined as properties of the loadcase utilizing the IMDPlus option in Lusas (see Figure 2.10). The working assumptions for the IMDPlus modal dynamics facility are as follows:

- The system is linear in terms of geometry, material properties and boundary conditions. Therefore, geometrically nonlinear eigenvalue results are not applicable. Nor are nonlinear joint and slideline analyses suitable for this type of post-processing treatment.
- There is no cross-coupling of modes caused by the damping matrix. This is reasonable for all but the most highly damped structures or applications.

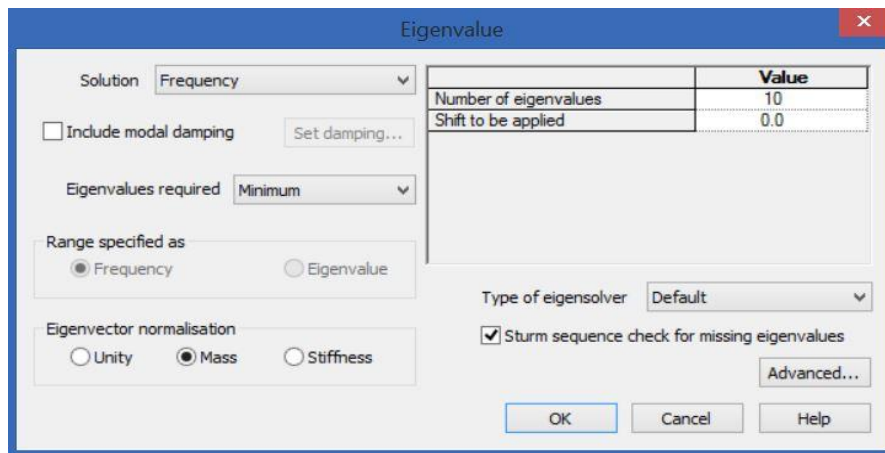


**Figure 2.10** Eigenvalue Controls.

### 2.3.2 Natural Frequency Analysis Results

The mode shapes obtained from eigenvalue frequency analysis are plotted in Figures 2.11-2.20. The first two vibrational modes are transverse modes and the third mode is the first vertical mode. Moreover, the first mode of the frame was found to have frequency of 298.78 Hz (Figure 2.11), the second mode was found to be at 756.96 Hz (Figure 2.12). Eigenvalue results of the first 10 mode shapes for the whole structure are displayed in Table

2.5. Noting that the frequency in Hertz is obtained by dividing the square root of the eigenvalue by  $2\pi$ , and the period of vibration in seconds can be obtained using the reciprocal of frequency ( $1/\text{frequency}$ ). The error norm for a given mode provides a relative measure of the accuracy of the computed modes. A high error norm signifies inaccuracy in either the eigenvalue or the eigenvector, or both and will provoke a warning message in Lusas Bridge software.

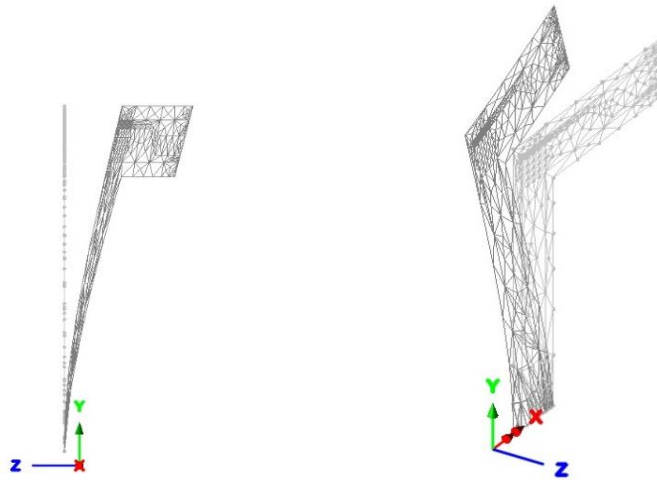


**Figure 2.11** The 1<sup>st</sup> mode shape (frequency: 298.78 Hz).

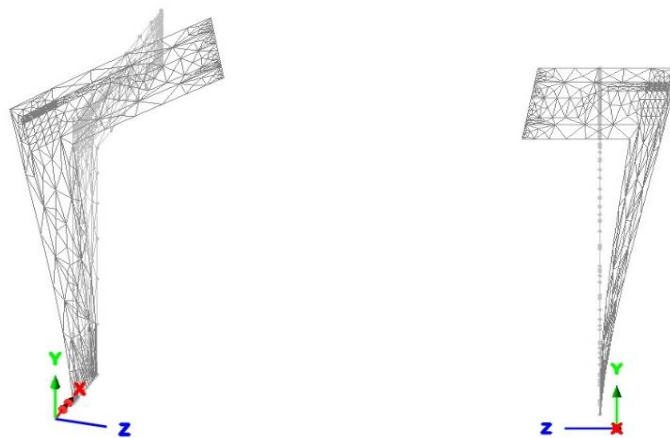


**Figure 2.12** The 2<sup>nd</sup> mode shape (frequency: 756.96 Hz).

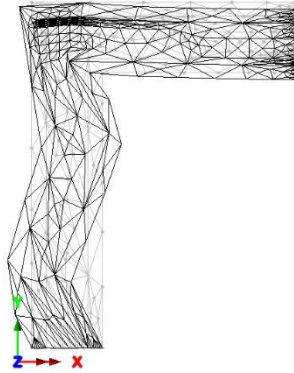


**Figure 2.13** The 3<sup>rd</sup> mode shape (frequency: 1206.3 Hz).

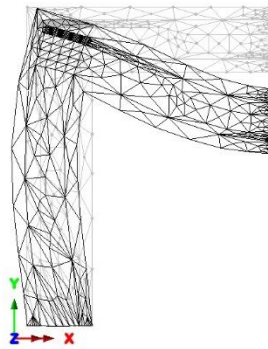


**Figure 2.14** The 4<sup>th</sup> mode shape.

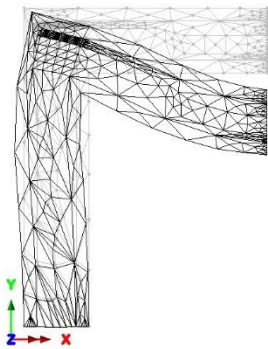


**Figure 2.15** The 5<sup>th</sup> mode shape.

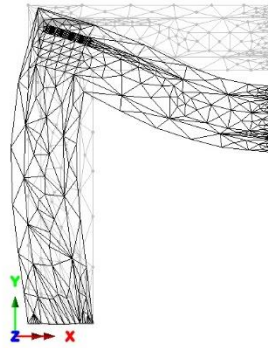


**Figure 2.16** The 6<sup>th</sup> mode shape.

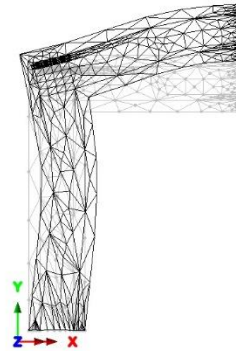


**Figure 2.17** The 7<sup>th</sup> mode shape.

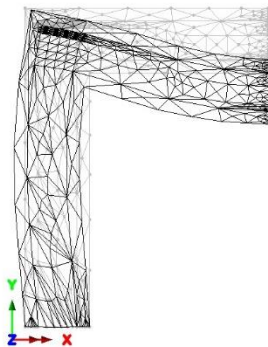


**Figure 2.18** The 8<sup>th</sup> mode shape.

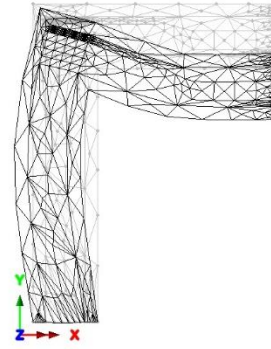


**Figure 2.19** The 9<sup>th</sup> mode shape.

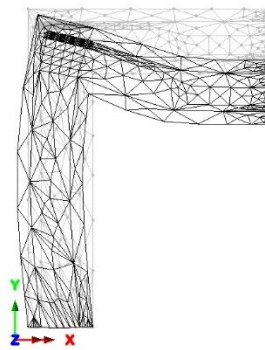


**Figure 2.20** The 10<sup>th</sup> mode shape.

**Table 2.5** Modal Frequencies of RC frame

Mode	Eigenvalue	Frequency (Hz)	Error Norm
<b>1</b>	0.352416E+07	298.778	0.998320E-10
<b>2</b>	0.226209E+08	756.964	0.209138E-10
<b>3</b>	0.574492E+08	1206.32	0.840491E-11
<b>4</b>	0.103503E+09	1619.18	0.134112E-10
<b>5</b>	0.113124E+09	1692.77	0.103542E-10
<b>6</b>	0.136238E+09	1857.67	0.140018E-10
<b>7</b>	0.138146E+09	1870.63	0.915716E-11
<b>8</b>	0.138281E+09	1871.55	0.157550E-09
<b>9</b>	0.251601E+09	2524.50	0.476150E-06
<b>10</b>	0.254828E+09	2540.64	0.139250E-06

## 2.4 Analysis of 3-Span Concrete Box Beam Bridge of Varying Section

A 3-Span Concrete Box Beam Bridge of varying cross-section is modelled using the box section property calculator and the multiple varying sections facilities in LUSAS (Figure 2.21).

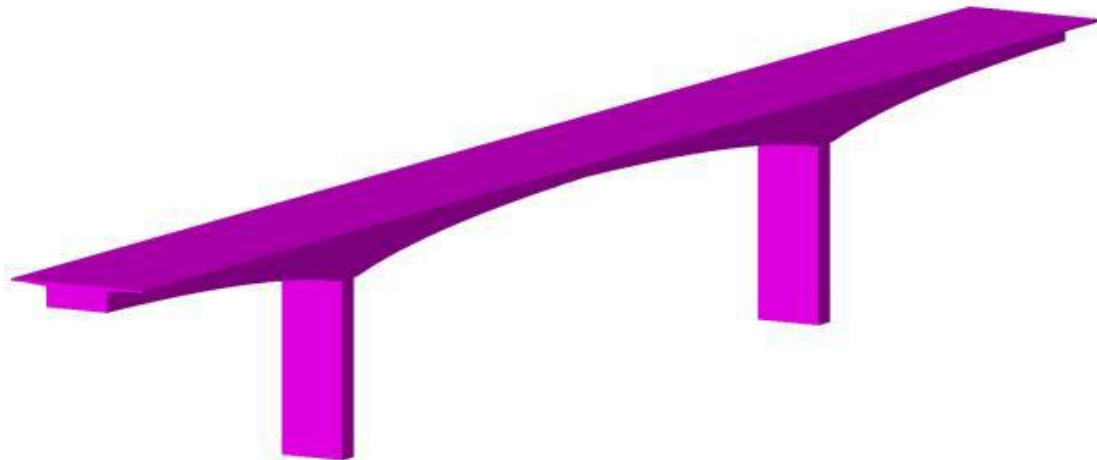


**Figure 2.21** 3-Span Concrete Box Beam bridge.

Two models are created suitable for prototype / assessment work; a preliminary model and a damaged model. Simplified geometry is used for both to allow the example to concentrate on the use of IMDPlus (Interactive Modal Dynamics) facility to extract the bridge response under the moving truck load. Units used are kN, m, kg, s, C throughout.

### 2.4.1 Bridge Description

The 3-span structure is comprised of varying hollow cross-sections with solid diaphragm sections at the four supports. Cross-section properties for three void locations on the structure (as shown in Figure 2.22) is defined and used in the creation of multiple varying section geometric line attributes and then assigned to selected lines on the model.



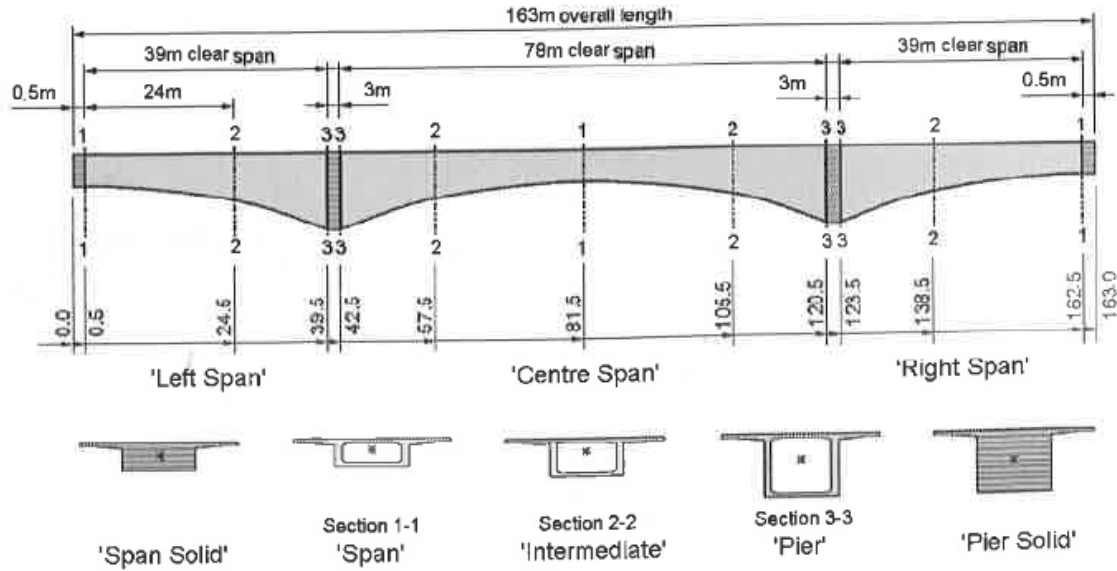


**Figure 2.22** Elevation and cross sections of the bridge.

The supplied basic beam model is a 'Flat' model with clear spans of 39m, 78m and 39m formed of single straight lines. During the initial part of FE modeling of multiple varying section, geometric line attributes are assigned to the single lines along with other section properties and a simple linear analysis is carried out in order to verify the model.

### 2.4.2 Modeling Description

The geometric lines of this model have been assigned a line mesh of Thick Beam elements with an element length of 1m. Concrete (ungraded) material properties (see Figure 2.23), and a structural gravity load have also been assigned. Fixed supports restrain the piers and roller supports restrain the ends of the deck as illustrated in Figure 2.24.

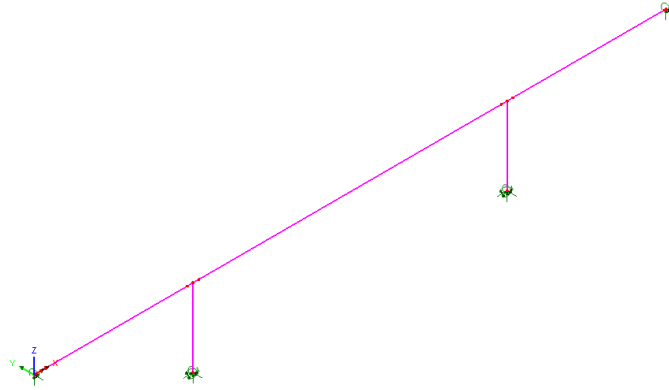


**Figure 2.23** Geometric lines and supports of the varying section bridge.

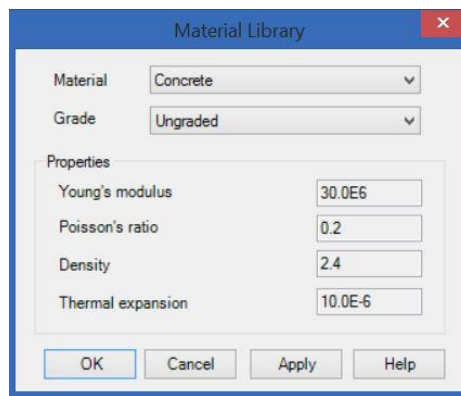


**Figure 2.24** Concrete material properties.

Cross-section properties for three voided box sections that are used in three spans are defined which shown in Figures 2.25-2.27 utilizing the Complex Section option. Solid sections has been modeled by excluding voids (see Figures 2.28 and 2.29) and a rectangular solid section has been used for piers as shown in Figure 2.30.

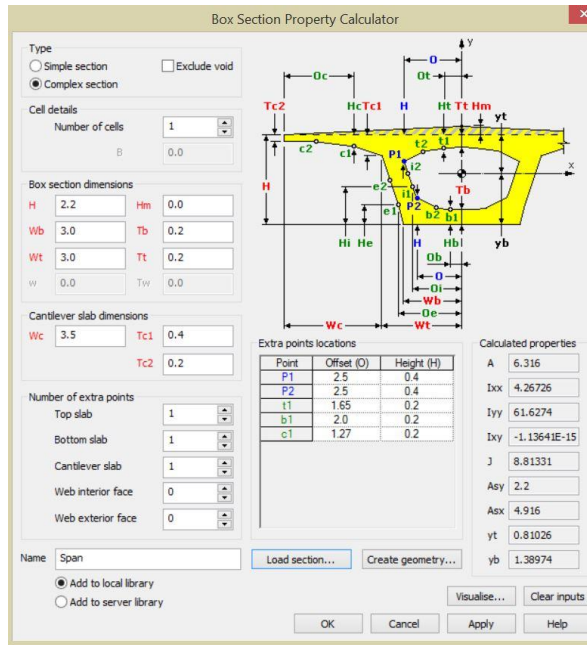


Figure 2.25 Voided span section properties.

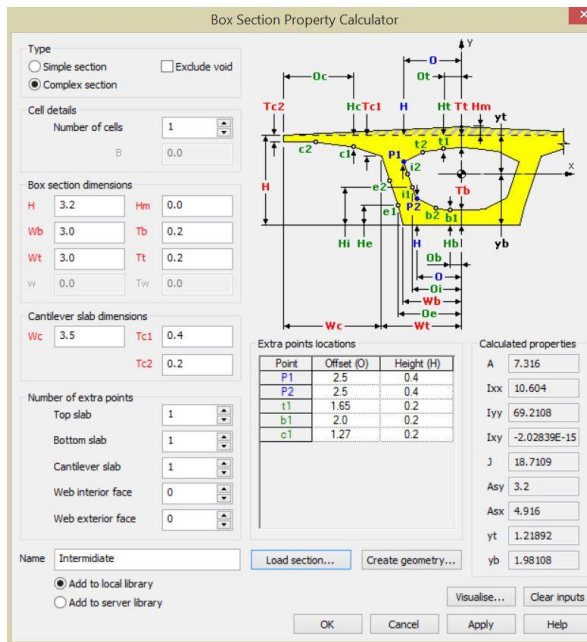


Figure 2.26 Voided intermediate section properties.

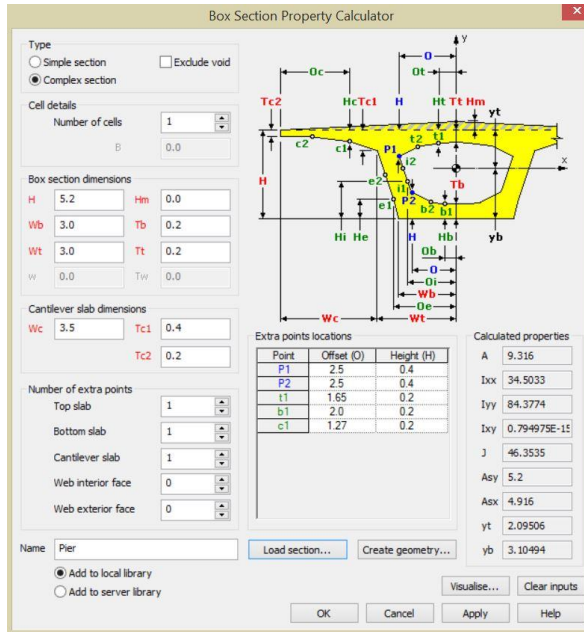


Figure 2.27 Properties of the voided section adjacent to the pier.

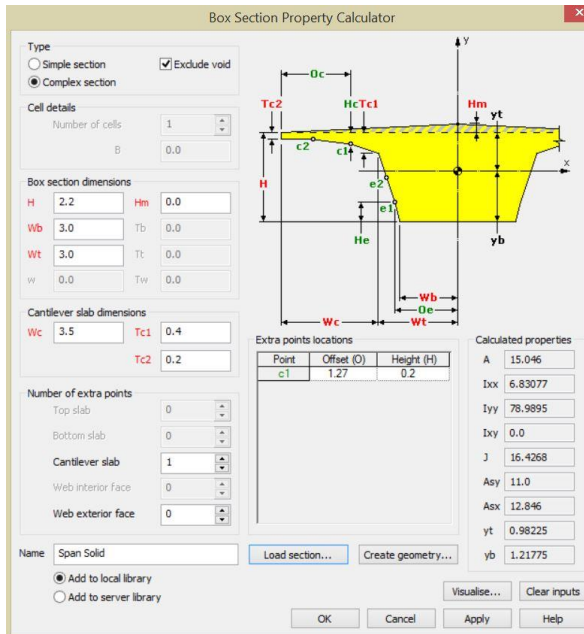


Figure 2.28 Solid span section properties.

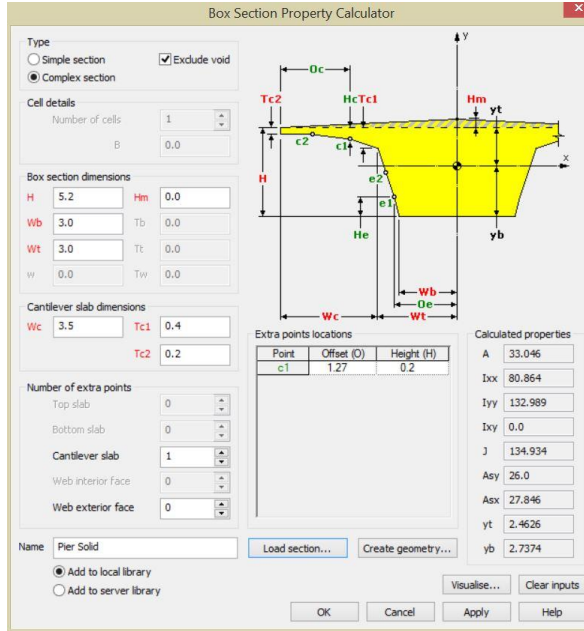


Figure 2.29 Solid pier section properties.

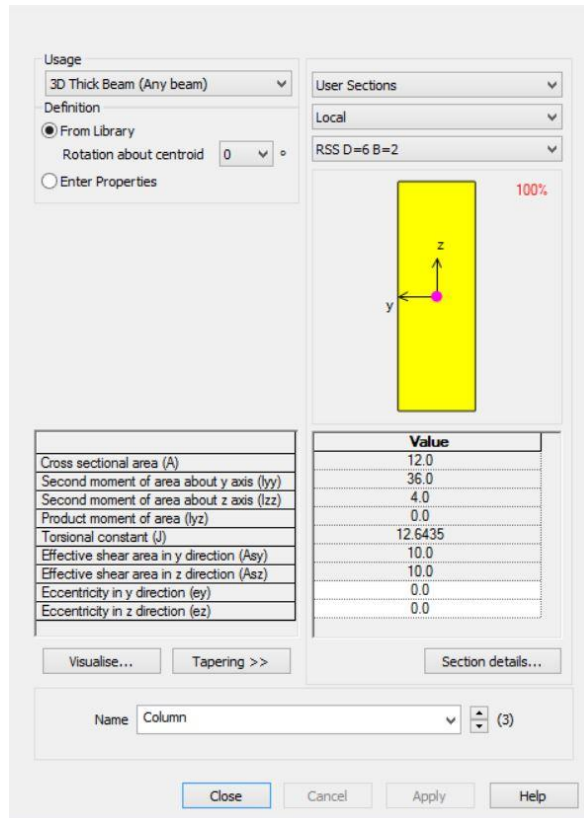
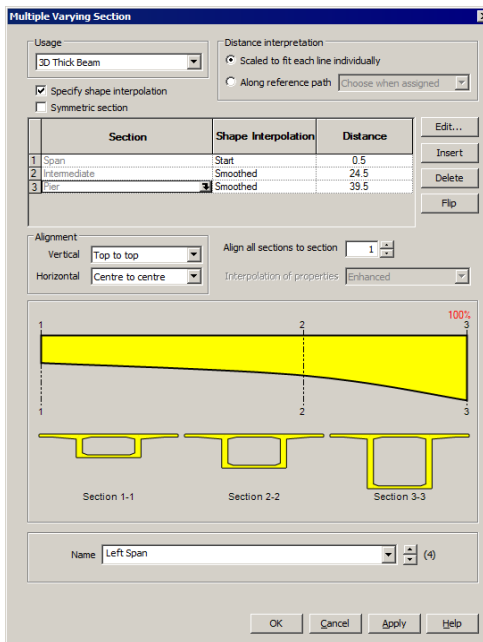
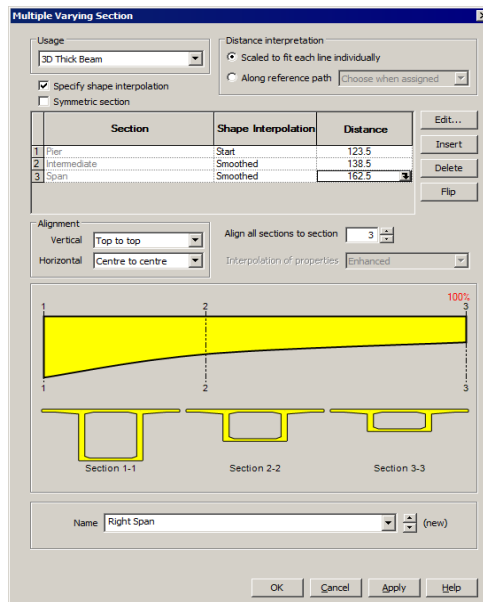


Figure 2.30 Column section properties.

A multiple varying geometric line attribute has been defined for the left-hand and right-hand span. This make use of the previously defined voided sections named Span, Intermediate and Pier as illustrated in Figures 2.31 and 2.32. The same procedure has been used to define the multiple varying section line properties of the Centre Span (Figure 2.33)



**Figure 2.31** Multiple varying section line properties for the Left Span.



**Figure 2.32** Multiple varying section line properties for the Right Span.

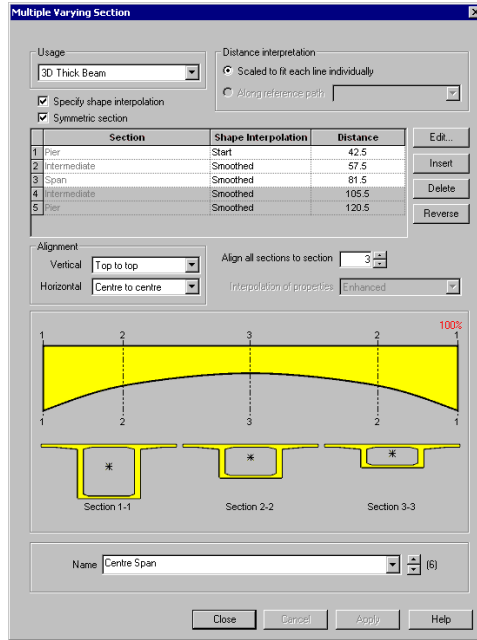


**Figure 2.33** Multiple varying section line properties for the Centre Span.

The damage bridge model has been defined using the same procedure. Depth of the box section has been decreased as illustrated in Figure 2.35 at four locations before and after each pier (see Figure 2.35) representing the damage in order to investigate its effect on modal parameters.

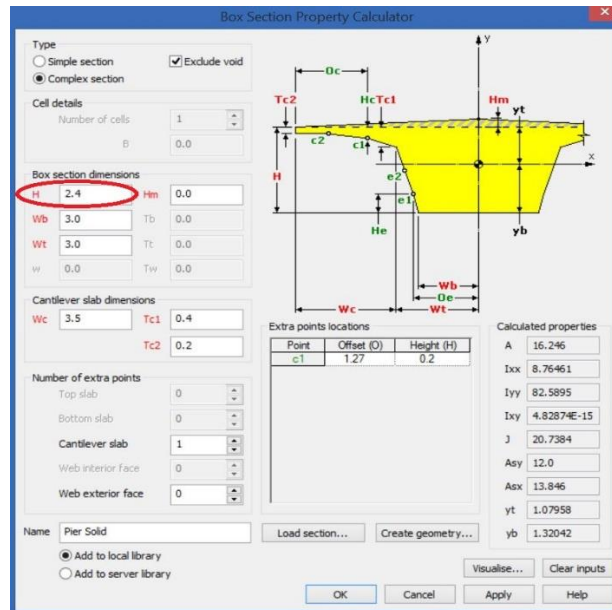


**Figure 2.34** Damaged section properties.

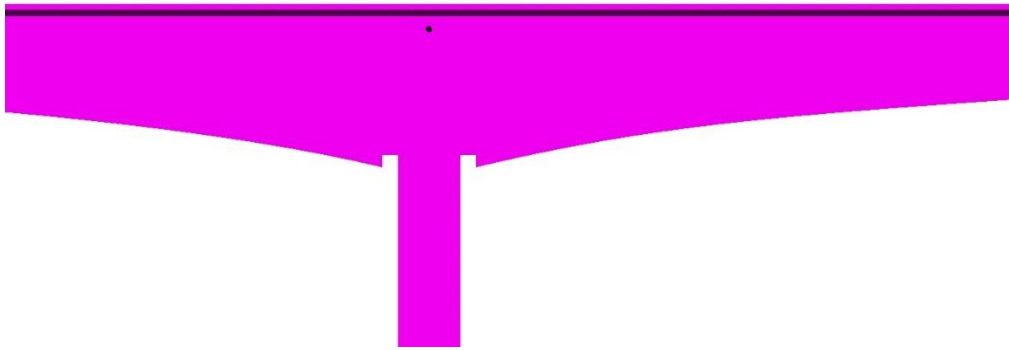


**Figure 2.35** Location of the damage.

### 2.4.3 Moving Load Analysis

In the first step, Eigenvalue controls are defined as properties of the loadcase as presented in Figure 2.36.

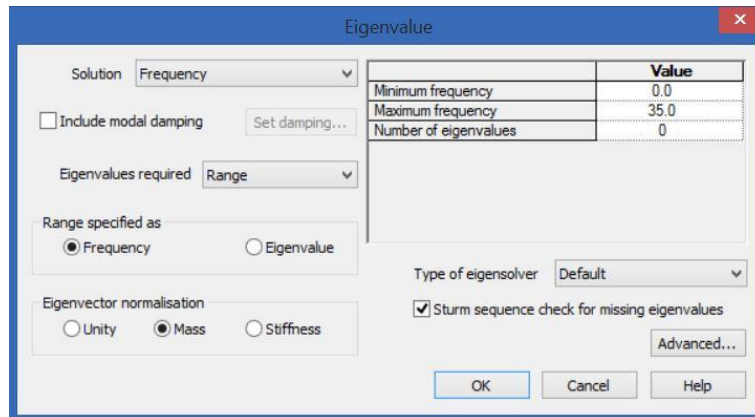


**Figure 2.36** Eigenvalue controls.

Afterwards, moving load calculations are performed using the IMDPlus facility. In order to carry out the moving load analysis of the truck travelling across the following three stages have been carried out:

- Defining the path along which the moving loads travel. For this bridge the unit axle load has been defined as a discrete point load called Unit Axle Load which defines the unit loading from a single axle of AASHTO LRFD design Truck (HS-20) (Figure 2.37) and acts vertically.



- Converting the loading along this path from this unit load into modal forces that are applied in the IMDPlus moving load analysis (see Figure 2.38)
- Running an IMDPlus moving load analysis to calculate the response of the bridge as shown in Figure 2.39.

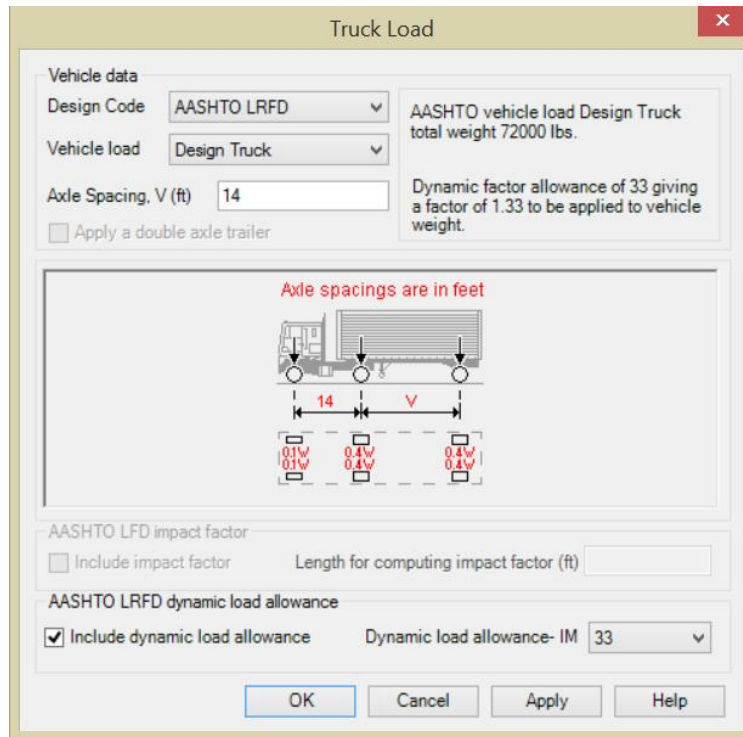


**Figure 2.37** HS-20 truck load.

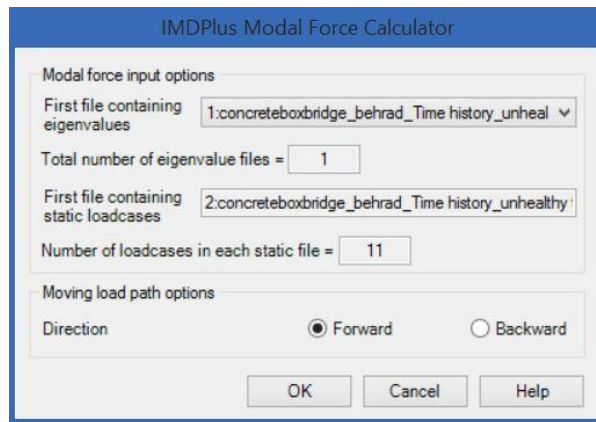


**Figure 2.38** IMDPlus modal force properties.

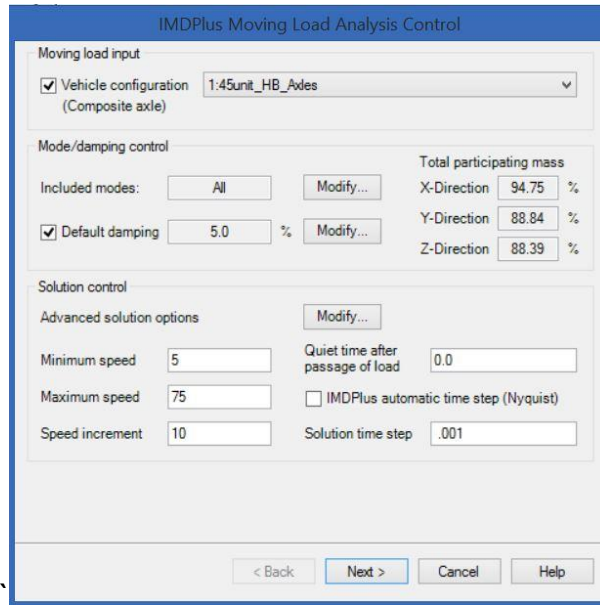


**Figure 2.39** IMDPlus moving load analysis control.

#### 2.4.4 Seismic Response Analysis

Seismic response of the bridge under El Centro grand motions (see Appendix C) has been examined in time domain. Seismic Response calculations are performed using the IMDPlus facility as well and involves defining the excitation and specifying the results required. The input for the seismic analysis is defined on the IMDPlus Seismic Analysis control dialog (see Figures 2.40 and 2.41). The input consists of the El Centro earthquake acceleration records, included modes and damping along with interpolation options.

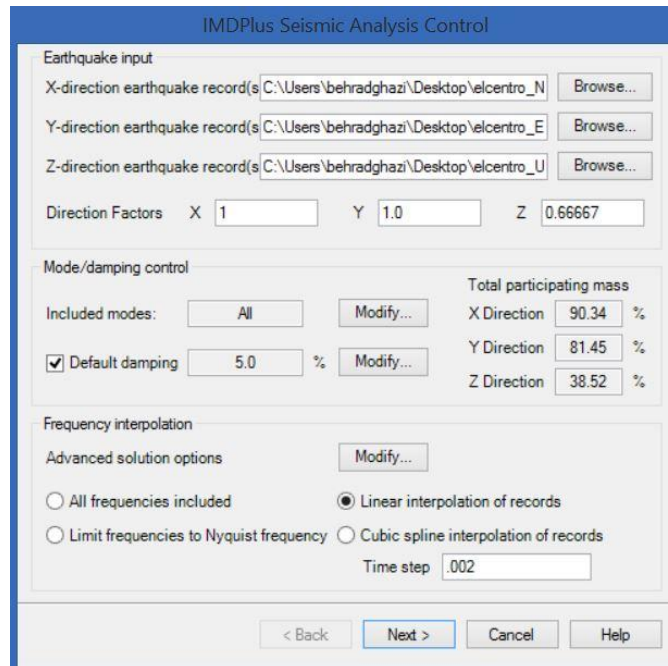


**Figure 2.40** IMDPlus Seismic Analysis control dialog.

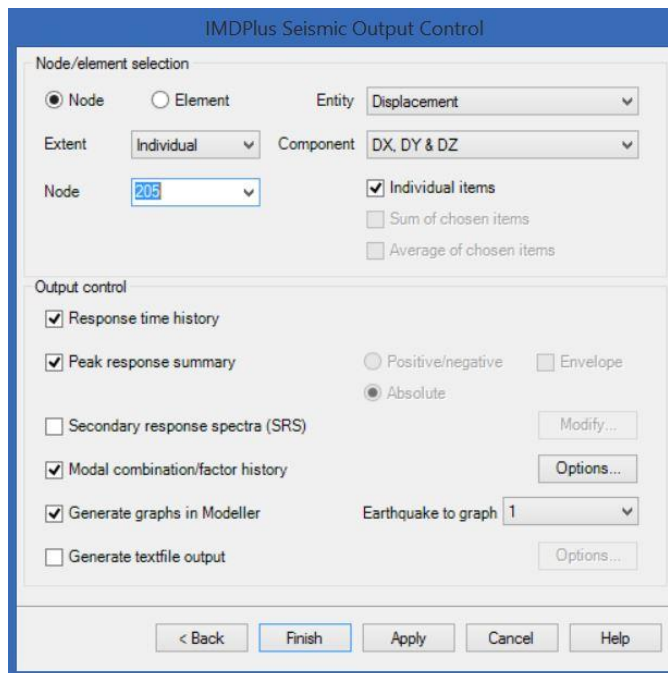


**Figure 2.41** IMDPlus Seismic output control.

### 2.4.5 Natural Frequency Analysis Results

The first 10 mode shapes obtained from eigenvalue frequency analysis are presented in Figures 2.42-2.51. The first, third, fourth, seventh and tenth vibrational modes are transverse modes. The second fifth, sixth and eighth modes are vertical modes and Ninth mode is torsional (see Figure 2.50). Eigenvalue results of the first 10 mode shapes for the whole structure are displayed in Table 2.6. Noting that the frequency in Hertz is obtained by dividing the square root of the eigenvalue by  $2\pi$ , and the period of vibration in seconds can be obtained using the reciprocal of frequency ( $1/\text{frequency}$ ). The error norm for a given mode provides a relative measure of the accuracy of the computed modes. A high error norm signifies inaccuracy in either the eigenvalue or the eigenvector, or both and will provoke a warning message in Lusas Bridge software.

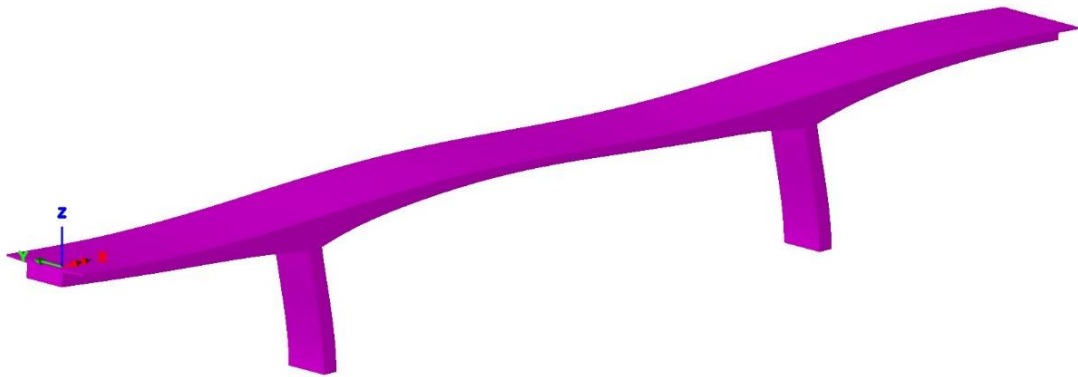


**Figure 2.42** The 1<sup>st</sup> mode shape (frequency: 1.41 Hz).

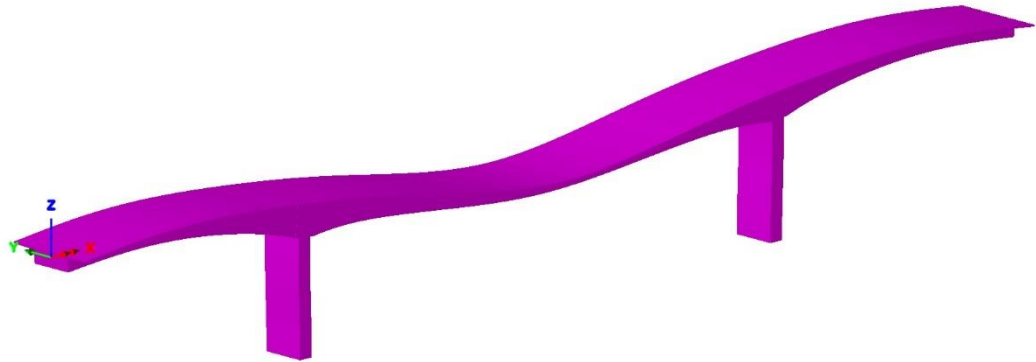


**Figure 2.43** The 2<sup>nd</sup> mode shape (frequency: 1.86 Hz).

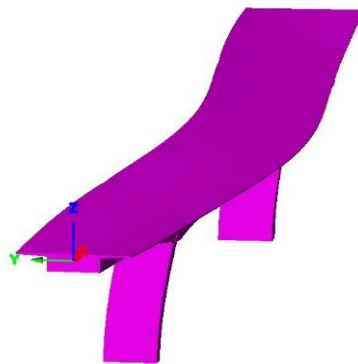


**Figure 2.44** The 3<sup>rd</sup> mode shape, plan view on top and 3D view at the bottom (frequency: 2.31 Hz).

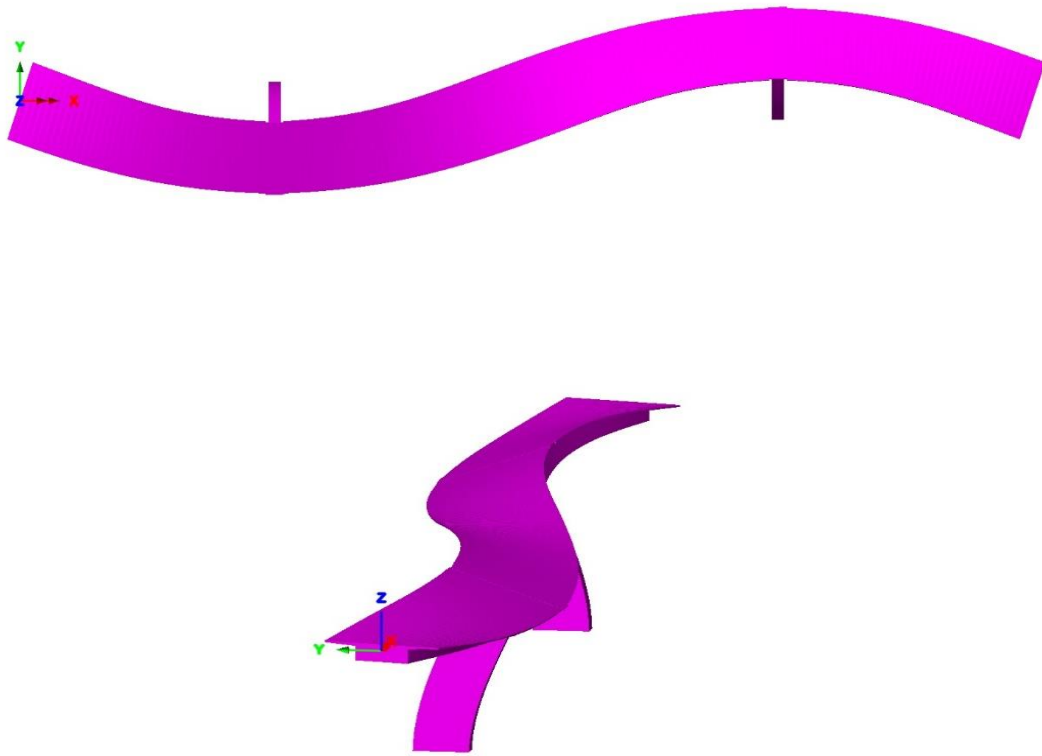


**Figure 2.45** The 4<sup>th</sup> mode shape, plan view on top and 3D view at the bottom.

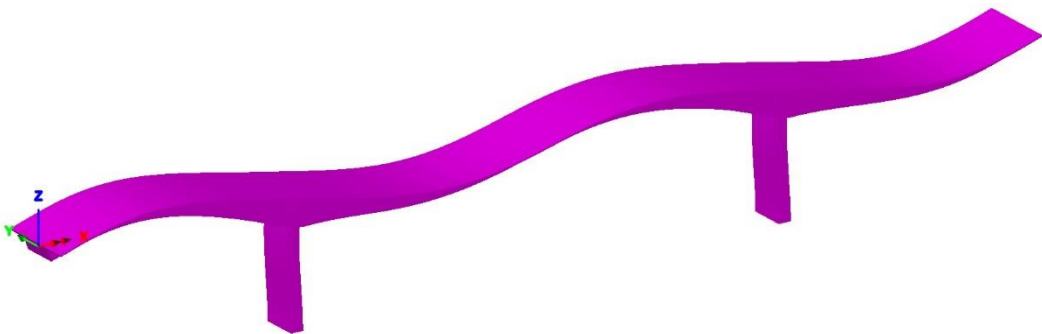


**Figure 2.46** The 5<sup>th</sup> mode shape.

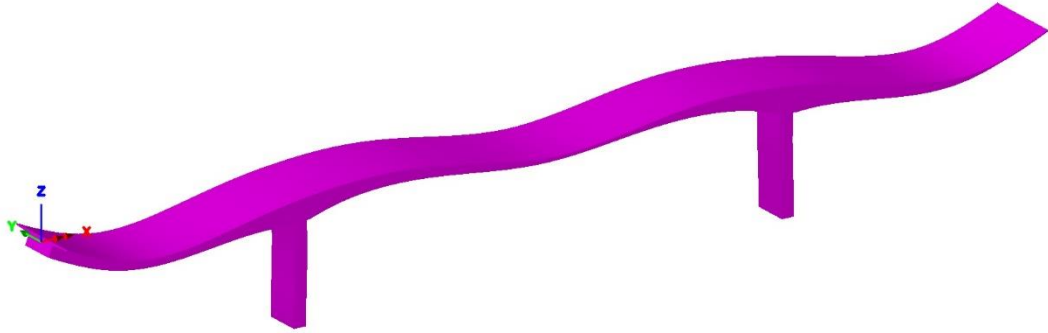


**Figure 2.47** The 6<sup>th</sup> mode shape.

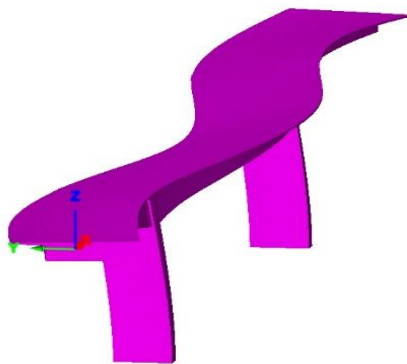


**Figure 2.48** The 7<sup>th</sup> mode shape, plan view on top and 3D view at the bottom .

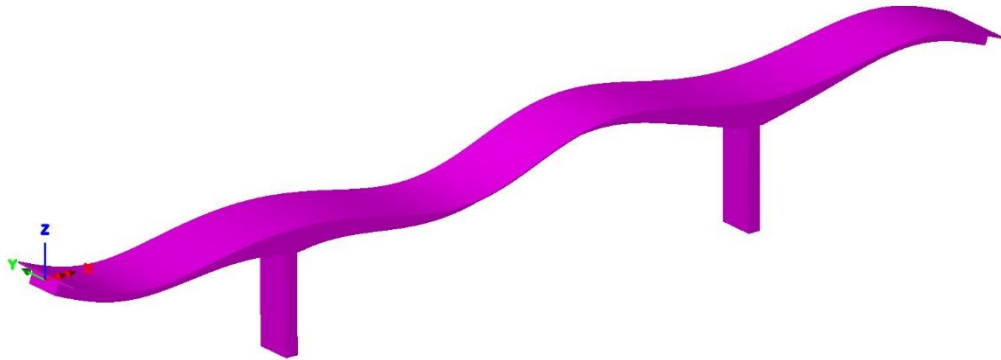


**Figure 2.49** The 8<sup>th</sup> mode shape.

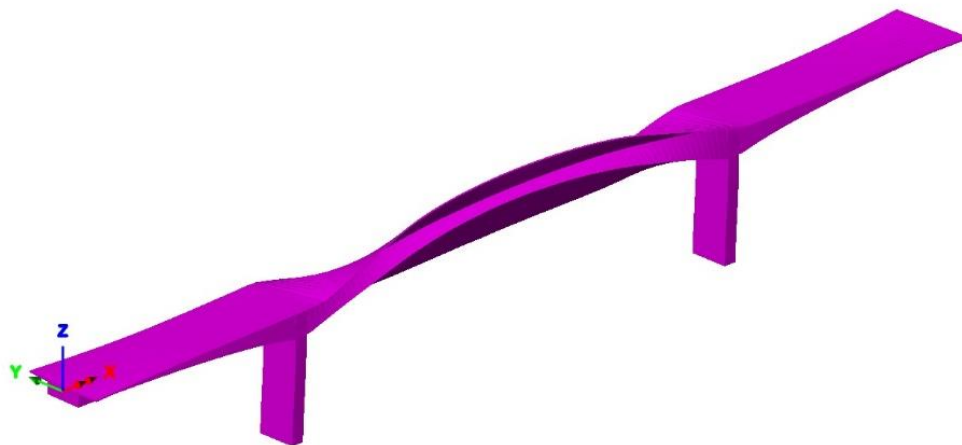


**Figure 2.50** The 9<sup>th</sup> mode shape ( Torsional ).



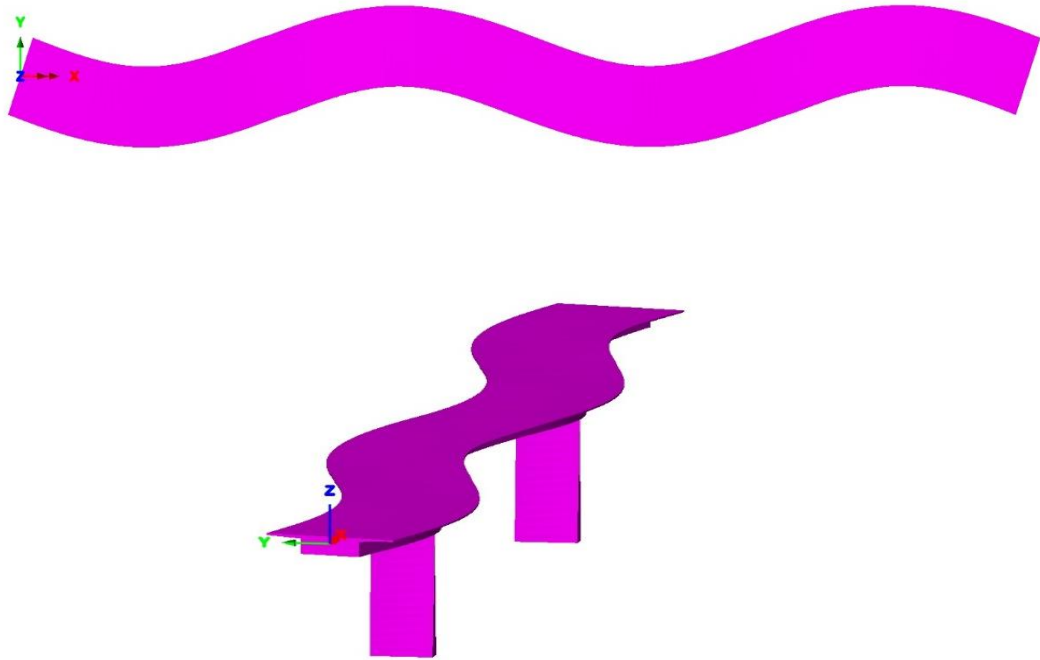


**Figure 2.51** The 10<sup>th</sup> mode shape.

**Table 2.6** Modal Frequencies of Concrete Box Section

<b>Mode</b>	<b>Eigenvalue</b>	<b>Frequency (Hz)</b>	<b>Error Norm</b>
<b>1</b>	787.77	1.41	0.107885E-09
<b>2</b>	136.93	1.86	0.362999E-10
<b>3</b>	211.02	2.31	0.268435E-10
<b>4</b>	580.96	3.84	0.242861E-10
<b>5</b>	601.71	3.90	0.851561E-11
<b>6</b>	964.71	4.94	0.121051E-10
<b>7</b>	1213.07	5.54	0.578849E-11
<b>8</b>	1614.49	6.39	0.892591E-11
<b>9</b>	2508.70	7.97	0.280746E-11
<b>10</b>	3352.68	9.215	0.267796E-11

## 2.4.6 Moving Load Analysis Results

Initially Moving Load Analysis has been carried out by moving the HS-20 truck over the bridge and the response of the mid-span of the bridge for the range of speeds selected is investigated. The displacements of the mid-span for a single speed of 15 m/s (or 54 kph) is presented in Figure 2.52. The vertical acceleration response of the mid-span for the same truck speed shown in Figure 2.53.

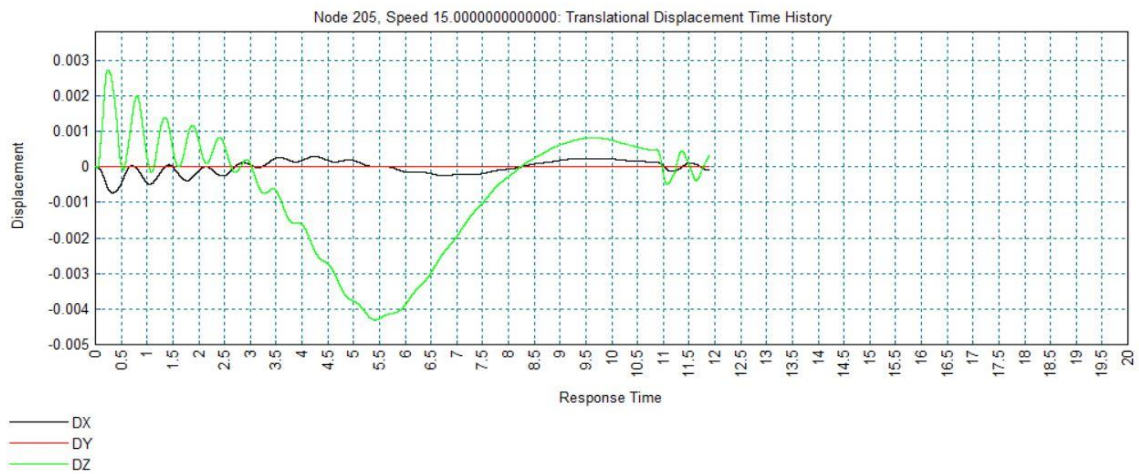


**Figure 2.52** Displacement time history of the mid-span for truck speed of 15 m/s, Displacement (meter) & Time (Seconds).

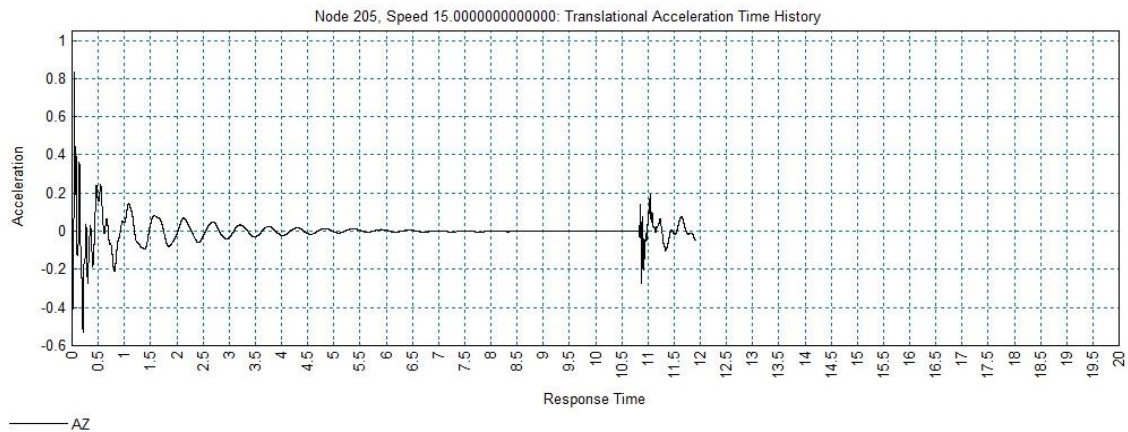


**Figure 2.53** Acceleration of the mid-span for truck speed of 15 m/s, Acceleration ( $m/s^2$ ) & Time (Seconds).

Previously, the displacement and acceleration response of the mid-span of the bridge deck for a single truck speed are illustrated. Now the peak positive and negative vertical displacement and acceleration responses of the mid-span over the speed range of 15 m/s to 75 m/s as specified previously in the moving load analysis control dialog will be shown in Figures 2.54 and 2.55.

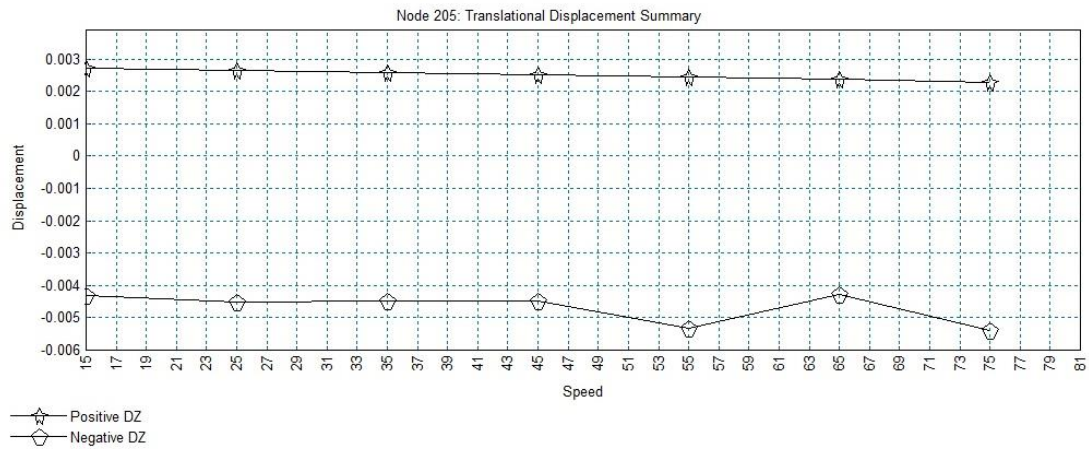


**Figure 2.54** Peak vertical displacement response of the mid-span over the speed range of 15 m/s to 75 m/s, Displacement (meter).

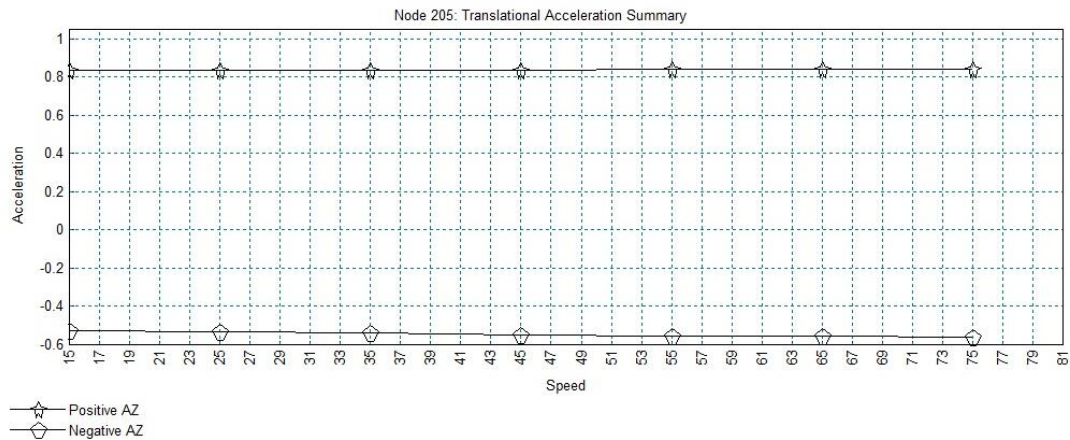


**Figure 2.55** Peak vertical acceleration response of the mid-span over the speed range of 15 m/s to 75 m/s, Acceleration ( $m/s^2$ ).

In the next step, HS-20 truck run over the bridge three times back and forth in order to obtain a time history displacement response with a longer duration. The displacements and vertical acceleration responses of the mid-span for a single speed of 15 m/s (or 54 kph) are presented in Figures 2.56 and 2.57.

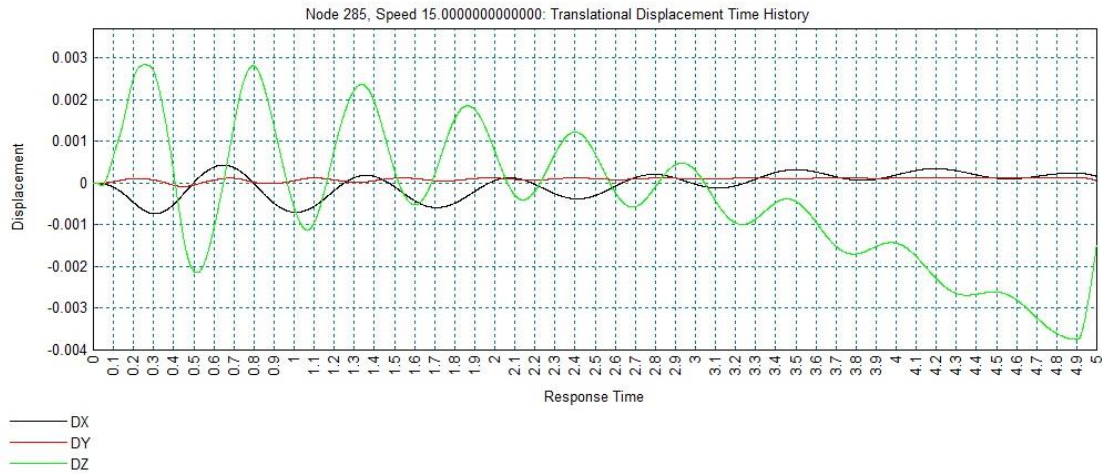


**Figure 2.56** Displacement time history of the mid-span for truck speed of 15 m/s, Displacement (meter) & Time (Seconds).

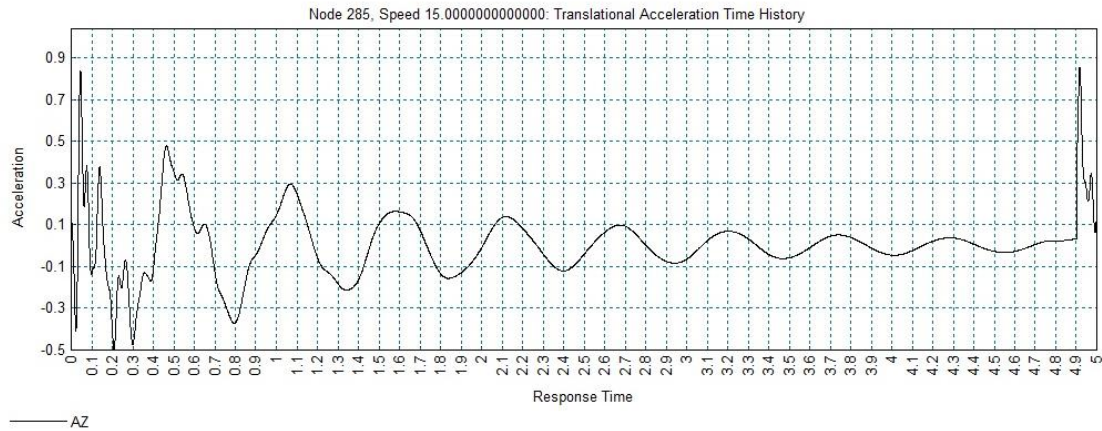


**Figure 2.57** Acceleration of the mid-span for truck speed of 15 m/s, Acceleration ( $m/s^2$ ) & Time (Seconds).

The displacement and acceleration response of the mid-span of the bridge deck for a single truck speed are illustrated. Furthermore, the peak positive and negative vertical displacement and acceleration responses of the mid-span over the speed range of 15 m/s to 75 m/s as specified previously in the moving load analysis control dialog will be shown in Figures 2.58 and 2.59.

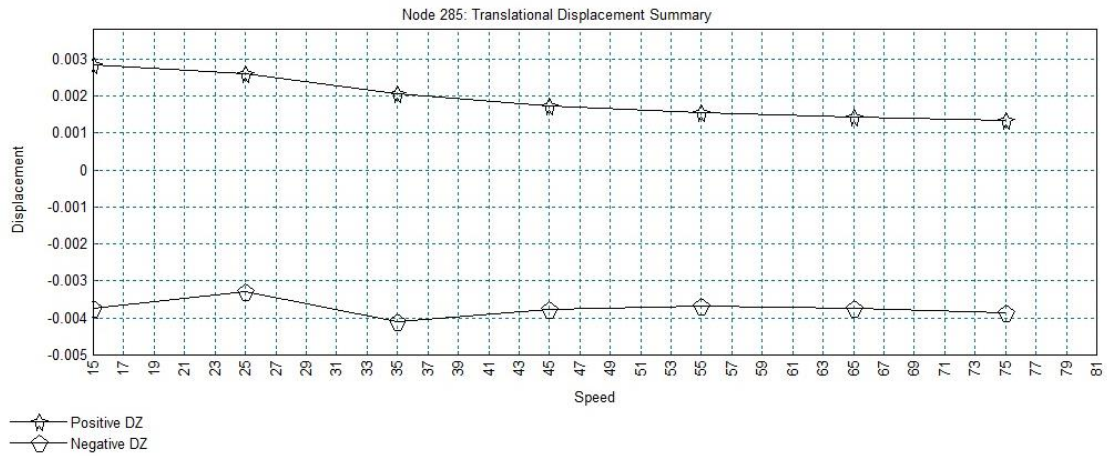


**Figure 2.58** Peak vertical displacement response of the mid-span over the speed range of 15 m/s to 75 m/s, Displacement (meter).

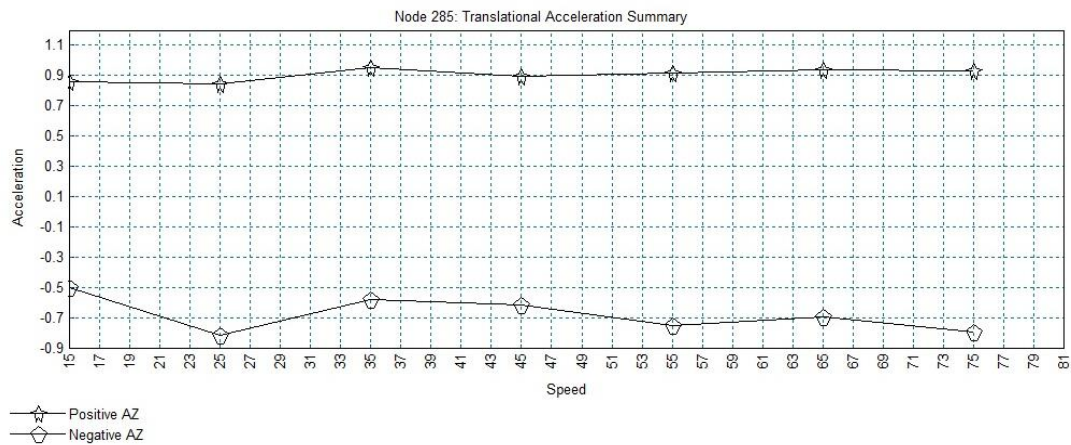


**Figure 2.59** Peak vertical acceleration response of the mid-span over the speed range of 15 m/s to 75 m/s, Acceleration ( $m/s^2$ ).

### 2.4.7 Seismic Response Analysis Results

Seismic Response of the bridge under El Centro earthquake ground motion is presented in this section. The displacement of the mid-span of the bridge deck has been shown in Figure 2.60. Peak displacements are also output to Notepad and indicate absolute peak displacements of 0.0079 m in the X-direction, 0.0039 m in the Y-direction along with additional output for the Z-direction and rotations about each of these axes as presented in Figure 2.61. From this output we can identify times of 2.652 seconds and 2.03 seconds which correspond to the absolute peak displacements in the X and Y directions respectively.

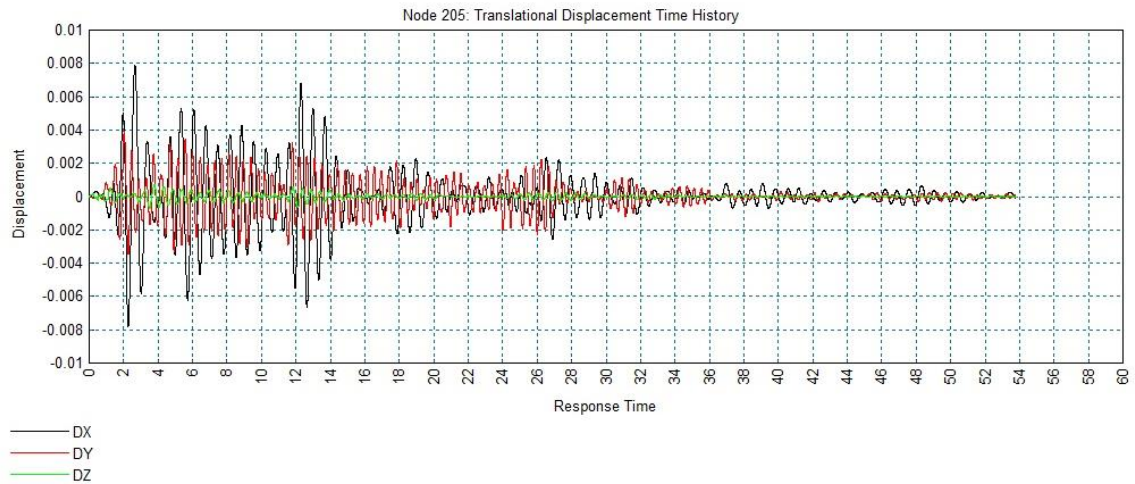


**Figure 2.60** Displacement time history of the mid-span under El Centro earthquake, Displacement (meter) & Time (Seconds).

# Entity	Time	Value
Peak_Pos_DX	2.652000000	0.7891669245E-002
Peak_Neg_DX	2.266000000	-0.7795712057E-002
Abs_Peak_DX	2.652000000	0.7891669245E-002
Peak_Pos_DY	2.030000000	0.3903998036E-002
Peak_Neg_DY	2.274000000	-0.3440177035E-002
Abs_Peak_DY	2.030000000	0.3903998036E-002
Peak_Pos_DZ	3.768000000	0.7127761721E-003
Peak_Neg_DZ	3.502000000	-0.7333823736E-003
Abs_Peak_DZ	3.502000000	0.7333823736E-003
Peak_Pos_THX	2.270000000	0.1389062526E-003
Peak_Neg_THX	2.012000000	-0.1421302582E-003
Abs_Peak_THX	2.012000000	0.1421302582E-003
Peak_Pos_THY	2.276000000	0.1645769886E-003
Peak_Neg_THY	2.664000000	-0.1566897377E-003
Abs_Peak_THY	2.276000000	0.1645769886E-003
Peak_Pos_THZ	1.232000000	0.1431122188E-012
Peak_Neg_THZ	1.180000000	-0.1468654499E-012
Abs_Peak_THZ	1.180000000	0.1468654499E-012
Abs_Peak_RSLT	2.268000000	0.8511753403E-002

**Figure 2.61** Peak displacements output, Displacement Value (meter) & Time (Seconds).

## 2.5 Analysis of 6-Span Precast Segmental Box Girder Bridge

### 2.5.1 Description of the Bridge

The investigated structure is a six-span precast segmental box girder bridge with a total length of approximately 250 m (820 ft.) and a width of 12.30 m (40 ft.). It carries two east-bound and two west-bound lanes. The bridge is located in Qatar. Figure 2.62 provides an aerial view of the bridge site and Figure 2.63 shows a side view of the bridge structure. The superstructure consists of a post-tensioned concrete box girder system with three central spans of 46 m each, 1 central span of 40 m and two shorter end spans of 37 m and 34 m. Thickness of the deck and sections heights are respectively 0.25m and 2.00m with 50mm wearing surface, as shown in Figure 2.64.



**Figure 2.62** Aerial Photo of the bridge.

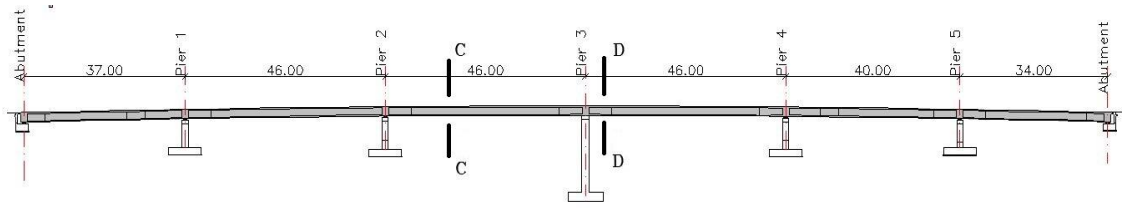
The substructure consists of five column piers and two stub abutments. Concrete with compressive strength of 25 Mpa (3600 psi) and 20 Mpa (3000 psi) used for piers and foundation. Mechanically Stabilized Earth (MSE) walls were used behind the existing



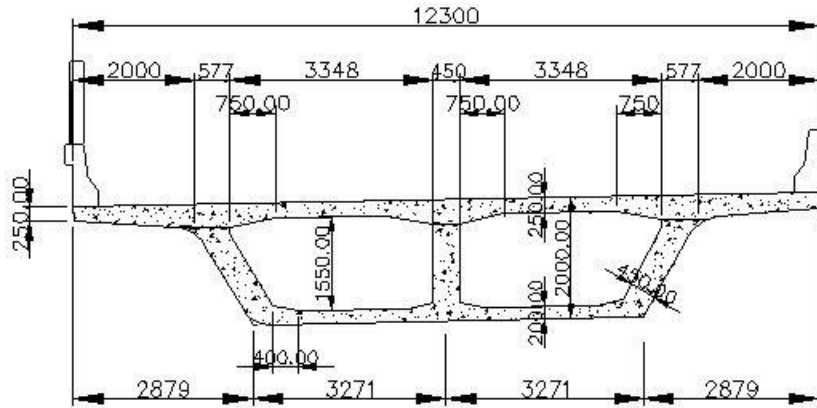
abutments because of poor soil conditions. The MSE walls are supported on 1.00 m diameter cast in place concrete piles with design capacity of 4500 kN and rested on bedrock. All existing pier piles have been driven vertically. From both ends, abutments separate the bridge from the road approach with expansion joints. The box-girder system is resting on elastomeric bearings. Piers 2 and 3 have fixed bearings, while sliding guided bearings are used for the rest of piers and abutments. Rotation of bearings are less than 0.02 (Rad.) for both longitudinal and transverse directions. All the Foundations were designed to a net allowable bearing pressure of 600 kN/m<sup>2</sup>. The bridge crosses Qatar Expressway on 15 degrees skewed alignment. A concrete parapet with a bridge railing and sound wall is placed along the south edge of the bridge. The bridge was opened for traffic in 2011.



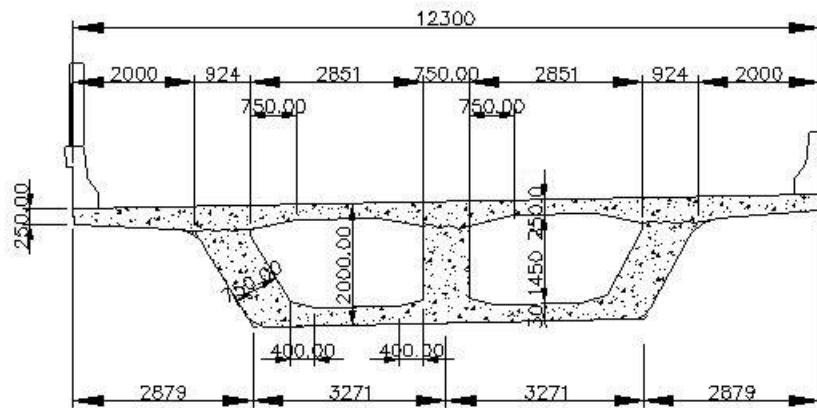
**Figure 2.63** Side view of the bridge.



a) Bridge elevation



Section B-B



Section D-D

c) Cross sections of concrete box girders

Figure 2.64 Geometry of the bridge.

### **2.5.2 Modeling Description**

A complete analysis using Lusas Bridge software requires a description of the material, the model configuration, boundary conditions, and loading. For service-load simulations, at least two material constants are required to characterize the linear elastic behavior of the material: Young's modulus ( $E$ ) and Poisson's ratio ( $\nu$ ). For nonlinear analysis, the steel and concrete uniaxial behaviors beyond the elastic range must be defined to simulate their behavior at higher stresses. The minimum input parameters required to define the concrete material are the uniaxial compression curve, the ratio of biaxial and uniaxial compressive strength, and the uniaxial tensile strength. Lusas is equipped with default values if necessary, which are indicative of typical concrete performance. Boundary conditions that represent structural supports specify values of displacement and rotation variables at appropriate nodes.

The bridge Finite Element model has been completed by employing all of the finite element strategies discussed in earlier sections. Despite the fact that experimental data were not yet available for comparison, it was useful to complete a model and conduct a detailed analysis for such a configuration. The features involved included the following procedures.

### **2.5.3 Geometry**

The 6-Span Precast Segmental Box Girder Bridge is modelled using the box section property calculator and the multiple varying sections facilities in LUSAS (Figure 2.65). Units used are kN, m, kg, s, C throughout.

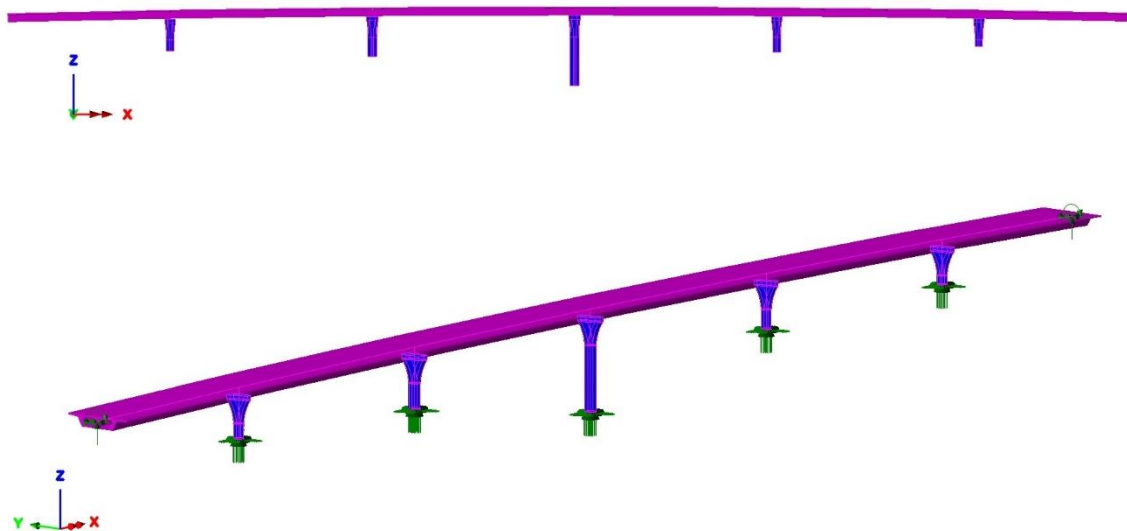


**Figure 2.65** Precast Segmental Box Girder Bridge modeled in Lusas Bridge Plus software.

Bridge Deck has been modeled by defining geometric lines and assigning a line mesh of thick beam elements to them. For modeling the varying section, similar procedure to the previous bridge model has been utilized by defining a basic beam as a 'Flat' model with three central spans of 46 m each, one central span of 40 m and two shorter end spans of 37 m and 34 m formed of single vertically curved lines. Afterwards, geometric line attributes are assigned to the single lines along with other section properties. Fixed supports restrain the piers and roller supports restrain the ends of the deck.

Cross-section properties for four voided box sections that are used in six spans are defined which shown in Figures 2.66-2.69 utilizing the Complex section option and Solid sections has been modeled by excluding voids from previous sections (see Figures 2.70 and 2.71).

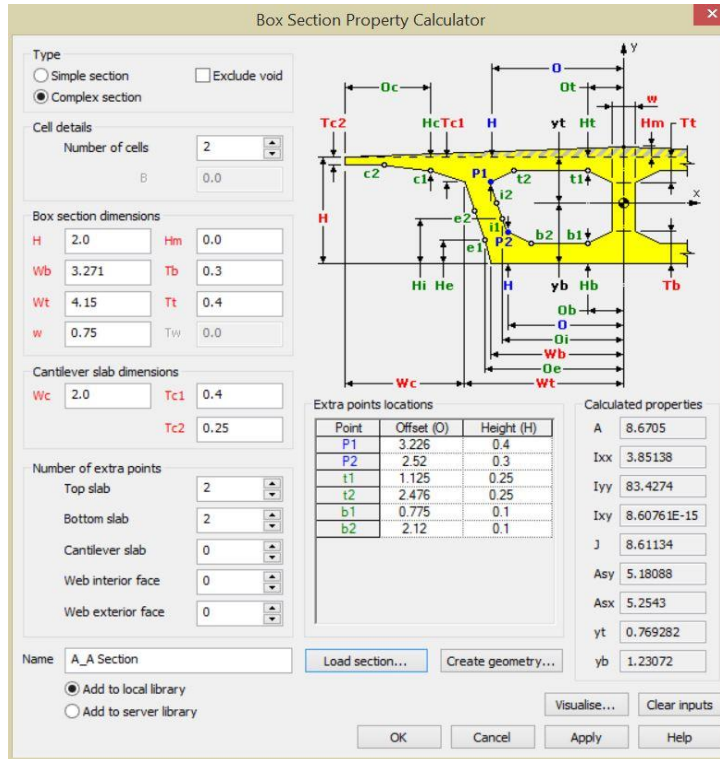


Figure 2.66 Properties of A\_A section adjacent to the abutments.

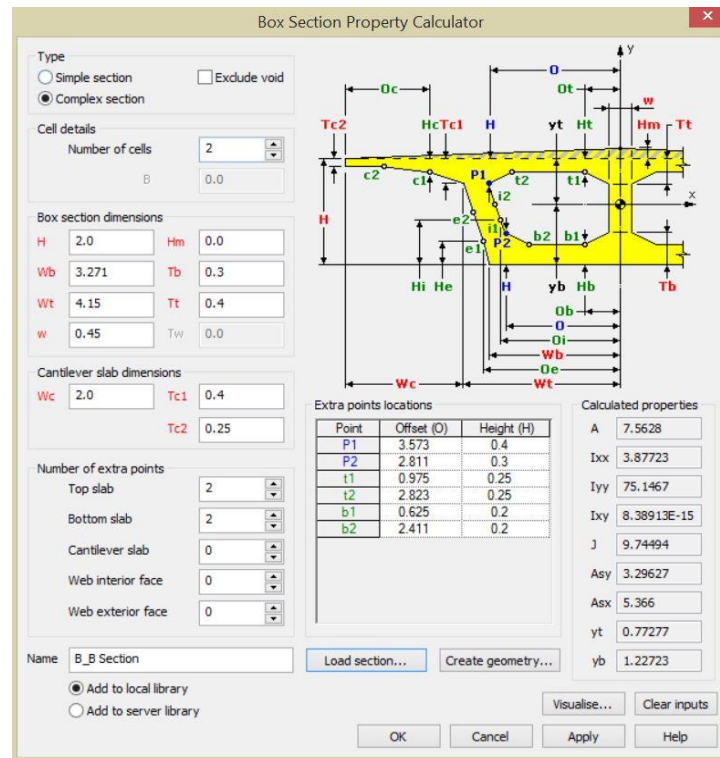


Figure 2.67 Voided B\_B section properties.

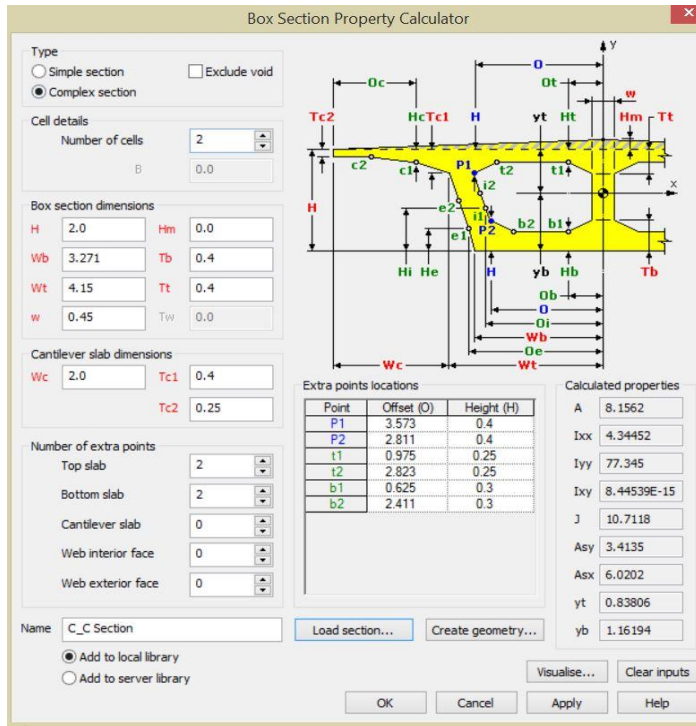


Figure 2.68 Voided C\_C section properties.

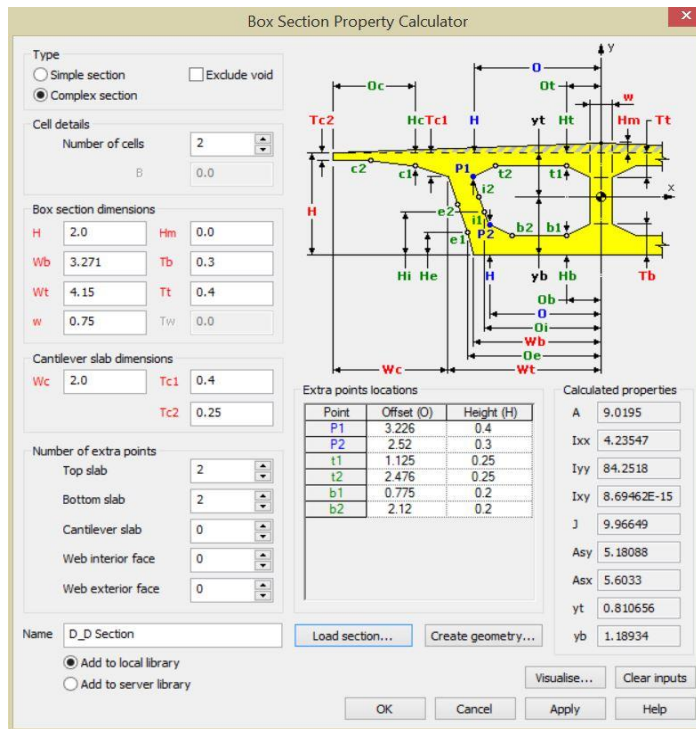


Figure 2.69 Voided D\_D section properties.

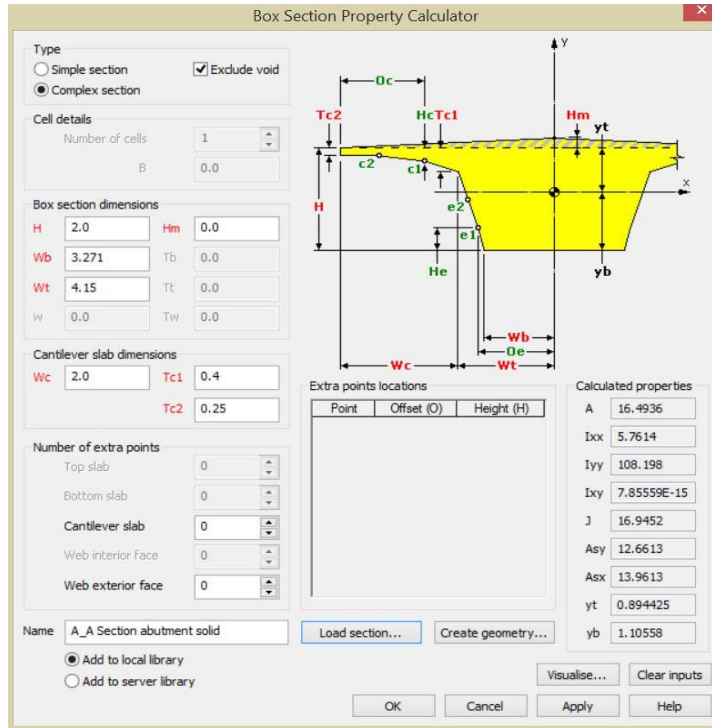


Figure 2.70 Solid section properties at abutments.

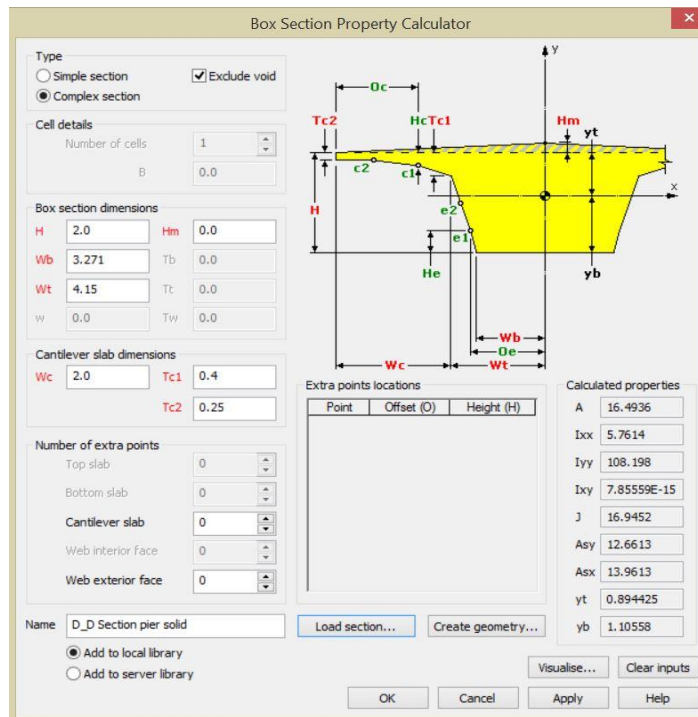
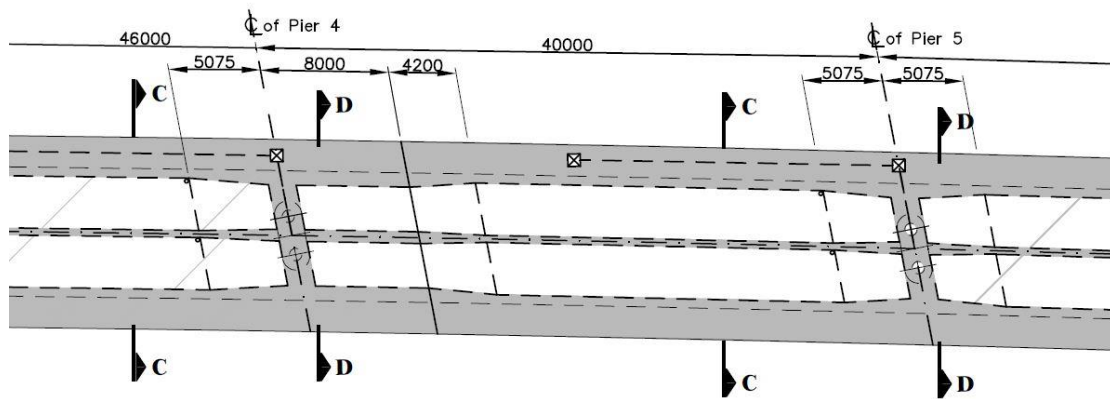


Figure 2.71 Solid section properties at piers.

A Multiple varying geometric line attribute has been defined for each span with respect to changes of concrete box sections in the plans (for instance see Figure 2.72 for 5th span between pier 4 and 5 ). This make use of the previously defined voided sections as illustrated in Figures 2.73 and 2.74 for this span. The same procedure has been used to define the multiple varying section line properties of the other Spans.



**Figure 2.72** Varying section of the bridge.



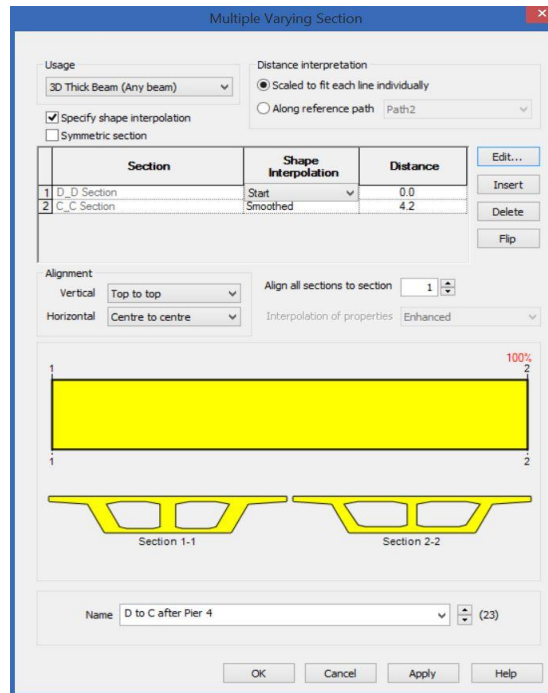


**Figure 2.73** Multiple varying section line properties for 5<sup>th</sup> span (transition from D\_D section to C\_C).

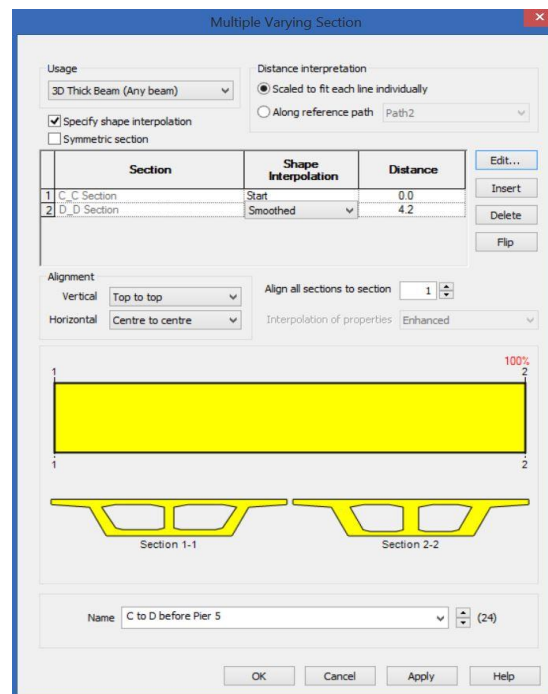


**Figure 2.74** Multiple varying section line properties for 5<sup>th</sup> span (transition from C\_C section to D\_D).

Unique Architectural design of the bridge piers makes its FE modeling demanding. Piers have similar structural configuration but various dimensions. Therefore, Geometry of each pier modeled separately by defining volumes as shown in Figure 2.75. Then attributes such as material and mesh types are assigned to the volumes (illustrated in Figure 2.76). 3D Solid Continuum Elements TH4 and PN6 has been used to model the piers as presented in Table 2.7. The complete model had 10,692 elements, separated into 9,172 3D solid elements, 1,520 3D thick beam elements constituting the deck.

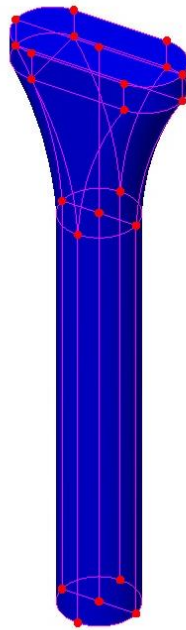


**Figure 2.75** Bridge piers geometry.

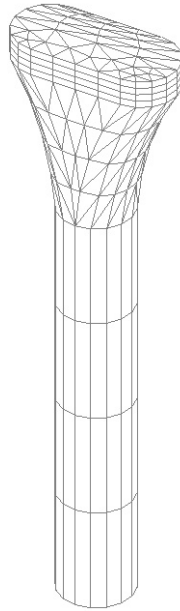


**Figure 2.76** Bridge piers Mesh.

**Table 2.7** 3D Solid Continuum Elements TH4 and PN6 description

General	TH4	PN6
<b>Element Group</b>	3D Solid Continuum	
<b>Element Description</b>	A family of 3D isoparametric solid continuum elements with higher order models capable of modelling curved boundaries. The elements are numerically integrated.	
<b>Number Of Nodes</b>	4 for tetrahedra. The elements are numbered according to a right-hand screw rule in the local z-direction.	
<b>Freedom</b>	U, V, W: at each node.	
<b>Notes</b>	The elements are based on the standard isoparametric approach. The variation of stresses within an element may be regarded as constant for the lower order elements (corner nodes only), and linear for the higher order elements (with mid-side nodes).	

## 2.5.4 Material

Development of a model for the behavior of concrete is a challenging task. Concrete is a quasi-brittle material and has different behavior in compression and tension. The tensile strength of concrete is typically 8-15% of the compressive strength [20]. Figure 2.77 shows a typical stress-strain curve for normal weight concrete [21].

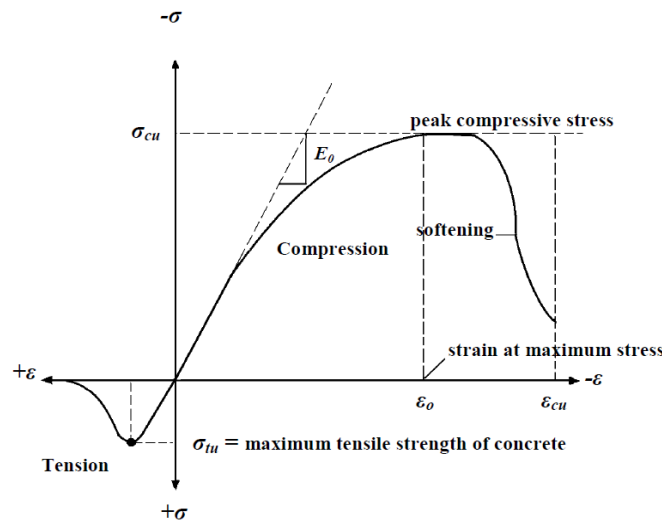


**Figure 2.77** Typical uniaxial compressive and tensile stress-strain curve for concrete [21].

In compression, the stress-strain curve for concrete is linearly elastic up to about 30 percent of the maximum compressive strength. Above this point, the stress increases gradually up to the maximum compressive strength. After it reaches the maximum compressive strength  $\sigma_{cu}$ , the curve descends into a softening region, and eventually crushing failure occurs at an ultimate strain  $\epsilon_{cu}$ . In tension, the stress-strain curve for concrete is approximately linearly elastic up to the maximum tensile strength. After this point, the concrete cracks and the strength decreases gradually to zero [21].

For concrete, Lusas Bridge software requires input data for material properties as represented in Figure 2.78.

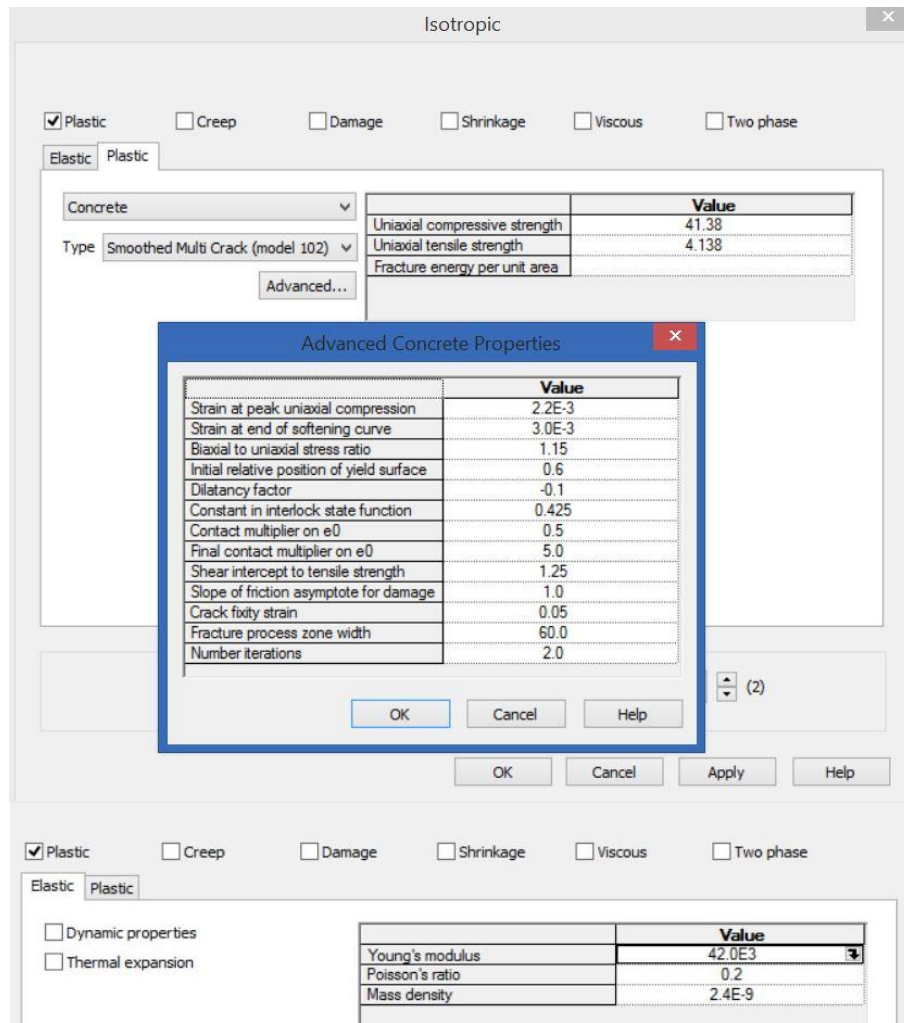


**Figure 2.78** Concrete material properties.

### 2.5.5 Defining the Loads

Three loadcases will be defined Based on AASHTO LRFD specifications:

- The self-weight of the bridge.
- A Lane load equivalent to a traffic load over the full length and width of the traffic lane.
- A design truck moving load over the full length of the bridge.

**2.5.5.1 Self-weight** The self-weight is defined as a gravity acceleration in the negative Z direction. The correct units are automatically calculated when the gravity loading is selected from the bridge menu.

**2.5.5.2 Lane Load** The second load will represent a lane load along the traffic lanes as shown in Figures 2.79 and 2.80. In Lusas Bridge Plus software, Vehicle and Lane loads are represented by Patch loads that are assigned to points which may form part of the model, or may be defined specifically to locate the bridge loads.

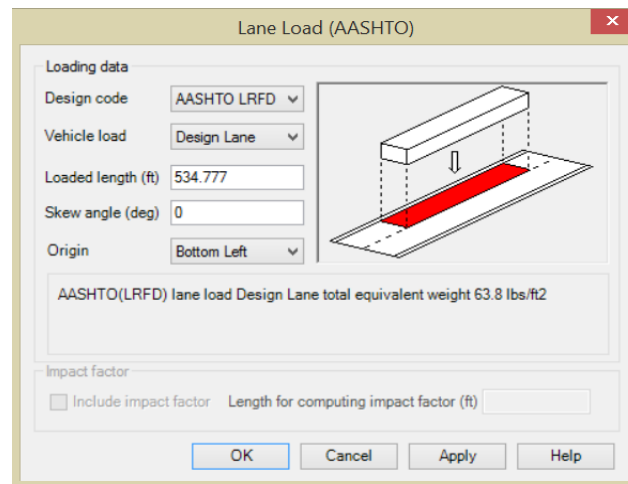


**Figure 2.79** AASHTO LRFD design lane load description.

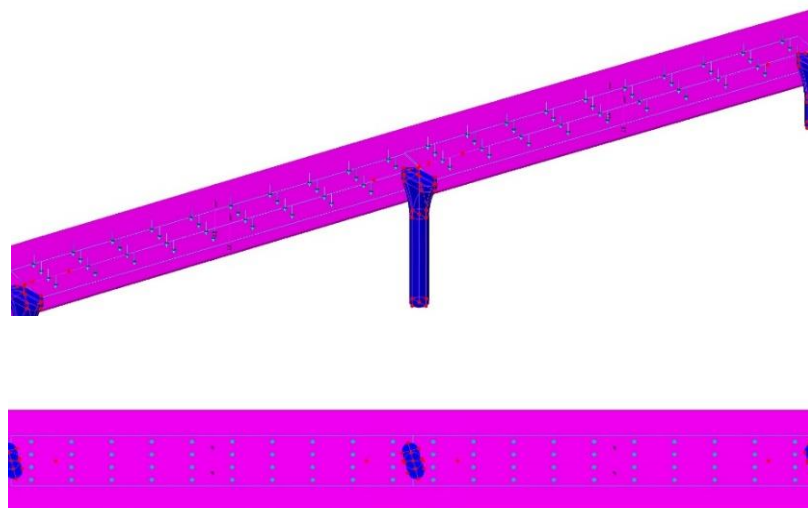


**Figure 2.80** AASHTO LRFD design lane load applied to the bridge model.

**2.5.5.3 Moving Load** The moving vehicle is assigned to the points using the moving load generator (see Figure 2.81). To use this facility a line defining the path of the vehicle is created. Based on AASHTO LRFD design specification HS-20 truck has been used as the moving vehicle which is shown in Figure 2.82. Moving loads on the model are visualized in Figure 2.83.

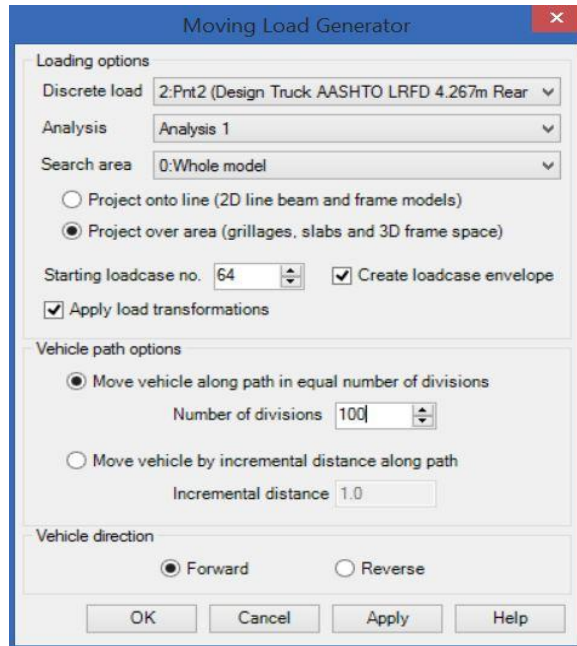


**Figure 2.81** Moving load generator.

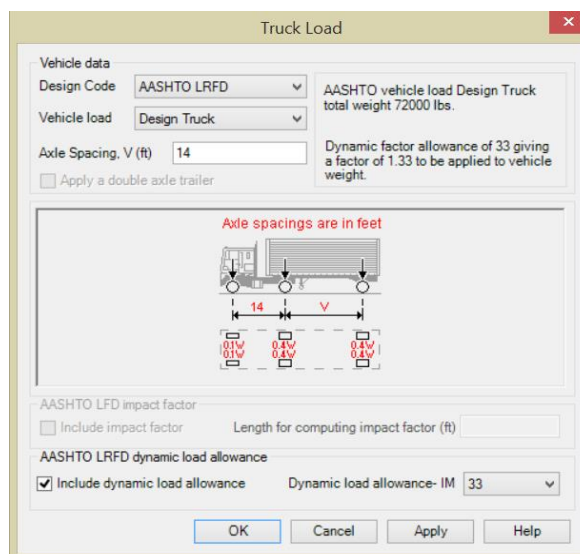


**Figure 2.82** AASHTO LRFD HS-20 truck load.

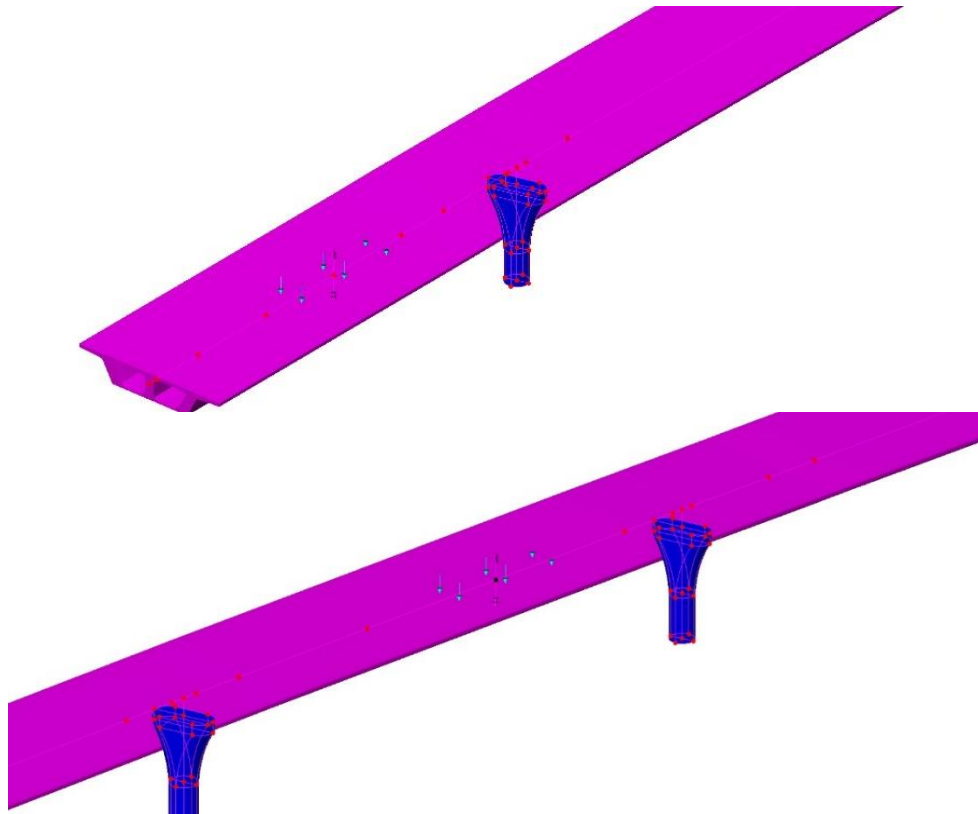


**Figure 2.83** Moving HS-20 truck on the bridge FE model.

In the Last step, Eigenvalue controls are defined as properties of the loadcase.

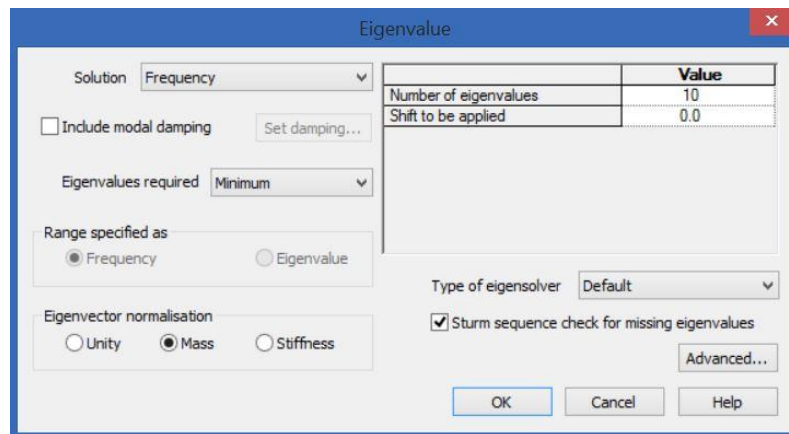


**Figure 2.84** Eigenvalue controls.



### 2.5.6 Analysis Results

Static and Dynamic Finite Element analysis of 6-Span Precast Segmental Box Girder Bridge has been carried out as presented in the last section. The data show the global behavior of the bridge model, particularly the distribution of moments and stresses in the deck. The deformed shape of the bridge under gravity load, AASHTO LRFD design lane load and HS-20 moving truck have been shown in Figures 2.85-2.87. The bridge has Maximum deflection of 2cm and 1.9cm under Dead load and Live Load respectively. Maximum Positive and Negative Displacement Envelope of each node has been illustrated in Figures 2.88 and 2.89 as the HS-20 truck moves over the bridge.

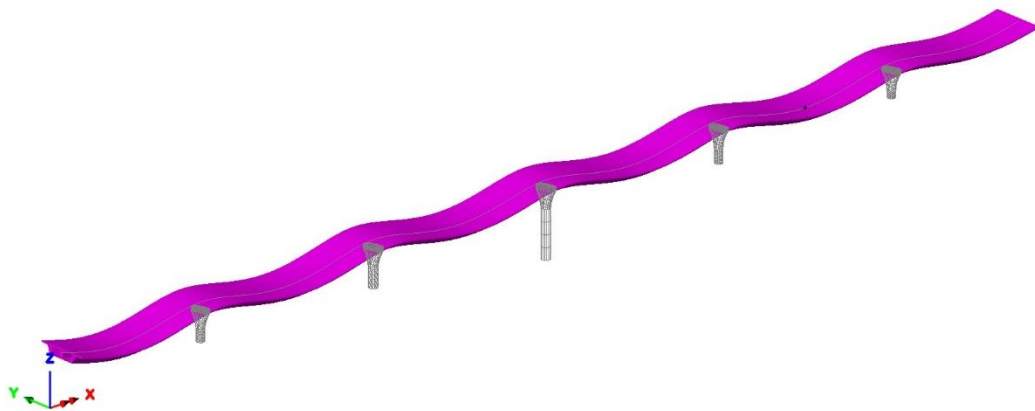


**Figure 2.85** Deformed mesh under gravity Load (max displacement 0.02 m).

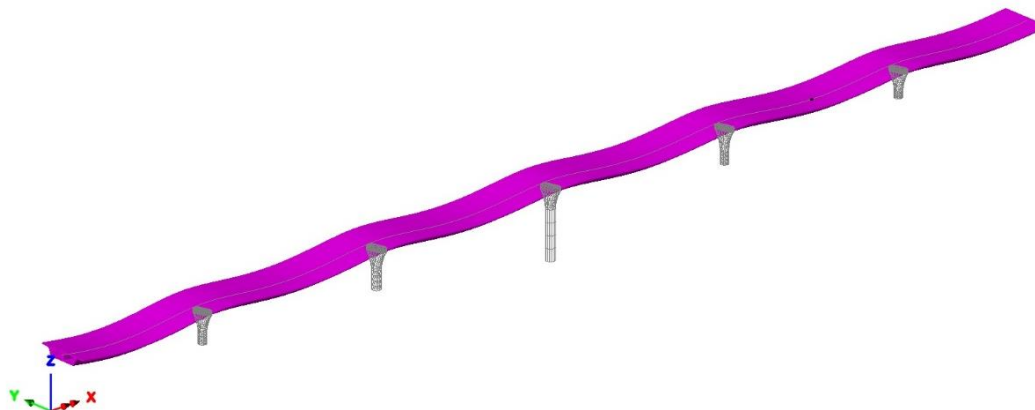


**Figure 2.86** Deformed mesh under Lane Load (max displacement 0.0018 m).

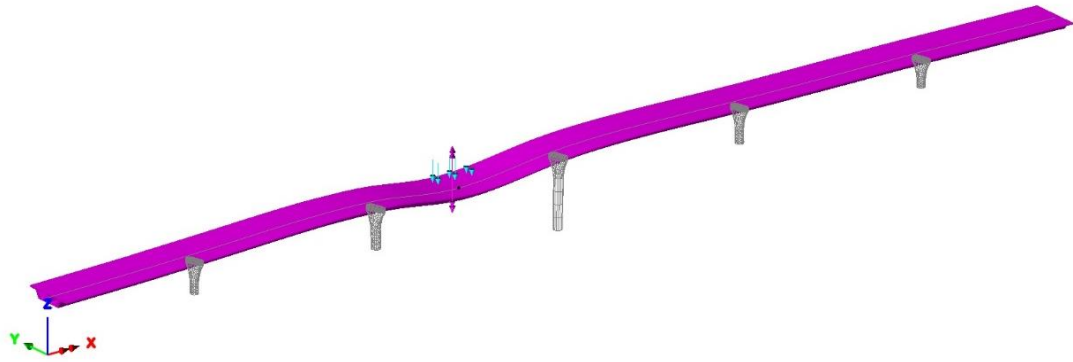


**Figure 2.87** Deformed mesh under HS-20 truck load (max displacement 0.0017 m for this case).

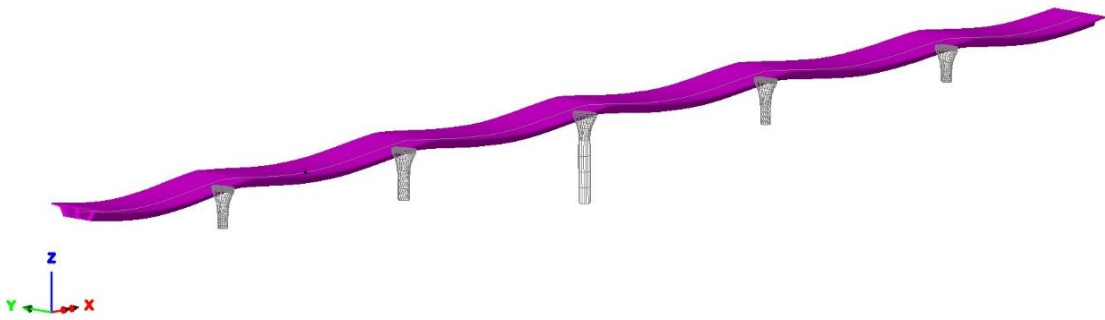


**Figure 2.88** Deformed Mesh for positive displacement envelope under HS-20 truck moving load (max displacement 0.0019 m).

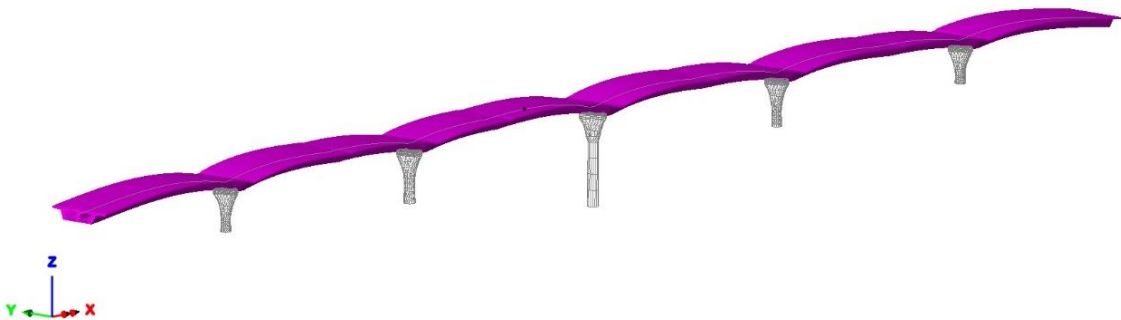


**Figure 2.89** Deformed Mesh for negative displacement envelope under HS-20 truck moving load (max displacement 0.0005 m).

Furthermore, Moment Diagrams under different Load cases have been shown in Figures 2.90-2.92. For the case of HS-20 truck moving load, positive and negative Moment Diagram envelopes have been presented in Figures 2.93 and 2.94. Figures 2.95-2.98 illustrate Stress Contours of the deck and piers as a result of gravity load, lane load and moving HS-20 truck load applied to the bridge model.

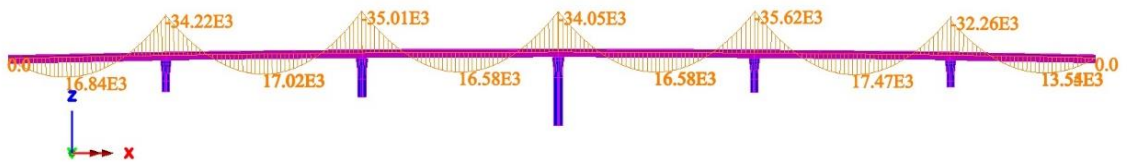


**Figure 2.90** Moment Diagram under gravity load (max positive moment  $17.47 \times 10^3$  kN.m and max negative moment  $-35.61 \times 10^3$  kN.m).

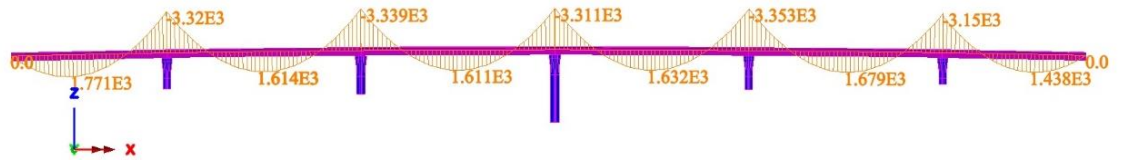


**Figure 2.91** Moment Diagram under lane load (max positive moment  $1.77 \times 10^3$  kN.m and max negative moment  $-3.35 \times 10^3$  kN.m).

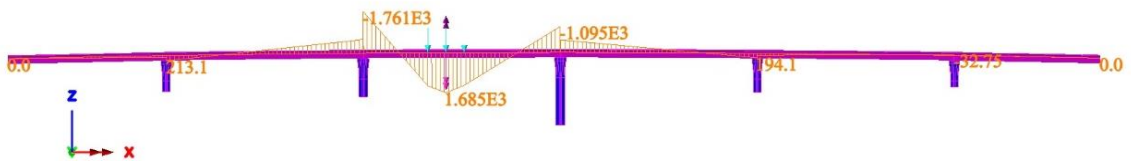


**Figure 2.92** Moment Diagram under HS-20 truck load.

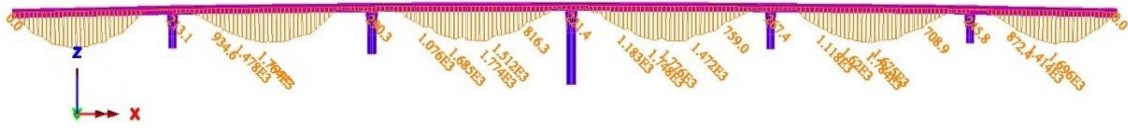


**Figure 2.93** Positive Moment Diagram envelope under HS-20 truck moving load (max positive moment  $1.85 \times 10^3$  kN.m ).

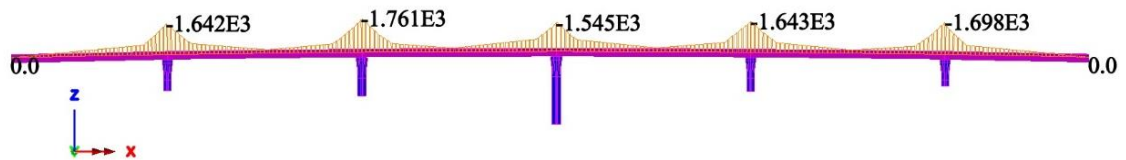


**Figure 2.94** Negative Moment Diagram envelope under HS-20 truck moving load (max negative moment  $-1.76 \times 10^3$  kN.m ).

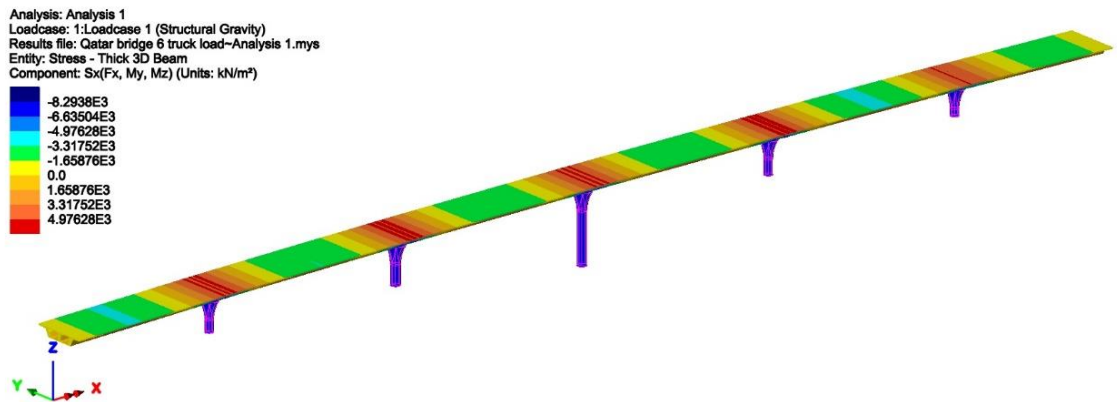


**Figure 2.95** Stress Contour S(x) of bridge deck under gravity load.

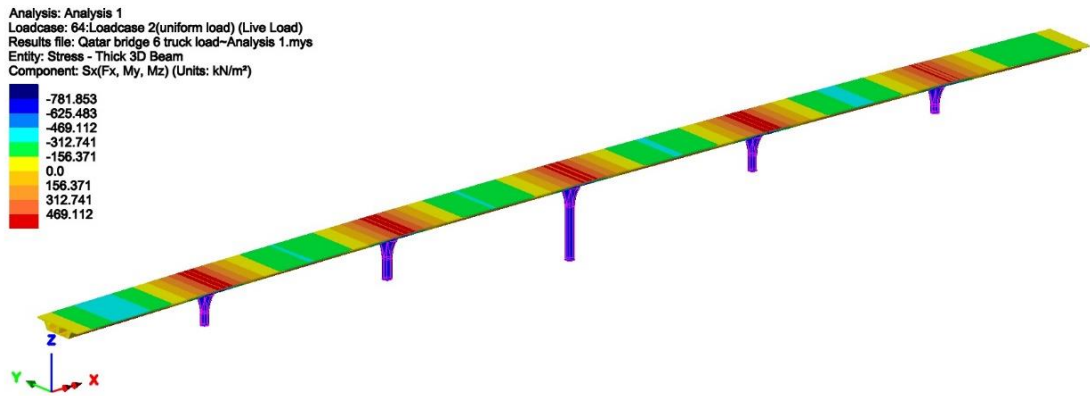


Figure 2.96 Stress Contour S(x) of bridge deck under lane load.

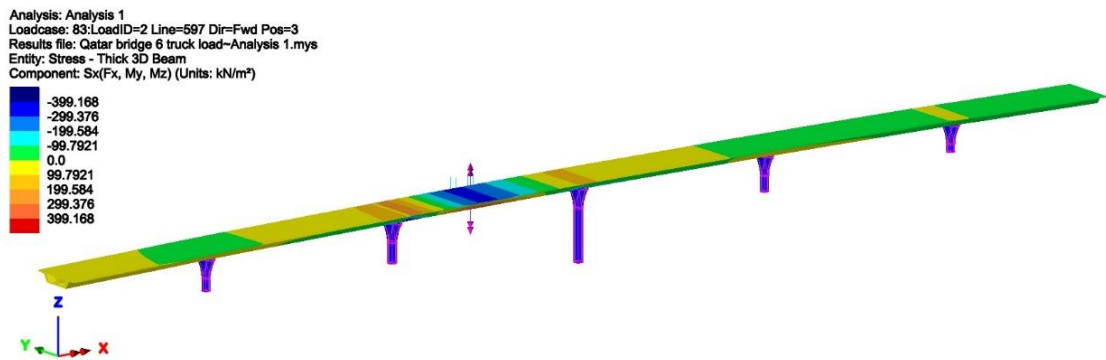


Figure 2.97 Stress Contour S(x) of bridge deck under moving HS-20 truck load.

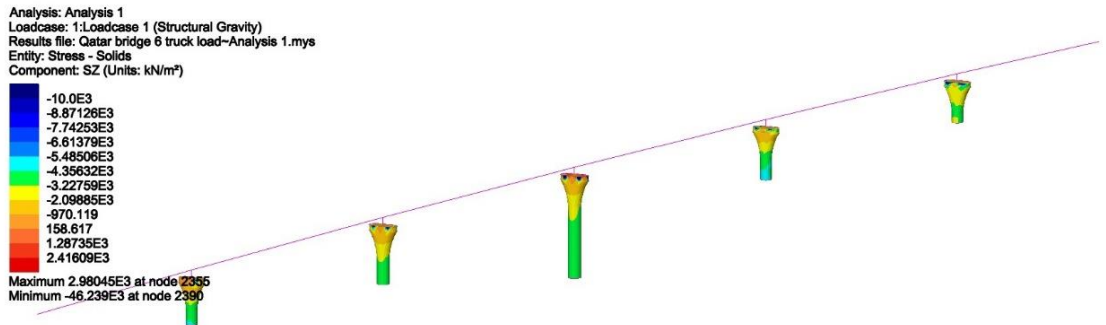
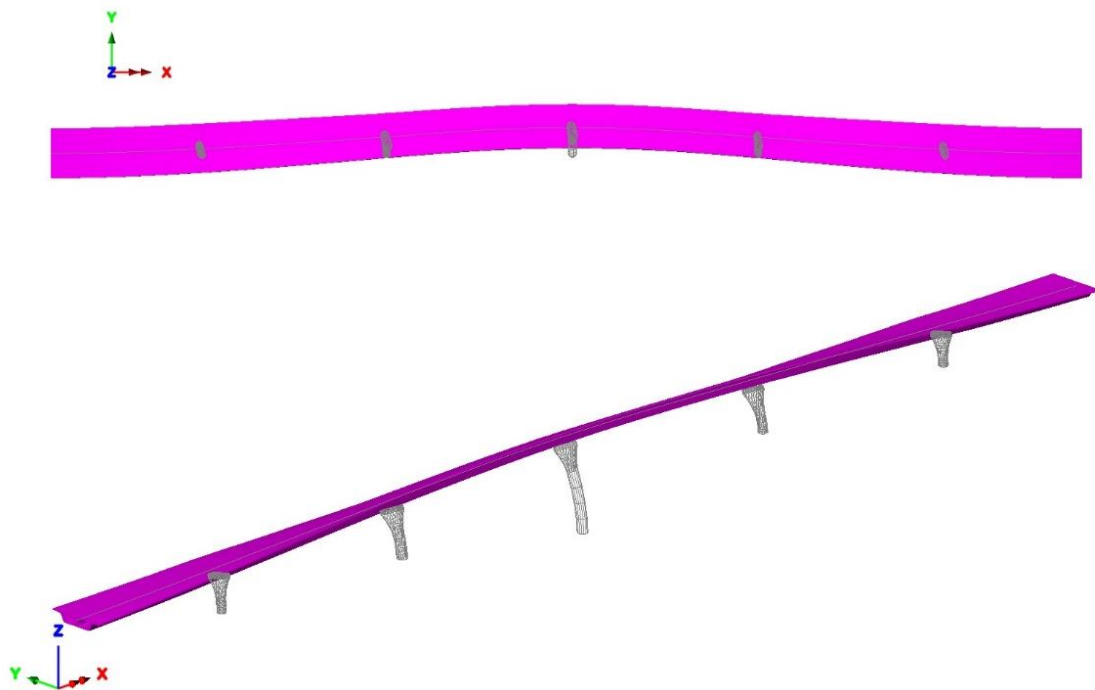


Figure 2.98 Stress Contour S(z) of bridge piers under gravity load.

### 2.5.7 Natural Frequency Analysis Results

The first 10 mode shapes obtained from Eigenvalue Frequency Analysis are presented in Figures 2.99-2.108. The first two vibration mode are transverse and the third mode is the first vertical mode. Eigenvalue results of the first 10 mode shapes for the whole structure are displayed in Table 2.8. Noting that the frequency in Hertz is obtained by dividing the square root of the eigenvalue by  $2\pi$ , and the period of vibration in seconds can be obtained using the reciprocal of frequency ( $1/\text{frequency}$ ). The error norm for a given mode provides a relative measure of the accuracy of the computed modes. A high error norm signifies inaccuracy in either the eigenvalue or the eigenvector, or both and will provoke a warning message in Lusas Bridge software.



**Figure 2.99** The 1<sup>st</sup> mode shape, plan view on top and 3D view at the bottom (frequency: 1.43 Hz).

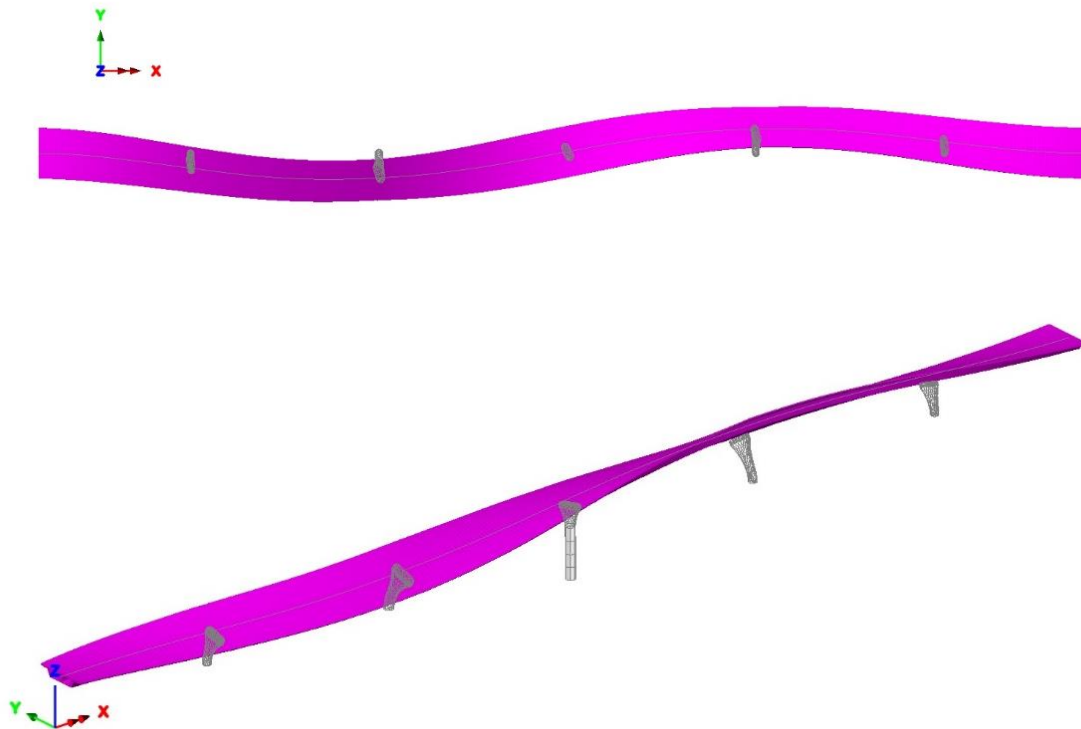


**Figure 2.100** The 2<sup>nd</sup> mode shape, plan view on top and 3D view at the bottom (frequency: 2.38 Hz).

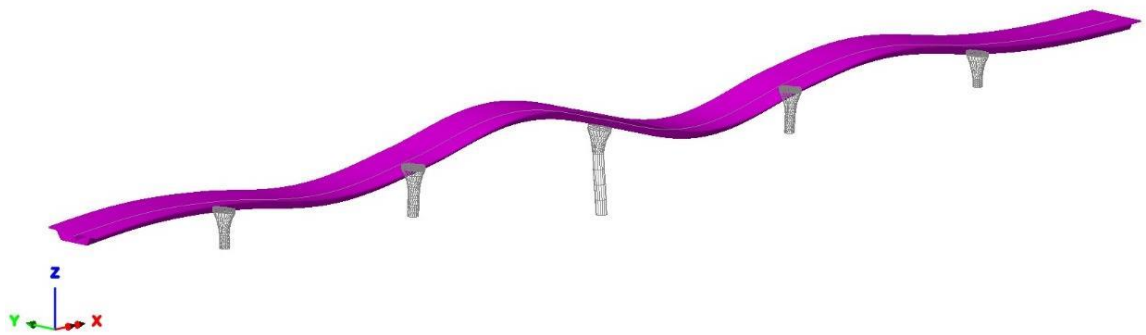


**Figure 2.101** The 3<sup>rd</sup> mode shape (frequency: 2.69 Hz).

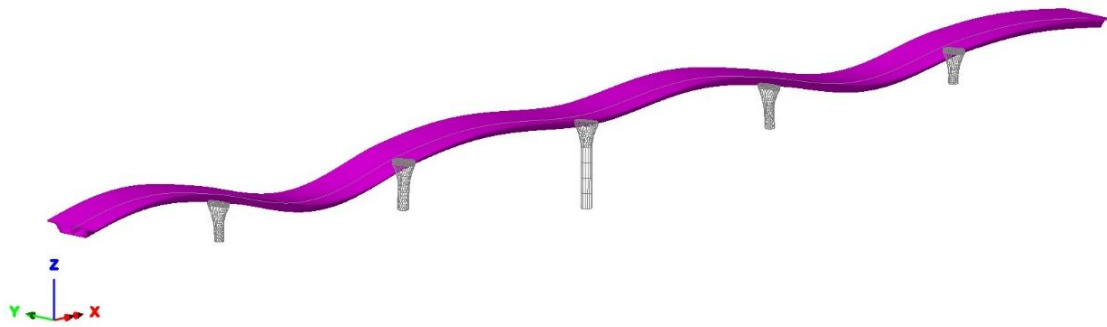


**Figure 2.102** The 4<sup>th</sup> mode shape.

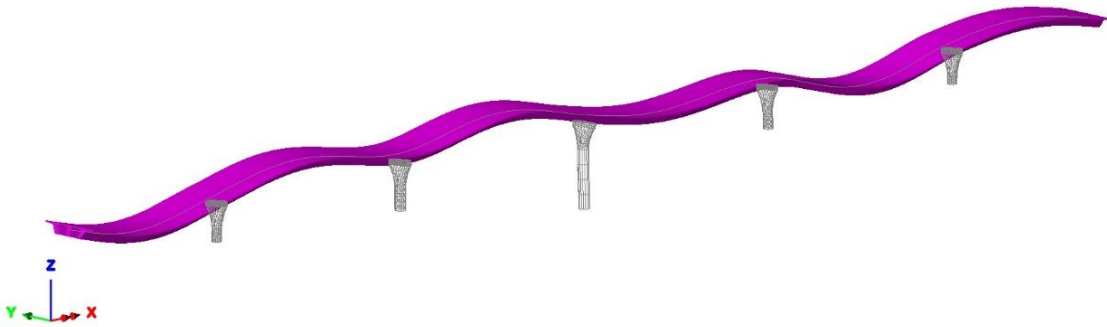


**Figure 2.103** The 5<sup>th</sup> mode shape.

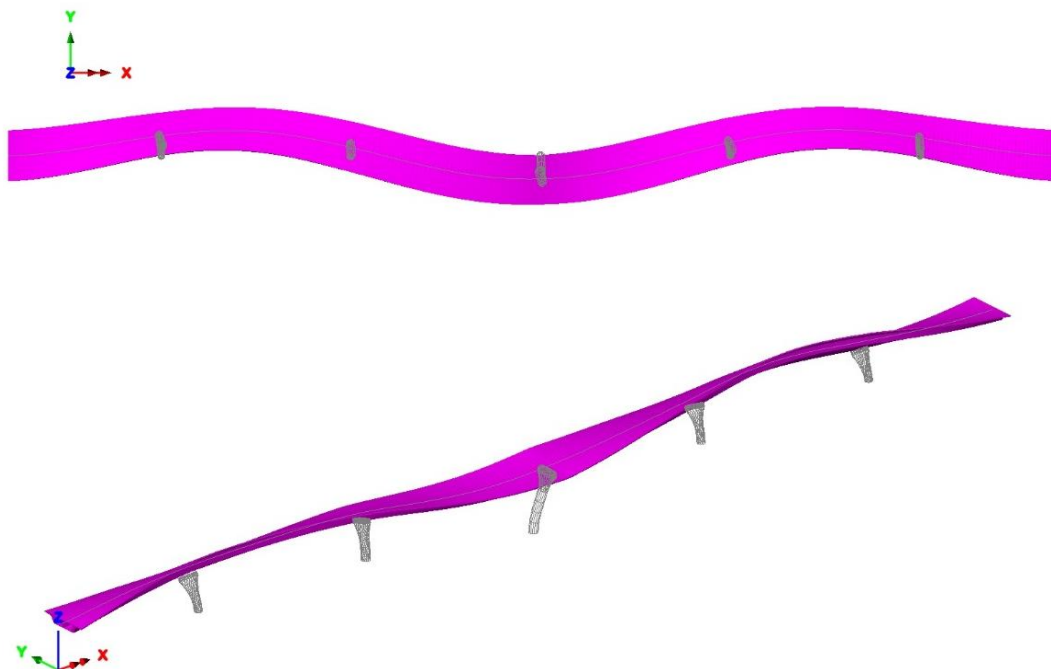


**Figure 2.104** The 6<sup>th</sup> mode shape, plan view on top and 3D view at the bottom.



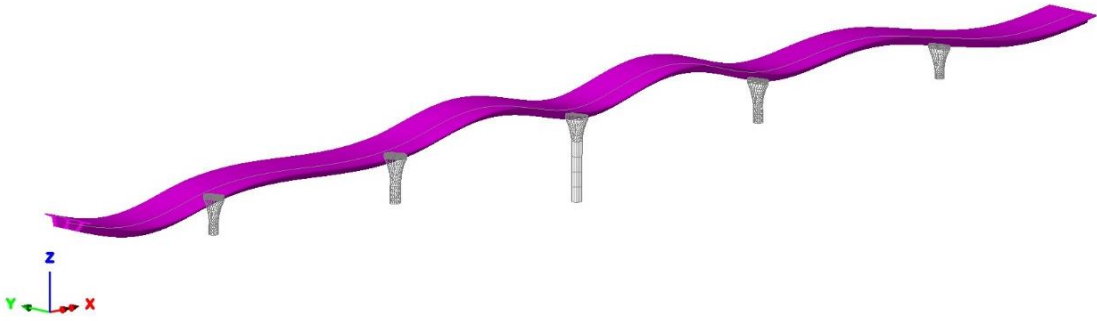


Figure 2.105 The 7<sup>th</sup> mode shape.

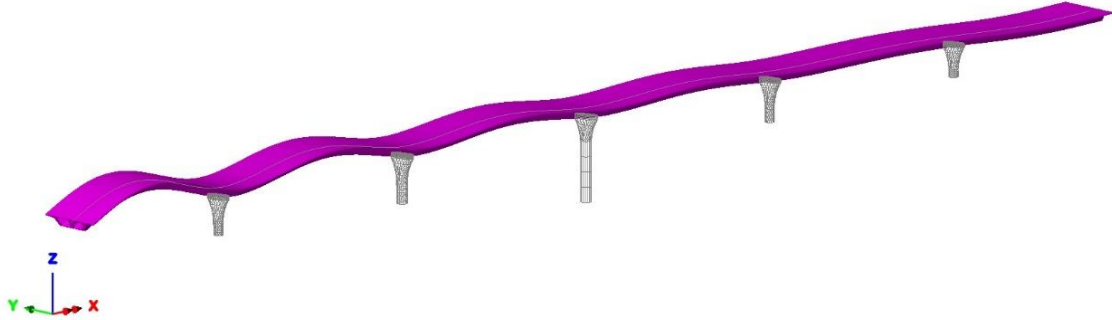
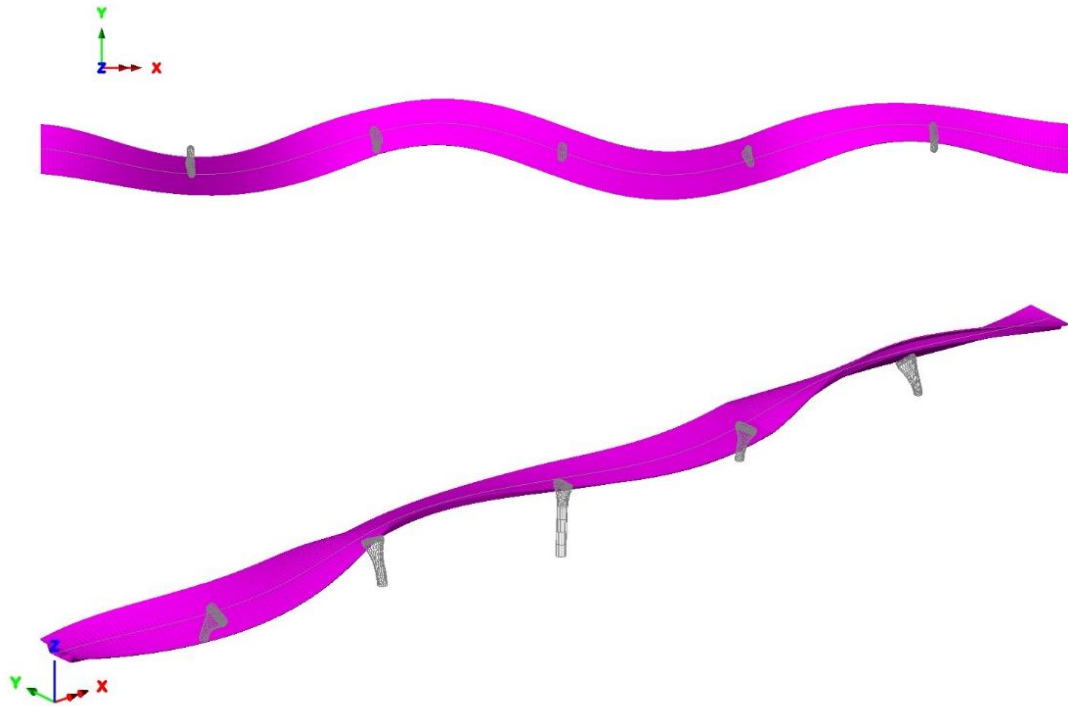


Figure 2.106 The 8<sup>th</sup> mode shape.



Figure 2.107 The 9<sup>th</sup> mode shape.



**Figure 2.108** The 10<sup>th</sup> mode shape, plan view on top and 3D view at the bottom.

**Table 2.8** Modal Frequencies of Concrete Box Section

<b>Mode</b>	<b>Eigenvalue</b>	<b>Frequency (Hz)</b>	<b>Error Norm</b>
<b>1</b>	80.73	1.43	0.249011E-10
<b>2</b>	224.74	2.38	0.321457E-08
<b>3</b>	286.26	2.69	0.107534E-06
<b>4</b>	360.15	3.02	0.734772E-06
<b>5</b>	446.17	3.36	0.662351E-05
<b>6</b>	468.42	3.44	0.711453E-06
<b>7</b>	580.09	3.83	0.385683E-04
<b>8</b>	705.69	4.23	0.349717E-03
<b>9</b>	899.49	4.77	0.306804E-02
<b>10</b>	1083.15	5.24	0.715200E-04

## 2.6 Conclusions

In this chapter, Lusas Bridge plus finite element program was used to simulate the behavior of an experimental frame, 3-span bridge and the in-service 6-Span Precast Segmental Box Girder Bridge. In general, the conclusions and methods would be very similar using other nonlinear Finite Element Analysis programs. Model development for aforementioned structures is demonstrated. Element types used in the models are covered along with the constitutive assumptions and parameters for the various materials in each Section. Besides, Geometry of the models, loading and boundary conditions are illustrated. The mode shapes obtained from eigenvalue frequency analysis are presented. For the 3-span bridge Moving Load analysis has been carried using the IMDPlus facility and Seismic response of the bridge under El Centro earthquake ground motion is presented. Furthermore, Static and Dynamic Finite Element Analysis of 6-Span Precast Segmental Box Girder Bridge has been carried out. Finite Element Analysis results for each model thoroughly demonstrated in each section. The Finite Element Analysis performed in this chapter will be employed in the next chapters. For future studies, the accuracy of FEA results obtained will be validated using lab-scale experimental or Structural Health Monitoring results. Additionally, Finite Element Modal Updating technique can be utilized to obtain calibrated model of each structure.

## **CHAPTER 3**

### **EXPERIMENTAL WORK**

#### **3.1 Introduction**

This chapter is dedicated to a preliminary study in designing and setting up a test-bed for the research on Structural Health Monitoring utilizing Wireless Sensor Networks. To evaluate the performance of the sensors and validate the proposed optimal design and algorithms of used wireless sensor network under actual experimental conditions, a series of tests were carried out on a scaled down frame mounted on the shaking table in the laboratory. The design and setup of the physical model are presented in detail. Three different excitation cases has been investigated to evaluate the performance of the developed wireless sensing system under actual experimental conditions. Furthermore, responses obtained from the WSN system will be compared to the ones resulted from the finite element model.

#### **3.2 Reinforced Concrete Frame**

Reinforced concrete frame used for this lab experiment was designed by Dr. Mohamed Mahgoub and constructed in Qatar University Department of Engineering laboratory. The RC frame is shown in Figure 3.1. The span of the beam is 32.5 cm (12.8 in) and the height of both columns are 24.5 cm (9.6 in). The frame properties are: The modulus of elasticity  $E_c = 31.58\text{MPa}$  (4500 psi), mass per unit volume  $M = 2400\text{ kg/m}^3$  (150 lb/scf), cross-section dimensions  $5 \times 5\text{ cm}$  for an area  $A = 25\text{ cm}^2$ , #2 (6 mm diameter) for Steel rebar, for stirrups diameter of 3 mm and 1 cm concrete cover. Figure 3.2 shows the frame dimensions and the location of the rebar. There were four main flexural steel bars extending

the full length and four bars that bent up to reinforce negative moment regions of the beam. Similar rebars were used for the beam and columns. A special support fixture was used at the ends of both columns to ensure that a close approximation of the idealized boundary condition was achieved. Design calculations and construction procedures for the frame are provided in Appendix A.



**Figure 3.1** The investigated RC frame.

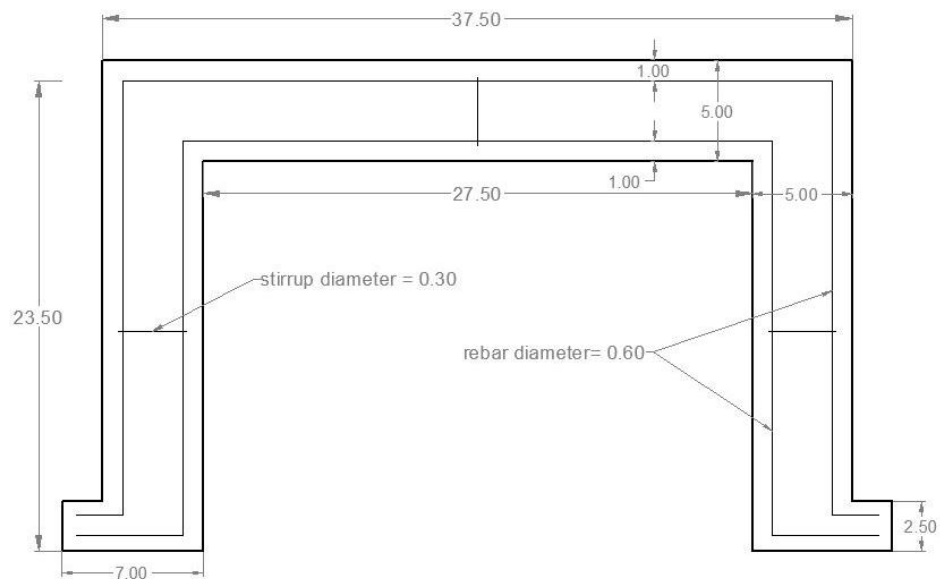


**Figure 3.2** Position of steel reinforcement in RC frame (Dimensions are in cm).

### 3.3 Experiment Setup

All the tests were carried out on a scaled down Reinforce Concrete frame mounted on the shaking table in Qatar University Department of Engineering laboratory (see acknowledgements section). The RC frame was excited by sine excitation using the shaking table at different frequencies and the time history data were measured using the accelerometers with the help of wireless sensing system. Six different cases were run to evaluate the performance of the sensors and wireless networks at frequency of 5 Hz, 7 Hz, 11 Hz, 13 Hz, 15 Hz and 20 Hz. Figure 3.3 presents the input excitations of the shaking table.

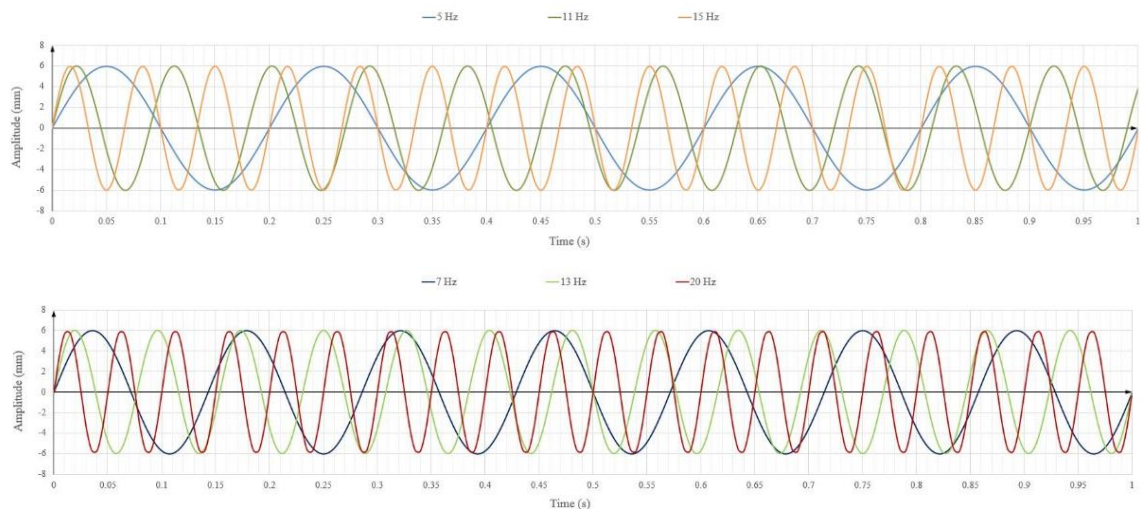


**Figure 3.3** Sine excitation of shaking table.

Figure 3.4 shows the layout of the location of the sensors for measurement of vertical and horizontal in-plane accelerations. Three accelerometers were placed on top of the beam (node ID 3, 2 and 7) and two accelerometer were placed at columns (node ID 4 and 8).



**Figure 3.4** Wireless sensors arrangement mounted on RC frame.

### **3.3.1 Shaking Table**

For the excitation of the reinforced concrete frame, a shaking table was used consisting of a M437A magnetic air cooled shaker and a BT500M slip table with total weight of 4900 kg (10800 lb) and dimensions of 2043L × 1510W × 1166H (see Figure 3.5).



**Figure 3.5** RC frame mounted on the shaking table.

M437A shaker has the capacity of maximum force of 8,800 lbf peak sine force with a dynamic performance ranging from DC to 2,500 Hz and designed for specimen payload up to 500 kg (1102 lbs). Other properties of the shaker has been presented in Table 3.1. The BT500M slip table with the dimensions of 500 mm × 500 mm (19.7 in × 19.7 in) is capable of providing high over-turning moment and cross-axial restraints, since it combines a standard slip table assembly with 3,000 psi hydrostatic bearings to provide high dynamic moment restraint while preserving the damping characteristics of an oil film. Additionally, light weight magnesium has been used for the slip plate (see Table 3.2 for more details). As shown in Figure 3.5, the frame is mounted on the shaking table using fully threaded stainless steel bolts.

**Table 3.1** M437A Shaker Properties

<b>System Performance</b>	<b>American</b>	<b>Metric</b>
Sine Force	8,800 lbf	4,000 kgf
Shock Force (6ms)	17,600 lbf	8,000 kgf
Useful Frequency Range	DC to 2,500 Hz	DC to 2,500 Hz
Continuous Displacement	2.0 in	51 mm
Max Velocity	5.9 ft/s	1.8 m/s
Max Acceleration (sine)	100 g	981 m/s <sup>2</sup>
Max Static Payload	1102 lb	500 kg
Armature Diameter	14.5 in	370 mm
Armature Material	Aluminum (A)	Aluminum (A)
Amplifier Series/Model Number	MPA409	MPA409



**Table 3.2** BT500M Slip Table Properties

<b>System Performance</b>	<b>American</b>	<b>Metric</b>
Slip Plate Working Surface	19.7 x 19.7 in	500 x 500 mm
Slip Plate Material	Magnesium (M)	Magnesium (M)
Slip Plate Thickness	1.57 in	40 mm
Slip Plate Grid plus amature pattern	4 in grid	100 mm grid
Slip Plate Mass	46.2 lb	21 kg
Max Payload	882 lb	400 kg

### 3.3.2 Measurement Sensors

Regarding the wireless based equipment, the Crossbow technology [22] was chosen as it offers economical solutions including low powering boards and measurement platforms with microaccelerometers embedded. The selected Crossbow product (WSN professional kit) uses as gateway a IRIS Mote board (Figure 3.6) in charge of the communication over the network in the radio frequency range of 2.4 to 2.48 GHz. IRIS Mote provides three times radio range and twice the program memory over previous MICA Motes and Outdoor line-of-sight tests have yielded ranges as far as 500 meters between nodes without amplification. Additionally, any IRIS Mote can function as a base station when it is connected to a standard PC interface or gateway board. A base station allows the aggregation of sensor network data onto a PC or other computer platform.



**Figure 3.6** IRIS mote board top and bottom view.

To provide communication, in-system programming and to supply energy to the devices, the system uses an interface board model MIB520 (Figure 3.6) connected to a central computer through a USB bus. USB Bus power eliminates the need for an external power source for this board.



**Figure 3.7** MIB520 USB interface board.

The sensors' platform supplied by Crossbow is composed by a measurement board that works mounted on an IRIS Mote board. In this unit, the IRIS Mote board is not only in charge of the network communication but also in charge of supplying energy to the measurement board (using two AA batteries), as well as acquiring and converting the analog measurements with an ADC resolution of 10 bits. There are several options of measurements boards available in the market, however; the one suitable for dynamic monitoring works is the MTS400 which developed in conjunction with UC Berkeley and Intel Research Labs. This measurement board has embedded four microsensors: biaxial microaccelerometer; light; pressure-temperature; and humidity-temperature. Table 3.3 presents the characteristics of the biaxial microaccelerometer ADXL202 embedded in the MTS400 board. These sensor boards utilize the latest generation of IC-based surface mount sensors which enable these energy-efficient digital devices to provide extended battery-life and performance wherever low maintenance field-deployed sensor nodes are required. The

location of the sensors in the MTS400 board are shown in Figure 3.8. The technical specifications of the referred sensors are found in Appendix B of the present thesis.

**Table 3.3** Characteristics of Microaccelerometer ADXL202

Sensor Type	ADXL202JE
Channels	X, Y
Frequency Response (Hz)	0 - 50
Range (g)	$\pm 2.0$
Sensitivity (mV/g)	$167 \pm 17\%$
Resolution (g rms)	0.002
Size (mm)	5.0 x 5.0 x 2.0
Weight (gram)	1.6
Noise Density ( $\mu\text{g}/\sqrt{\text{Hz}}$ )	500

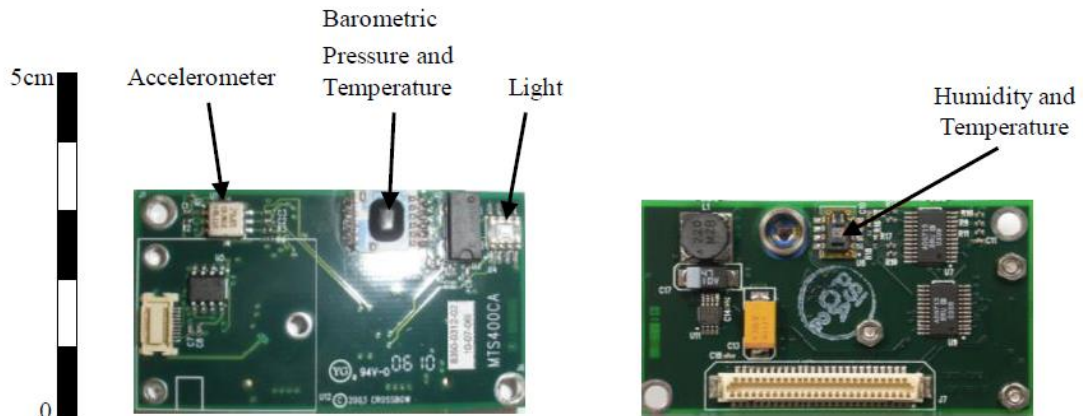


**Figure 3.8** Front and back view of the MTS400 sensors' board.

### 3.4 Experimental Results

For this test, a sampling period of 120 seconds was considered .To show overall data quality of the measured acceleration, a sample time histories of 15 seconds are provided in Figures 3.9-3.11. Under 5 Hz sine excitation, the acceleration from two wireless sensors on top of the beam (node ID 3 and 7) and one sensor mounted on the column (node ID 4) have been compared in Figure 3.9. The acceleration from these sensors at 13 Hz and 20 Hz are provided in Figures 3.10 and 3.11 respectively.

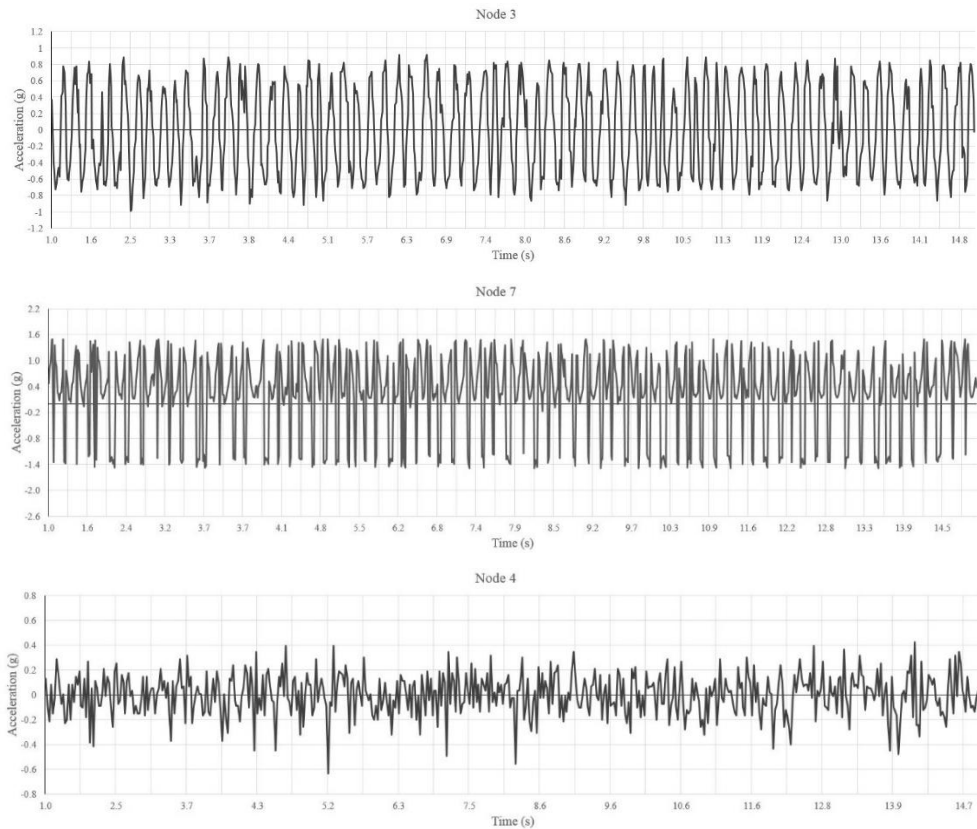


**Figure 3.9** Acceleration data recorded under 5 Hz excitation

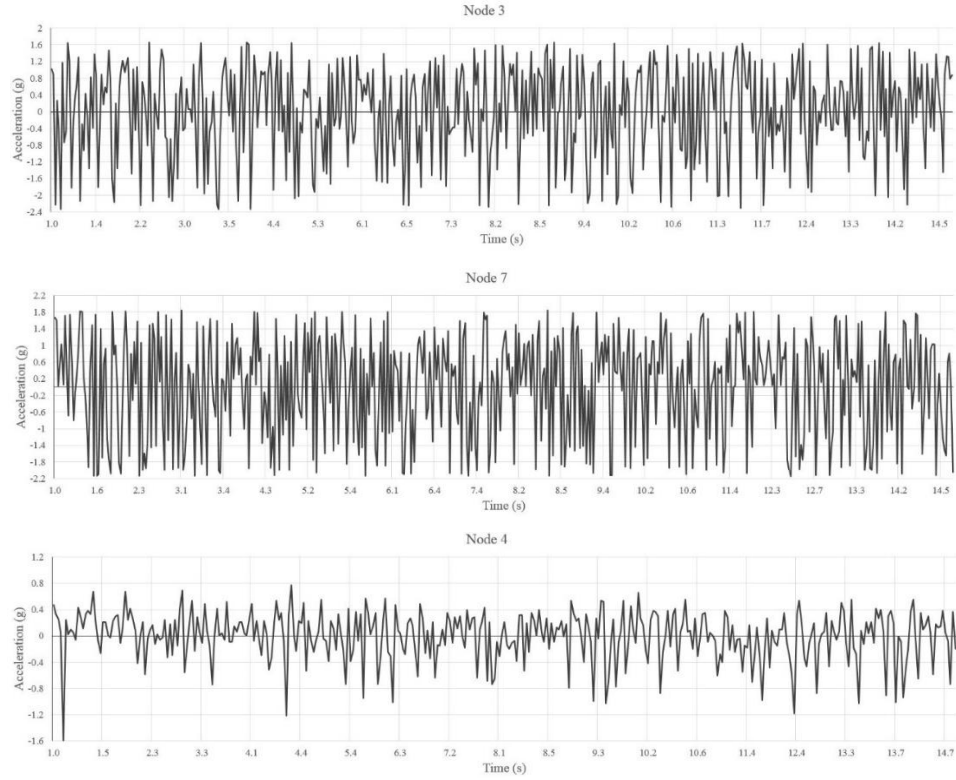


**Figure 3.10** Acceleration data recorded under 13 Hz excitation.

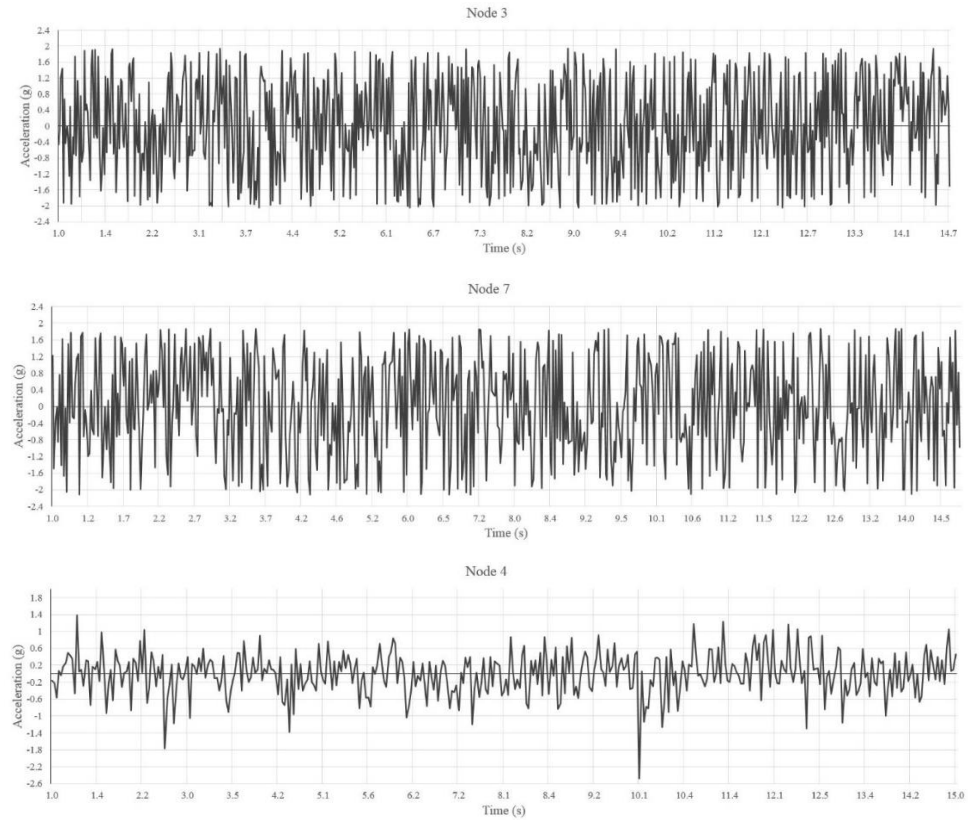


**Figure 3.11** Acceleration data recorded under 20 Hz excitation.

From the experimental data it can be observed that the accelerations measured seem identical to the excitation due to the fact that the frame with the small size being very rigid. Moreover, for all excitation cases the recordings of the three accelerometers are very similar because of the geometric size of the RC frame model.

### **3.5 Conclusions**

This chapter presents a preliminary study in designing and setting up a test-bed for the research on SHM of bridges utilizing Wireless Sensor Networks. The test-bed encompasses the physical model and FE model of a scaled down reinforced concrete frame. The design and setup of the physical model are presented in detail.

The Reinforced Concrete frame was excited by sine excitation using the shaking table at six different frequencies and the time history data were measured using five MEMS accelerometers with the help of wireless sensing system. Note that the problems related to the energy consumption were not considered since the use of these platforms for long term monitoring was outside the scope of these tests. Time histories of the measured accelerations are provided at three different frequency. In conclusion, the plot results show that the developed wireless sensing system is capable of measuring the dynamic response of the RC frame structure with reliable precision level.

In the future studies, dynamic characterization of the RC frame will be carried out to determine the modal properties of the frame such as: natural frequencies, modal shapes and damping ratios. Subsequently, the natural frequencies and mode shapes obtained from the initial FE model in Section 2.3 will be compared with those measured from the vibration tests. Finite Element Model updating is needed to improve the FE model, Hence, these

measured dynamic characteristics of the physical model will be used for updating the FE model of the RC frame. Eventually, damage cases will be applied in the frame in the form of saw cuts perpendicular to the longitudinal axis of the beam. Modal test results obtained from the damaged frame will be compared to the updated FE model for the subsequent studies of damage detection.

**CHAPTER 4**  
**IMPLEMENTATION OF HEALTH MONITORING SYSTEM ON**  
**AN IN-SERVICE HIGHWAY BRIDGE**

**4.1 Introduction**

Major applications of SHM have been implemented in the oil industry, large dams and bridges and have acquired a great deal of research and practical efforts. Residential and commercial structures have received relatively little attention in comparison [10]. Bridge monitoring can be dated back to the construction of the Golden Gate and Bay Bridges in San Francisco in the 1930s in USA, in which the dynamic behavior of the bridges was studied. The collapse of the Tacoma Narrows Bridge in Washington State, USA in 1940 led to the inspection and modification of other suspension bridges, including strengthening the Golden Gate Bridge. The widespread introduction of systematic bridge inspection programs was directly attributed to the catastrophic bridge collapse at Point Pleasant, West Virginia, USA, in 1967 [10]. At present, bridges are generally inspected every two years, largely using visual inspection techniques with the aid of some NDE methods such as acoustic or ultrasonic methods. There is the possibility that damage could not be detected between inspection intervals.

In the last three decades, many attempts have been made to detect structural damage using vibration data, in both time domain and frequency domain [10, 11]. The vibration-based methods have achieved some success in mechanical and aerospace engineering, whereas their successful applications to large-scale civil structures are very limited [23] due to the uniqueness of civil structures, significant uncertainties of structures and complicated environmental factors.



Since the 1990s, long-term monitoring systems have been implemented in major bridges in China, Japan, America, and Europe. In Hong Kong and mainland China alone, more than 40 long-span bridges had been equipped with long-term monitoring systems by [24]. Table 4.1 lists major bridges in the United States instrumented with real-time monitoring systems [25, 26].

**Table 4.1** Major Bridges Equipped with Health Monitoring Systems.

Bridge name	Bridge Type[1]	Location	Main span (m)	Sensors installed [2]
Golden Gate Bridge	Susp	San Francisco, CA	1280	(1) (4) (16)
Sunshine Skyway Bridge	Cable	Tampa Bay, FL	366	(2) (3) (5) (7) (9)
Bayview Bridge	Cable	Quincy, IL	274	(9) (18)
Commodore Barry Bridge	Truss	Logan Township, NJ	548	(1) (2) (3) (4) (5) (8) (12) (19) (21) (22)
Ironton-Russell Bridge	Truss	Ironton, OH	241	(2) (3)
New Benicia Martinez Bridge	Box	CA	201	(2) (3) (4) (9) (12) (14)
Saint Anthony Falls I-35W Bridge	Box	Minneapolis, MN	154	(2) (3) (4) (9) (11) (24)
North Halawa Valley Bridge	Box	Halawa, HI	110	(2) (3) (5) (12)

Source: W.S. Winston Ho and Norman N. Li, "Membrane Processes," Perry's Chemical Engineers' Handbook, ed. Robert H. Perry and Don W. Green, 6<sup>th</sup> ed. (New York: McGraw-Hill, 1984) 17-20

Note [1]: Susp – Suspension bridge; Cable – Cable-stayed bridge; Arch – Arch bridge;

Truss – Steel truss bridge; Box – Box Girder Bridge; Rigid – Continuous rigid-frame bridge

Note [2]: (1) – anemometer; (2) – temperature sensor; (3) – strain gauge; (4) – accelerometer;

(5) – displacement transducer; (6) – velocimeter; (7) – global positioning system;

(8) – weigh-in-motion sensor; (9) – corrosion sensor; (10) – elasto-magnetic sensor;

(11) – optic fibre sensor; (12) – tiltmeter; (13) – level sensing station; (14) – dynamometer;

(15) – total station; (16) – seismometer; (17) – fatigue meter; (18) – cable tension force;

(19) – joint meter; (20) – laser displacement sensor; (21) – meteorological station;

(22) – video camera; (23) – jacking pressure sensor; (24) – potentiometer;

Several recent trends in SHM practice for bridges are worth mentioning:

- The recent long-term health monitoring systems emphasize multipurpose monitoring of the bridge integrity, durability, and reliability. For instance, the monitoring system for the Stonecutters Bridge includes sensors measuring environment, such as corrosion sensors, rainfall gauges, barometers, hygrometers, and pluviometers to facilitate bridge safety/reliability assessment [27].
- For some recent bridges such as the Shenzhen Western Corridor and the Stonecutters Bridge, the design of a monitoring system is required as part of the bridge design. Integration of bridge design and monitoring system design ensures that design engineers' important concerns are reflected in the monitoring system while civil provisions for implementing a monitoring system are considered in the bridge design.
- The implementation of long-term monitoring systems on new bridges, such as the Stonecutters Bridge and the Sutong Bridge, is achieved in accordance with the construction progress. In this way some specific types of sensors, such as corrosion sensors, strain gauges, and fiber optic sensors, can be embedded into the bridge during certain bridge erection stages. Furthermore, the construction monitoring results provide initial values of parameters. This is especially important for the strain gauges such that the absolute strain rather than relative strain can be obtained [28]. Consequently the health condition of the structural components and the impact of extreme events (typhoons, earthquakes, etc.) on the structural performance can be evaluated realistically. Additionally, the construction monitoring can provide a complete record of the bridge as the in-construction state may be different from the design state. Integration of the construction monitoring ensures that the later long-term monitoring will be more accurate and effective.

## **4.2 Structural Health Monitoring Systems**

A Structural Health Monitoring system generally consists of sensory system, data acquisition and transmission system, data processing and control system, data management system, and structural evaluation system. The first two are embedded on the structures, while the other three are usually located in the control office.

The sensory system is composed of various types of sensors that are distributed along the bridge to capture different signals of interest. The data acquisition and transmission system is responsible for collecting signals from the sensors and transmitting the signals to the central database server. The data processing and control system is developed to control the data acquisition and transmission, process and store the data, and display it. The data management system consists of the database system for temporal and spatial data management. In accordance with monitoring objectives, the structural evaluation system may have different applications. It may include an online structural condition evaluation system and/or an offline structural health and safety assessment system. The online system is mainly to compare the measurement data with the design values, analysis results, and pre-determined thresholds and patterns to provide an evaluation on the structural condition. The offline includes varieties of model-based and data-driven algorithms, for example, loading identification, modal identification and model updating, bridge rating system, and damage diagnosis and prediction.

Design of SHM systems requires comprehensive understanding of the monitoring needs, characteristics of the structure, environment condition, hardware performance, and economic considerations. First of all, the monitoring items and the corresponding information should be identified, which may include [29]:

- The parameters to be monitored, such as temperature, wind, displacement, and corrosion;
- The nominal value and expected ranges of the parameters;
- The spatial and temporal properties of the parameters, for example, variation speed of the measurands, location of the measurands;

- The accuracy requirement;
- The environment condition of the monitoring;
- The duration of the monitoring.

After the monitoring parameters are identified, the number of sensors should be determined according to the size and complexity of the structure and the monitoring objectives. Then types of sensors are carefully selected such that their performance can meet the requirement of the monitoring. Important sensor performance characteristics include measurement range, sampling rate, sensitivity, resolution, linearity, stability, accuracy, repeatability, frequency response and durability. Moreover, sensors must be compatible with the monitoring environment, such as temperature range, humidity range, size, packaging, isolation, and thermal effect. The data acquisition units (DAUs) should be compatible with the sensors as well. Sampling rate, resolution, accuracy, and working environment should be taken into account for selection of hardware.

Besides, the budget of the project is another important factor in SMH system design, such as availability of hardware, installation and protection of the hardware. Special protection of sensors and wires is worth the effort. Maintenance is also a factor to be considered during the design stage. Important sensors and DAUs should be accessible for check and repair after installation.

### **4.3 Sensors and Sensing Technology**

In bridge monitoring system, the sensors are mainly employed for monitoring three types of parameters: (i) loading sources such as wind, seismic, and traffic loading; (ii) structural

responses such as strain, displacement, and acceleration; and (iii) environmental effects including temperature, humidity, rain, and corrosion. This section introduces the commonly used sensors, categorized by the monitoring parameters.

#### **4.3.1 Wind Measurement Sensors**

The traditional sensors widely used for wind monitoring of a bridge include anemometers for measuring wind velocity. Occasionally, pressure transducers are installed to measure wind pressures and pressure distribution over a particular part of the bridge envelope. Propeller and ultrasonic anemometers are the most commonly used instruments for measuring wind velocity and direction on site. The propeller anemometer directly records wind speed and direction. It is convenient and relatively reliable and sustainable in harsh environments but it is not sensitive enough to capture the nature of turbulent winds at higher frequencies. The ultrasonic anemometer measures wind velocity through its two or three orthogonal components. The ultrasonic anemometer is quite sensitive but it is not sustainable in harsh environments. For bridge with a long span, the anemometers are often installed at a few bridge deck sections on both sides. Wind pressure transducers sense differential pressure and convert this pressure difference to a proportional electrical output for either unidirectional or bidirectional pressure ranges.

#### **4.3.2 Seismic Sensors**

Seismometers are instruments that measure motions of the ground, including those of seismic waves generated by earthquakes, nuclear explosions, and other sources. For short-period seismometers, the inertial force produced by a seismic ground motion deflects the mass from its equilibrium position, and the displacement or velocity of the mass is then

converted into an electric signal as the output proportional to the seismic ground motion. Long-period or broadband seismometers are built according to the force-balanced principle, in which the inertial force is compensated with an electrically generated force so that the mass moves as little as possible. The feedback force is generated with an electromagnetic force transducer and it is proportional to the seismic ground acceleration. A strong-motion seismometer usually measures acceleration, which is also built on the force balanced principle and can be integrated to obtain ground velocities and displacements.

#### **4.3.3 Weigh-in-motion Stations**

Weigh-in-motion (WIM) devices can measure the axle weight of the passing vehicles and thus the sum of the weight of the vehicles, velocity of the vehicles, and distance between the axles. These data can be used to evaluate the traffic load on bridges. Current WIM systems are capable of measuring weight at normal traffic speeds and do not require the vehicle to stop, making them much more efficient. A dynamic WIM station mainly consists of a metal housing with lightning protection, bending plate sensors and processing board, induction loop detection and loop processor board, central processing unit, and power supply.

#### **4.3.4 Thermometers**

Temperature, including structural temperature and ambient air temperature, is frequently measured in many monitoring systems. Changes in temperature significantly influence the overall deflection and deformation of bridges. Restraint of movement can induce stresses within a bridge. Additionally, Excessive thermal stresses can damage bridges. It is noted

the temperature is usually non-uniformly distributed over the entire structure and is different from the ambient temperature, due to heat transfer. The most often used temperature sensors include thermocouples, thermistors, and resistance temperature detectors.

#### **4.3.5 Strain Gauges**

Foil strain gauges, fiber optic strain gauges, and vibrating wire strain gauges are commonly used sensors measuring strain in civil structures. Figure 4.1 represents a brief comparison between foil strain gauges (also known as electrical resistance strain gauges) and vibrating wire strain gauges. Fiber optic strain gauges will be described later.

Foil strain gauges are the most common type of strain gauge consisting of a thin insulating backing which supports a fine metallic foil. As the object is deformed, the foil is stretched or shortened causing the change in its electrical resistance in proportion to the amount of strain, which is usually measured using a Wheatstone bridge. The physical size of most foil strain gauges is about a few millimeters to centimeters in length. Its full measurement range is about a few milli-strain. The foil strain gauges are economical and can measure dynamic strains.

The vibrating wire strain gauge consists of a thin steel wire held in tension between two end anchorages. The wire vibrates due to an excitation with a short pulse and the resonant frequency is measured. When the distance between the anchorages changes, the tension of the wire changes, so does the natural frequency. The change in the vibration frequency of the wire is transferred into the change in strain. A main drawback of vibrating wire gauges is that they can measure the static strain only as it takes seconds to obtain the frequency of the vibrating wire.

Sensor	Function	Advantages	Disadvantages
Electrical Resistance Strain Gages	Short Term Monitoring	Operate over a wide range of temperatures	Data read out equipment is expensive
		Inexpensive	Tedious installation, time consuming to install and to connect to data acquisition system
		Suitable for dynamic loads	Affected by electromagnetic interference
		Available in a wide variety of gage lengths	Lead length limitation
		Provides an electrical signal that can be measured with a wide variety of circuits	
Vibrating Wire Gages	Long Term Monitoring	Long term reliability	May require long lengths of wire
		Multiplexing ability	Cannot monitor live loads
		Easy installation	
		Low cost	
		Immune to electromagnetic interference	
		Rugged housing resistant to impact and corrosion	
		Measures temperature as well as strain	
Fiber Optic Sensors	Long Term Monitoring & Short Term Monitoring	Light weight	The fiber wire should be handled carefully and gently
		Small size	Expensive hardware and software
		Multiplexing ability	Long term behavior still under investigation
		Immune to electromagnetic interference	Expensive installation
		Environmental ruggedness	
		Extremely accurate	
Wireless System	Short Term Monitoring	No cables are required for data transfer	Restricted battery life
		Low cost of deployment	Still under investigation
		Each mote works independently	

**Figure 4.1** Advantages and Disadvantages of strain gauges.

Source: O. Y. Abudayyeh, J. Barbera, I. Abdel-Qader, H. Cai, and E. Almaita, "Towards sensor-based health monitoring systems for bridge decks: A full-depth precast deck panels case study," *Advances in Civil Engineering*, vol. 2010, 2011.



#### **4.3.6 Displacement Measurement Sensors**

Displacement of bridge structures serves as an effective indicator of its structural performance condition. Large displacements or deformations may create hazardous conditions for traffic actually on the bridge, and excessive displacements may affect the bridge's structural integrity. Displacement monitoring is thus needed. Equipment measuring the displacement includes linear variable differential transformer, level sensing station and Global Positioning System (GPS).

The linear variable differential transformer (LVDT) is a commonly used electromechanical facility for measuring relative displacements based on the principle of mutual inductance. It consists of a hollow metallic tube and a separate movable ferromagnetic core. The coils produce an electrical signal that is in proportion to the position of the moving core. LVDTs are available in a wide range of linear stroke, ranging from micro-meters to 0.5 meter. The measurement of vertical displacement by the level sensors is in principle based on the pressure difference. The conventional level sensing system can detect the elevation difference of about 0.5 mm.

The Global Positioning System (GPS) consists of three parts: the space segment, the control segment, and the user segment. The space segment is composed of 32 satellites in six orbital planes. The spacing of satellites in orbits is arranged so that at least six satellites are within line of sight from any location on the Earth's surface at all times [30]. The control segment is composed of a master control station, an alternate master control station, and shared ground antennas and monitor stations. The user segment is composed of millions of civil, commercial, and scientific users of the standard positioning service. Basically, a GPS receiver receives the signals sent by the GPS satellites high above the

Earth, determines the transit time of each message, computes the distances to each satellite, and calculates the position of the receiver. Nevertheless, this accuracy is in the order of a meter and cannot be used for displacement monitoring of bridges. In the practical survey, the Real Time Kinematic (RTK) technique is used where a reference station provides the real-time corrections. A RTK system usually consists of a base station receiver and a number of mobile units. The base station re-broadcasts the phase of the carrier that it measures, and the mobile units compare their own phase measurements with the ones received from the base station. This system can achieve a nominal accuracy of  $1 \text{ cm} \pm 2$  parts-per-million (ppm) horizontally and vertically. Atmospheric conditions affect the accuracy of GPS measurements.

#### **4.3.7 Accelerometers**

Although vibration can be measured in terms of velocity and dynamic displacement as well, acceleration can be measured more accurately. Accelerometers are widely used to measure acceleration of structures induced by force or ambient excitations. The acceleration responses of a bridge are closely related to the serviceability and functionality of the bridge. Additionally, a vibration testing can be employed to obtain the natural frequencies, damping ratios, and mode shapes of the global structure, which are directly associated with the mass, stiffness, and damping characteristics.

Basically an accelerometer is a mass-spring-damper system that produces electrical signals in proportion to the acceleration of the base where the sensor is mounted. The following parameters should be considered in selection of accelerometers: usable frequency response, sensitivity, dynamic range, and thermal transient sensitivity. There are

four main types of accelerometers available: piezoelectric type, piezoresistive type, capacitive type, and servo force balance type.

#### **4.3.8 Weather Stations**

In some applications, it is desirable to measure the environmental conditions such as ambient temperature, humidity, rainfall, air pressure, and solar irradiation. A typical weather station usually integrates a few types of sensors and can measure the above-mentioned parameters besides the wind speed and direction. Solar irradiation intensity, air temperature, and wind are important parameters for deriving the temperature distribution of structures. With temperature distribution, the thermal effect on the structural responses can be evaluated quantitatively.

#### **4.3.9 Fiber Optic Sensors**

Optical fibers can be used as sensors to measure strain, temperature, pressure, and other quantities. The sensors modify a fiber so that the quantity to be measured modulates the intensity, phase, polarization, wavelength of light in the fiber. Accordingly the fiber optic sensors can be classified into four categories as: intensity modulated sensors, interferometric sensors, polarimetric sensors, and spectrometric sensors [31].

A significant advantage of the fiber optic sensors is multiplexing, that is, several fiber optic sensors can be written at the same optical fiber and interrogated at the same time via one channel. In addition, fiber optic sensors are very small in size and immune to electromagnetic interferences. They are also suitable for both static and dynamics measurements with a frequency from hundreds to thousands Hertz. The major drawback of fiber optic sensors is the high cost of both sensors and the acquisition unit (or readout

unit). In addition, the fibers are rather fragile and should be handled very carefully in the field installation. Figure 4.2 represents a brief comparison between fiber optic and vibrating wire sensors.

Parameters	Embeddable Fiber Optic Sensor	Vibrating Wire Strain Gage
Gage length	1 to 500 mm	50 to 300 mm
Resolution	0.01% full scale	1 Microstrain
Measurement range	±2000 to ±10000 Microstrain	±2000 to ±3000 Microstrain
Remote operations possibility	Yes	Yes
Working principle	Measuring the change in optical characteristics such as intensity, wave length , phase	Measuring the frequency of a taut wire
Availability for embedment and surface mounting	Yes	Yes
Material of sensor	High strength silica	High strength steel piano wire
Structural response capabilities	Static and dynamic loads	Just static loads
Temperature range	- 20 to 60 °C	-20 to 80°C
Immunity to electromagnetic interface	Yes	Yes
Ability to multiplexing	Yes for long and short term monitoring	Yes for long term monitoring

**Figure 4.2** Fiber optic versus vibrating wire Sensors.

Source: O. Y. Abudayyeh, J. Barbera, I. Abdel-Qader, H. Cai, and E. Almaita, "Towards sensor-based health monitoring systems for bridge decks: A full-depth precast deck panels case study," *Advances in Civil Engineering*, vol. 2010, 2011.

In bridge monitoring, Fiber Bragg grating (FBG) sensors are commonly used for strain measurement [32, 33]. The strain variation causes the shift in the central Bragg wavelength. Consequently, FBG strain sensors monitor changes in the wavelength of the light. Counting the spectral space between the sensors, one optical fiber can accommodate six to ten FBG sensors. Other applications of fiber optic sensors include monitoring fatigue crack [34], wear of bearings [35], corrosion [36], displacement [37], temperature [38], and acceleration [39].

#### **4.4 Wireless Sensors and Wireless Monitoring**

Advances in micro-electro-mechanical systems (MEMS) technology, wireless communications, and digital electronics have enabled the rapid development of the wireless sensor technology since the late twentieth century. The wireless sensor is actually neither one kind of pure sensing technology nor just a new transmission method, but a new system that can carry out many tasks including SHM. A wireless sensor network can comprise all of the components in a wire-based SHM system described previously, whereas it has its unique characteristics as compared with the wire-based SHM systems.

Development of wireless sensors is due to the fact that a robust system may require a dense network of sensors throughout the system. Traditional sensing systems usually attempt to develop more accurate sensors of limited quantity at optimized locations. A bio-system, however, usually comprises a huge number of distributed sensors each with limited functions. This philosophy inspires researchers to develop a network of low-cost, small size, large quantity sensors. In addition, the traditional sensing systems are usually wire-based which have high installation costs. Maintenance of such a monitoring system at a reliable operating level under the adverse environment for a long period of time is very difficult. Experience in monitoring civil structures shows that communication wires are more vulnerable to the environment than sensors themselves [40]. The wireless transmission provides a more flexible communication manner and sensors can be deployed and scalable easily.

As a result, Wireless sensor networks have been proposed extensively over the past several years as a means of alleviating instrumentation costs associated with structural health monitoring of civil infrastructure. However, low data throughput, unacceptable

packet yield rates, and limited system resources have generally plagued many deployments by limiting the number of sensors and their sampling rate. The sensor networks present challenges in three broad areas: energy consumption, network configuration and interaction with the physical world. Therefore, the development of sensor networks requires technologies from three different research areas: sensing, communication, and computing (including hardware, software, and algorithms). Structural health monitoring sensors need to be low-cost, low-power, self-healing, self-organized, and compact.

Researchers at the University of California at Berkeley have developed the open platform, well known as Berkeley Mote whose ultimate goal is to create a fully autonomous system within a cubic millimeter volume [41]. Such a system may comprise hundreds or thousands of sensor nodes each costing as little as about one US dollar. Berkeley Mote was the first open hardware/software research platform, which allows users to customize hardware/software for a particular application. The third generation of Mote, the Mica, was released in 2001. Subsequent improvements to the Mica platform resulted in Mica2, Mica2Dot, and MicaZ. Another commonly used wireless sensor unit is the Intel Mote platform Imote [42] and Imote 2 [43].

Berkeley Mote, Intel Mote, and quite a few others have been used for general purposes in military, environment, health, home, and other commercial areas [44, 45]. These systems have been customized for SHM applications [46-48]. A wireless monitoring was implemented in the Jindo Bridge, Korea in June 2009, in which 110 wireless nodes were used. In the structural discipline, researchers from Stanford University have developed their own wireless sensor unit for SHM [49, 50].

#### **4.4.1 Basic Architectures and Features of Wireless Sensors**

A wireless sensor node usually consists of four basic components: a sensing unit, a processing unit, a transceiver unit, and a power unit [44]. The components are carefully selected to meet the specified functions and keep a total low cost.

The processing unit is a micro-processor (or micro-controller), which controls the sensing, data processing, computation, and communication with other sensor nodes or the central station. The on-board processor makes the wireless sensor node intelligent, which differs from a traditional sensor. The microprocessor has a small storage that stores internal programs and processed data.

The sensing unit is usually composed of a few sensors and the Analog to Digital Converter (ADC). The analogue signals collected by the sensors are converted to digital signals by the ADC, and then sent to the processing unit. It is noted that the ADC in most general wireless sensor nodes is of only 8 or 10 bits. This is insufficient for vibration monitoring. In the customized Imote 2 [48], a 16-bits ADC is embedded. The wireless sensor unit developed in Stanford University [49] has a 16-bits ADC as well.

A transceiver unit connects the node to the network. The transmission distance of most wireless nodes is about 50 m to 500 m in outdoor environment.

Hence for large civil structures, this transmission range requires the sensor nodes communicate with the peers and send the data to the base station over the network. The wireless network has three kinds [51]: star, peer-to-peer, and multi-tier, as shown in Figure 4.3. In the figure, the sensor nodes include generic nodes and gateway nodes. A gateway node, like the substation in the wired systems, gathers data from the adjacent generic nodes

and transmits them to the base station. Most of the smart sensors to date adopt radio frequency for the wireless communication.

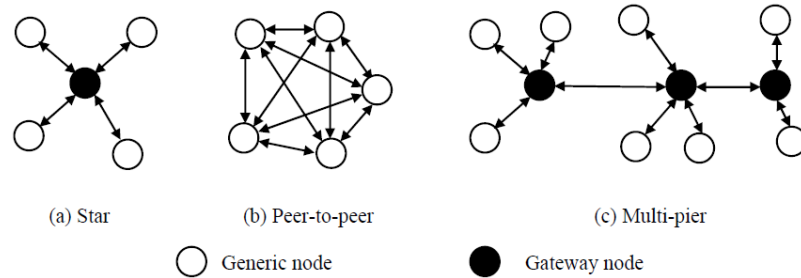


**Figure 4.3** Wireless network topology.

The power unit is an important component in wireless sensor node. Currently most of available smart sensors rely on the battery power supply, which has finite capacity and finite life. There have been several attempts to harvest energy at sensor nodes locally, for example, solar cell, wind turbine, mechanical vibration, fuel cells, and mobile supplier. Solar cell is the current mature technique and was used in wireless monitoring of the Jindo Bridge [52]. In wireless sensor nodes, communication consumes much more power than other operations including sensing and processing. Therefore, collected raw data are processed within the sensing unit to reduce the amount of the raw data transmitted wirelessly over the network. This also takes advantage of the computational characteristics of the processor board. Accordingly this distributed computation and monitoring make the wireless monitoring different from the monitoring using the traditional wired system.

To facilitate this distributed monitoring, the micro-processor has two types of software: one is the operating system and the other is the engineering algorithms. The operating system controls the nodes and provides device drivers. One popular operating system is TinyOS (<http://www.tinyos.net>), an open-source operating system designed by



the University of California at Berkeley. Both Berkeley Mote and Intel Mote run the TinyOS operating system.

Currently algorithms for distributed monitoring are relatively scarce and simple, mainly in modal analysis. The complicated monitoring algorithms used in the centralized monitoring usually need a large amount of memory, heavy computation, and data from multiple sensors. Consequently transplanting the available monitoring algorithms from the wired monitoring system directly is not feasible. It is imperative to develop appropriate algorithms for this distributed monitoring.

#### **4.4.2 Sustainable Operation of the Wireless Sensor Network**

Sensors, data acquisition systems, communication and processing units require sustainable power for truly autonomous operation. Sustainable operation of a sensor network platform is determined by the correlation of three metrics: (1) Peak energy consumption of the sensor node components, (2) energy harvesting/generation capability, and (3) rechargeable battery capacity. If peak sensor energy consumption can eventually drain the battery, the system is deemed not sustainable. Therefore, designing intelligent hardware and software protocols is necessary for achieving energy and service equilibrium to enable the on-going sensing operations. In the following subsections, design decisions for achieving sustainability are highlighted with respect to these metrics.

Several standards exist for RF communications such as IEEE 802.11 (WLAN), Bluetooth and IEEE 802.15.4 (ZigBee). Among these standards, ZigBee has become a popular choice in WSN applications due to its low power requirements and adequate data rates (up to 250Kbps). For instance, a common chip for ZigBee is Texas Instrument's CC2420 2.4 GHz RF transceiver which has been widely used in other smart sensors such

as MicaZ and Mica2 [53]. RF chip transmission power output is an important choice for the overall operation of the WSN. Transmission power determines (i) the communication distance, (ii) current consumption and (iii) battery output capacity. Therefore, sensor deployment (i.e. the proximity of the neighboring nodes) for infrastructure structural system should be done carefully by analyzing the power requirements and sensor node distances.

RF communication consumes significantly more power than sensor front-end or microcontroller units. However, distributed computing strategies associated with smart sensors for health monitoring requires complex computation and processing [54]. Several new sensor technologies follow this trend such as iMote2 [55] which is based on Intel XScale processor. On the other hand, FPGAs (Field-Programmable Gate Array) provide reconfigurable logic, tremendous flexibility and dedicated data-path logic for custom data processing. This enables previously unattainable computation and control to be realized at the sensor node. New FPGA technologies target low power sensor applications with ultra-low power standby and active mode selections [56].

**4.4.2.1 Energy Harvesting** Among all energy harvesting techniques, solar energy is the most convenient and suitable for structural health monitoring applications. Photovoltaic cells provide the highest power concentration ( $100 \text{ mW/cm}^2$ )[57]. Structural systems such as bridges can utilize the ambient solar energy by coupling solar panels with sensor nodes. Another energy source, although limited in power generation, is piezoelectric material in which mechanical strains across a material layer generate a surface charge. Several

companies such as Microstrain, Inc. produce piezoelectric energy harvesters. These harvesters can produce up to 30mW at 3.2 VDC with 1.5 g input vibrations.

Solar and piezoelectric energy harvesters can be simultaneously deployed for redundant and fault-tolerant monitoring operation: The sensors located under direct sunlight are equipped with two sustainable sources: solar and piezoelectric. The system can utilize an intelligent controller to switch between available sources (solar or vibration). For instance, during the daytime when sun irradiation is plentiful, solar provides the main power not only to power the smart sensors but also to charge up the backup battery. During the night or cloudy situations, the backup battery and the piezoelectric harvesters can act as the power source. A multiple-input power electronic converter needs to be implemented to add the energy of both these sources for energy diversification and increased reliability. The combination of various energy sources provides adequate power to energize the sensors and supply the power required for the SoC computation and RF communication.

Other energy harvesting systems, such as mini generators using bridge vibrations as the power source, or micro wind turbines, have also been considered for health monitoring applications, however to a much lesser extent than solar power systems.

**4.4.2.2 Power Management** For sustainability, not only is energy harvesting is critical, but efficient power management is also necessary. Power management and maintenance of a reliable operation is ensured by:

- Removing the load from energy harvesting source (putting the SoC system into sleep mode) if power reserves are less than a threshold.
- Minimizing the operations requiring high power consumption such as frequent and/or redundant raw data transmissions.

- Reserving minimum emergency power for critical instances of sensing such as when the traffic load is heavy and/or unexpected severe environmental changes occur.
- Utilizing ultra-low power components with minimal standby current.
- Transmitting only when there is an anomaly or a major change in the structural health to be reported.
- By integrating smart SoC processors, sensor nodes are capable of selfmonitoring their power generation and power consumption continuously. For continuous use, a power reserve must be provided in the form of battery to avoid power shortages. Using rechargeable energy storage such as high capacity (>5000mAh) Li-Ion/Polymer batteries, the power harvested by photovoltaic cells or piezoelectric energy sources can extend over a long period of time.

## 4.5 Structural Health Monitoring System of an In-service Highway Bridge

A Structural Health Monitoring System (SMH) using wireless Sensor Networks for an in-service 6-Span Precast Segmental Box Girder Bridge has been devised (see Section 2.5 for bridge description), which will be installed and operated by the Public Works Authority - Qatar (Ashghal, PWA). The deployment of Wireless Sensor Networks in the bridge will be implemented to evaluate the bridge response and demonstrate the ability of the proposed long-term monitoring systems to successfully perform on the bridge. The layout of the sensory system for the bridge is demonstrated in this section. The sensors are in four major types: accelerometers, temperature sensors, weigh-in-motion sensors, and strain gauges.

### 4.5.1 Accelerometers

A total of 36 Accelerometers were installed both on the bridge super-and substructures. As shown in Figure 4.4, one tri-axial accelerometer (A0), nine bi-axial (A2, A3, A5, A7, A9, A13, A15, A17 and A20), and twenty six uni-axial (A1, A4, A6, A8, A10, A11, A12, A14, A16, A18, A19, A21, A22 to A35) were installed. The accelerometers are located such that the longitudinal, lateral, torsional, and vertical motions of the bridge deck and piers can be measured. Thus, one bi-axial accelerometer will be installed on the south side for measuring the accelerations in the vertical and lateral directions, while one uni-axial accelerometer will be installed on the north side to measure the vertical acceleration.

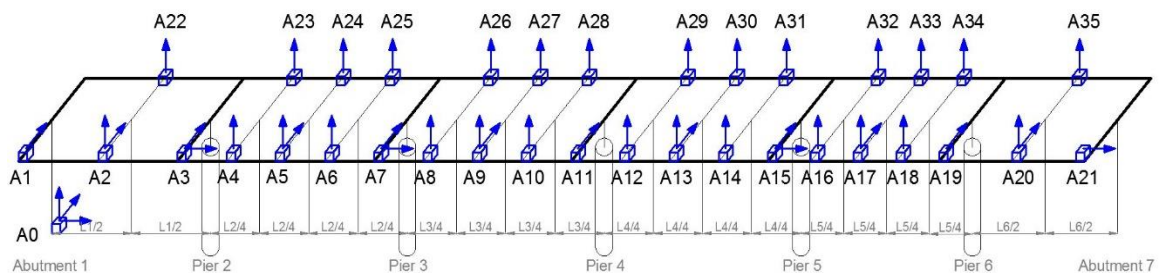


**Figure 4.4** Schematic Layout of the Accelerometers.

The positions of A1 to A35 are in respectively in the middle and quarter points of the spans (see Figure 4.4). Except for A0, which will be installed against the end wall at Abutment 1 to measure the ground motion in the three directions, accelerometers (A1 to A35) should be mounted on the floor surface inside the box-girder, by brackets bolted into the concrete, to measure the superstructure vibration at different positions.

#### 4.5.2 Strain Gauges

There are 67 strain gauges which will be installed in the bridge. Sixty four strain meters will be embedded in the bridge superstructure (see Figure 4.5), and three will be embedded in pier 3. Sections A1 to A6 are at the middle of each span, sections B1 to B5 are at the end of spans above the piers. The three strain meters installed in pier 3 are at the same elevation, measuring vertical strains at the three equally dividend points of the periphery of a circular cross section to obtain information of the static gravity load on pier 3. The strain meters are assumed to develop deformations consistent with the concrete, thus measuring the strain of the concrete at that position.

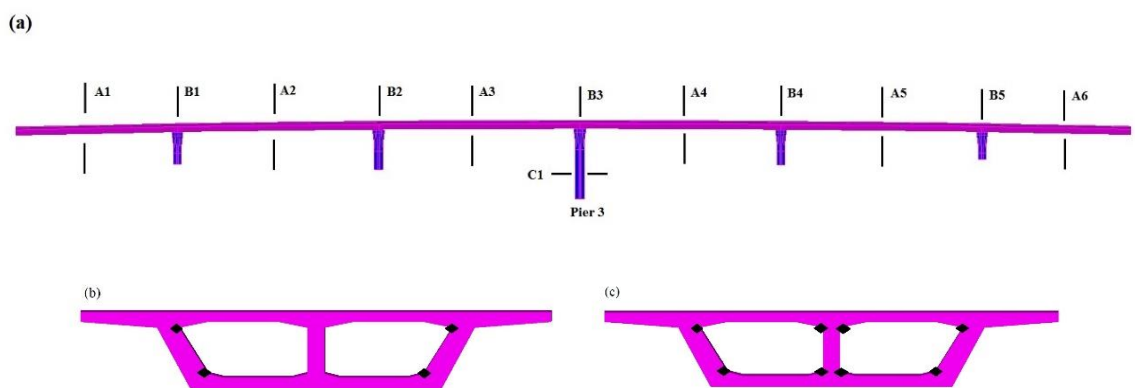


**Figure 4.5** Distribution of strain gauges in the bridge, (a) Sections monitored, (b) A1 to A6 cross sections, (c) B1 to B5 cross sections.

### 4.5.3 Temperature Sensors

Ten temperature sensors will be installed across mid-section on span 1 and 4. The schematic of the sensor locations is shown in Figure 4.6. The temperature sensors measure ambient and inside box girder temperatures. Of the ten temperature sensors, two measure the concrete deck temperature, two measures the temperature in box girder corners, and the other one record ambient temperature outside of the box girder.

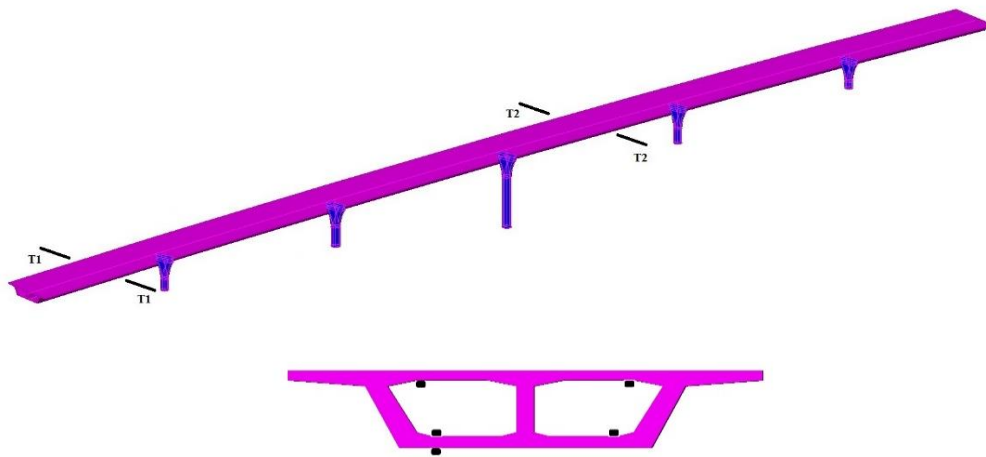


**Figure 4.6** Locations of Temperature sensors for long-term monitoring (a) Sections monitored, (b) T1 and T2 cross sections.

Temperature sensors will be installed at the same sections as the strain gauges. These sensors are measuring temperatures, which can be correlated with the strain gauge measurements in order to observe the influence of temperature conditions on deformation caused by traffic. Performing global condition monitoring on several bridges during the past decade, it was found that the natural frequencies of the bridge are varying with respect to changes of the structural temperature. Hence, monitoring environmental condition such as temperature is crucial for vibration based SHM systems.

#### **4.5.4 Weigh-in-motion (WIM) Stations**

The traffic loads on the bridge can be monitored by four dynamic WIM stations which were respectively installed in four lanes of the carriageways (two east-bound and two west-bound) at the west side approach slab. Each sensor is composed of two bending path pads and two magnetic loop detectors. The two bending path pads respectively placed on the left and right hand sides of the lanes were used for vehicle weight detection. The two magnetic loop detectors respectively installed in the front and rear of the carriageways at a defined distance were used for measuring axle numbers, axle length, as well as vehicle speed and height.

### **4.6 Conclusions**

Designing a SHM system is a systematic work integrating various expertise. In this chapter first the design criteria of SHM for a large-scale bridge is outlined. The commonly used types of sensory systems is then introduced. As a new and potentially promising sensing, transmission and monitoring system method, wireless monitoring is specially described in this chapter. Moreover, design and realization of power harvesting and power usage optimization for self-sustainable operation of SMH monitoring systems using wireless sensor networks is briefly discussed.

Finally, the long-term Structural Health Monitoring System using Wireless Sensor Networks (WSNs) for an in-service highway bridge is introduced. The results obtained from the FEA has been utilized to determine sensor locations and measurement types and could effectively minimize the number of sensors, data for transmission, and volume of data for processing. Once the hardware of the monitoring system is in place, continuous monitoring of the structure will be performed. Through continuous monitoring of the



dynamic response, vibrational features of the structure can be identified in terms of modal parameters. Next, damage localization will be performed based on the comparison of identified modal parameters with the initial values determined for the structure in its perfect condition. Finite Element Model Updating is then can be performed to update the structural model to reflect the change in structural dynamic response over time. This will provide the basis for the future use of the updated model to predict the capacity and remaining life of the structur

## CHAPTER 5

### OPERATIONAL MODAL ANALYSIS

#### 5.1 Fundamentals of Operational Modal Analysis

The expression Operational Modal Analysis means methods of modal identification which are based on response measurements only. Early applications of this discipline can be traced back to the beginning of modal testing in 1960s. The first applications of OMA were mainly based on the analysis of Power Spectral Density (PSDs) and the identification of Operational Deflection Shapes (ODSs). An ODS represents the deflection of a structure at a particular frequency under a generic input and it is usually the result of the contribution of different modes and ODSs are a close estimate of the actual mode shapes under certain assumptions. In the 1990s a number of methods working in time domain were developed and applied in combination with correlation functions, such as Natural Excitation Techniques (NExT). In the same period the use of ARMA models for modal parameter estimation started spreading and at the end of the 1990s new effective output-only modal identification techniques, such as the Frequency Domain Decomposition (FDD) and the Stochastic Subspace Identification (SSI) became available which could overcome the limitations of the previous techniques in dealing with closely spaced modes and noise[13]. Nowadays, OMA is a widely accepted tool for modal identification and has been applied to bridges [58-60], buildings [61, 62], historical structures [63], offshore platforms [64], wind turbines [65], dams [66], stadia [67]. Applications to ships [68], car bodies [69], trucks [70], engines [71] and rotating machinery are, instead, directly related to the mechanical engineering field. In aerospace engineering, examples of output-only tests

concern modal identification of aircrafts and shuttles by mean of in-flight tests and studies about flutter phenomena [72].

OMA techniques are based on the following assumptions:

- **Linearity:** the response of the system to a given combination of inputs is equal to the same combination of the corresponding outputs;
- **Stationarity:** the dynamic characteristics of the structure do not change over time, which means, coefficients of differential equations describing the problem are constant with respect to time;
- **Observability:** test setup must be defined in order to be able to measure the dynamic characteristics of interest (nodal point must be avoided in order to detect a certain mode for instance).

As mentioned before, OMA is based on the dynamic response of the structure under test to noncontrollable and immeasurable loadings such as environmental and operational loads (traffic, wind, etc.) unlike traditional modal testing. Consequently, some assumptions about the input are needed. First of all, it is assumed to be a stationary zero mean Gaussian white noise, which implies that input is characterized by a flat spectrum in the frequency range of interest and, hence, it gives a broadband excitation, so that all modes are excited [13]. Since all modes are equally excited, the output spectrum contains full information about the structure. From a mathematical point of view, signals are completely described by their correlation functions or by their counterpart in the frequency domain, the auto and cross power spectra. However, that input actually has a spectral distribution of its own which is not necessarily flat. Thus, modes are weighted by the spectral distribution of the input force and the response shows information originating not only from structural modes but also from the excitation signal. As a result, actual modes must be selected between information not related to physical modes, such as the ones due to input forces,

measurement noise and harmonic vibrations created by rotating parts. Secondly, the assumption of broadband excitation ensures that all the structural modes in the frequency range of interest are excited. Assuming that the combined system is excited by a random input, the second order statistics of the response carry all the physical information about the system and play a fundamental role in output-only modal identification [13].

## **5.2 Basic Concepts of Stationary Random Data and Processes**

The data observed from a physical phenomenon which can be described by an explicit mathematical relationship called deterministic. The observed free vibration response of a Single Degree Of Freedom (SDOF) system under a set of initial conditions is an example of deterministic data, since it can be defined by an explicit mathematical expression based on the mass and stiffness properties of the system. On the other hand, random data cannot be described by explicit mathematical relationships, therefore, the exact value at a certain time cannot be predicted and they must be described in probabilistic terms.

A random or stochastic process is the combination of all possible physical understanding of the random phenomenon. A sample function is a single time history representing the random phenomenon which is one of its physical realizations. A sample record is a sample function observed over a finite time interval and it can be thought as the observed result of a single experiment. In the following, focusing the attention in Stationary Random Processes (SRP) and in particular, Stationary and Ergodic Random Processes (SERP).

A collection of sample functions which also called ensemble is needed to characterize a random process. The mean value of the random process can be computed from the instantaneous values of each function in the ensemble at that time as follows:

$$\mu_x(\bar{t}) = \lim_{K \rightarrow \infty} \frac{1}{K} \sum_{k=1}^K x_k(\bar{t}) \quad (5.1)$$

Where  $x_k(\bar{t})$  is the k-th function in the ensemble, at a certain time instant  $\bar{t}$ .

Similarly, the autocorrelation function can be computed by taking the ensemble average of the product of instantaneous values at time instants  $\bar{t}$  and  $\bar{t} + \tau$ :

$$R_{xx}(\bar{t}, \bar{t} + \tau) = \lim_{K \rightarrow \infty} \frac{1}{K} \sum_{k=1}^K x_k(\bar{t}) x_k(\bar{t} + \tau) \quad (5.2)$$

Whenever the quantities expressed by Equations (5.1) and (5.2) do not change when the considered time instant  $t$  varies, the random process is said to be stationary. The mean value is independent of the time  $t$  and the autocorrelation depends only on the time lag  $\tau$  for stationary random processes,

$$\mu_x(\bar{t}) = \mu_x \quad (5.3)$$

$$R_{xx}(\bar{t}, \bar{t} + \tau) = R_{xx}(\tau) \quad (5.4)$$

In the following sections the basic properties for stationary random records such as probability density functions, auto- and cross-correlation functions, autoand cross-spectral density functions are briefly discussed. In fact, the above-mentioned properties are primary tools of signal analysis and commonly used to prepare the data for most OMA techniques.

### 5.2.1 Spectral Density Functions

Power spectral density function (PSD) is a statistical function which shows the strength of the variations (energy) as a function of frequency. In other words, it shows at which frequencies variations are strong and at which frequencies variations are weak. The unit of PSD is energy per frequency(width) and energy can be obtain within a specific frequency range by integrating PSD within that frequency range. Computation of PSD is done directly by the method called Fast Fourier Transform (FFT) or computing autocorrelation function and then transforming it which will be briefly described. PSD is a useful tool for identifying oscillatory signals in time series data and their amplitude.

Considering a sample record  $x_k(t)$  of finite duration T from stationary random processes. Its Fourier transforms exist as a consequence of the finite duration of the signals and can be written as follows:

$$X_k(f, T) = \int_0^T x_k(t) e^{-i2\pi f t} dt \quad (5.5)$$

and the two-sided auto- and cross-spectral density functions are defined as follows:

$$S_{xx}(f) = \lim_{T \rightarrow \infty} E \left[ \frac{1}{T} X_k^*(f, T) X_k(f, T) \right] \quad (5.6)$$

where \* represents complex conjugate. Two-sided means that  $S(f)$  is defined for  $f$  in the range  $(-\infty, +\infty)$  and the expected value operation is working over the ensemble index  $k$ . The one-sided auto- and cross-spectral density functions, with  $f$  varying in the range  $(0, +\infty)$ , are given by:

$$G_{xx}(f) = 2S_{xx}(f) = 2 \lim_{T \rightarrow \infty} E[|X_k(f, T)|^2] \quad 0 < f < +\infty \quad (5.7)$$

The two-sided spectral density functions are more commonly utilized in theoretical derivations and mathematical calculations, whereas the one-sided spectral density functions are typically used in the applications. In practical applications the one-sided spectral density functions are always the result of Fourier transforms of records of finite length ( $T < \infty$ ), along with averaging of a finite number of ensemble elements.

Before analyzing the computation of PSDs in practice, it is worth noting that PSDs and correlation functions are Fourier transform pairs. Accordingly, the two-sided spectral density functions are the Fourier transforms of the correlation functions:

$$S_{xx}(f) = \int_{-\infty}^{+\infty} R_{xx}(\tau) e^{-i2\pi f\tau} d\tau \quad (5.8)$$

Equation (5.8) is also called the Wiener-Khinchin relation. The auto-spectral density functions are real-valued functions, on the other hand, the cross-spectral density functions are complex-valued. In terms of one-sided spectral density functions, the correspondence with the correlation functions is given by:

$$G_{xx}(f) = 4 \int_0^{\infty} R_{xx}(\tau) \cos(2\pi f\tau) d\tau \quad (5.9)$$

It is worth pointing out two important properties of Gaussian random processes for practical applications. First, it can be shown that if a Gaussian process undergoes a linear transformation, the output is still a Gaussian process [73]. Furthermore, assuming a sample record of an ergodic Gaussian random process with zero mean, it can be proven that the Gaussian probability density function is completely determined by the knowledge of the auto-spectral density function [73].

In fact, considering that:



$$\sigma_x^2 = \int_{-\infty}^{+\infty} x^2 p(x) dx \approx \int_0^{\infty} G_{xx}(f) df \quad (5.10)$$

$G_{xx}(f)$  alone determines  $\sigma_x$  [73]. Hence, spectral density functions and their Fourier transform pairs (the correlation functions) play a fundamental role in the analysis of random data.

In practical applications, PSDs can be obtained by computing the correlation functions first and then Fourier transforming them. This approach is known as the Blackman-Tukey procedure [13]. Another approach, known as the Welch procedure, is, instead, based on the direct computation of the FFT of the records and the estimation of the PSDs in agreement with Equation (5.7). The Welch procedure is less computational demanding than the Blackman-Tukey method, but it requires some operations on the signal in order to improve the quality of the estimates.

Additionally, based on Equation (5.7), the one-sided auto-spectral density function can be estimated by dividing a record into  $n_d$  contiguous segments, each of length  $T=N\Delta t$ , Fourier transforming each segment and then computing the auto-spectral density through an ensemble averaging operation over the  $n_d$  subsets of data [13].

Even if the direct computation via FFT of the spectral density function is advantageous from a computational point of view, specific strategies are required to eliminate the errors originating from the fact that the estimates are based on records of finite length. A sample record  $x(t)$  can be interpreted as an unlimited record  $v(t)$  multiplied by a rectangular time window  $u(t)$ :

$$x(t) = u(t) v(t) \quad u(t) = \begin{cases} 1 & 0 \leq t \leq T \\ 0 & \text{elsewhere} \end{cases} \quad (5.11)$$

Therefore, the Fourier transform of  $x(t)$  is given by the convolution of the Fourier transforms of  $u(t)$  and  $v(t)$ . The Fourier transform of a rectangular signal is basically a sinc function (Figure 5.1) with side lobes characterized by a fairly large amplitude with respect to the main lobe (the amplitude difference is just  $-13$  dB).

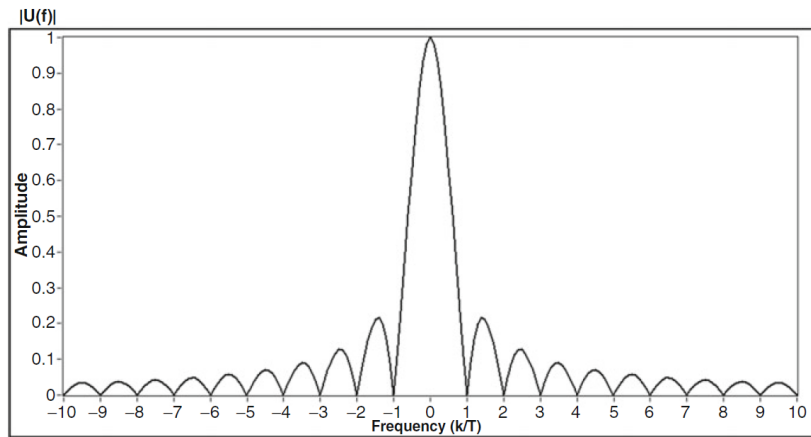


**Figure 5.1** Discrete Fourier Transform (DFT) of a rectangular window: amplitude.

The large side lobes of  $|U(f)|$  allow the energy at a certain frequency to spread to nearby frequencies, causing large amplitude errors. This phenomenon is also known as leakage and it may introduce significant distortions in the estimated spectra, in particular in the presence of data characterized by narrow bandwidth. Nevertheless, it does not happen when the analyzed data are periodic with a period equal to the record length. In such a case, in fact, the discrete frequency values, equally spaced at  $\Delta f=1/T$ , coincide with zeros of the spectral window in the frequency domain with the only exception of the

frequency line in the main lobe. The result is an exact reproduction of the correct spectrum. Thus, in order to suppress the leakage problem, data are made periodic by tapering them by an appropriate time window, which eliminates the discontinuities at the beginning and end of the analyzed record. There are different options for the choice of the window [74]. Here, the most commonly employed window is introduced. It is the full cosine tapering window, also known as Hanning window, which is given by:

$$u_{Hanning}(t) = \begin{cases} 1 - \cos^2\left(\frac{\pi t}{T}\right) & 0 \leq t \leq T \\ 0 & \textit{elsewher} \end{cases} \quad (5.12)$$

The highest side lobe level of the Hanning window is 32 dB below the main lobe. Thus, leakage is minimized. The use of the Hanning window to compute spectral density estimates by Fourier transform techniques implies a loss factor of 3/8. As a consequence, a rescaling is needed to obtain spectral density estimates characterized by the correct magnitude.

### **5.2.2 Fundamentals of Matrix Algebra**

Most OMA methods are based on fitting of an assumed mathematical model to the measured data. In such a case, the ultimate goal is to determine the unknown modal parameters of the system from the measured response of the structure under certain assumptions about the input. This is an example of inverse problem. The solution of inverse problems is based on matrix algebra, including methods for matrix decomposition.

Additionally, Matrix algebra plays an important role in the case of those OMA methods that extract the modal parameters without assumptions about the system that produced the measured data. Thus, a review of basics of matrix algebra and of some methods for the solution of inverse problems is presented to understand the mathematical background of the OMA methods described in consequent sections.

Consider the generic matrix:

$$[A] = \begin{bmatrix} a_{1,1} & \cdots & a_{1,M} \\ \cdots & a_{i,j} & \cdots \\ a_{L,1} & \cdots & a_{L,M} \end{bmatrix} \quad (5.13)$$

of dimensions  $L \times M$ . Its generic element is  $a_{i,j}$ , where the index  $i=1, \dots, L$  indicates the row number and the index  $j=1, \dots, M$  refers to the column number. The matrix  $[A]$  can be real-valued or complex valued, depending if its elements are real or complex numbers.

When the matrix  $[A]$  presents a linear operator transforming a certain vector  $\{x\}$  into a new vector  $\{y\}$ :

$$\{y\} = [A]\{x\} \quad (5.14)$$

When the vector  $\{y\}$  in Equation (5.14) can be computed via the matrix multiplication  $[A]\{x\}$ , and via the scalar product  $\lambda\{x\}$ ,  $\lambda$  is defined an eigenvalue of  $[A]$  and  $\{x\}$  is the corresponding eigenvector. The eigenvalues are obtained as a solution of the characteristic equation:

$$\det([A] - \lambda[I]) = 0 \quad (5.15)$$

and the corresponding eigenvectors are determined by replacing the obtained eigenvalues  $\lambda_k$  into Equation (5.16):

$$([A] - \lambda_k[I])\{x_k\} = \{0\} \quad (5.16)$$

If the matrix  $[A]$  is Hermitian or symmetric, the eigenvectors corresponding to distinct eigenvalues are orthogonal (their dot product is zero) and its eigenvalues are real. If the symmetric matrix  $[A]$  is positive-definite the eigenvalues are real and positive and the matrix  $[A]$  is invertible.

The matrix inversion can be implemented more effectively when dealing with systems of equations by decomposing the matrix into factors. There are different types of

matrix decomposition methods. The eigenvalue decomposition (EVD) provides an expression for the invertible square matrix  $[A]$  as a product of three matrices:

$$[A] = [U][\Sigma][V]^T \quad (5.17)$$

where  $[\Sigma]$  of dimensions  $L \times M$  is a rectangular diagonal matrix containing the singular values which arranged in descending order. The first  $r$  singular values are positive, while the remaining singular values  $\sigma_{r+1}, \dots, \sigma_M$  are all equal to zero.  $[U]$  and  $[V]$  are orthogonal matrices of dimensions  $L \times L$  and  $M \times M$ , respectively. The column vectors  $\{u_1\}, \dots, \{u_r\}$  of  $[U]$  span the range of  $[A]$ , while the vectors  $\{v_{r+1}\}, \dots, \{v_M\}$  span the null space of  $[A]$ . If  $[A]$  is a complex-valued matrix, the Singular Value Decomposition (SVD) is generalized by replacing the transpose with the Hermitian operator.

The SVD has many applications in signal processing and for the solution of inverse problems, including the computation of pseudo-inverse, least squares fitting of data, matrix approximation and rank determination. In the common case in which  $[A]$  is a square, real-valued matrix,  $[\Sigma]$  can be explained as a scaling matrix, while  $[U]$  and  $[V]^T$  can be regarded as rotation matrices. Hence, the SVD can be interpreted as a series of three geometrical transformations, namely a rotation, a scaling, and another rotation [13]. The SVD is also used for the computation of the Moore-Penrose pseudoinverse of a matrix.

Other decomposition methods such as LQ decomposition and RQ decomposition for square matrices result in the conversion of the matrix  $[A]$  into a product of an orthogonal

matrix [Q] and an upper [R] or lower [L] triangular matrix. The Cholesky factorization, instead, is a decomposition of a real-valued, symmetric, and positive definite matrix into the product of a lower triangular matrix and its transpose. Further details about matrix algebra and decompositions can be found elsewhere [75].

### 5.2.3 Inverse Problems

A common approach in OMA is the fitting of a hypothesized model to the measurements in order to obtain the unknown modal parameters. The approach to fitting depends on the selected model. For explaining the fundamentals, in this section the main concepts are demonstrated with reference to a simple and general polynomial function:

$$y(x) = c_0 + c_1x + c_2x^2 + \dots + c_{L-1}x^{L-1} \quad (5.18)$$

No specific references are made to the theoretical background of OMA at this stage, but the application of these concepts in different contexts is straightforward and it will become more clear when the theory of some OMA methods is reviewed in the subsequent sections.

Assuming that M measurements have been carried out, the L unknown model parameters  $(c_0, c_1, \dots, c_{L-1})$  can be determined from the following set of M equations which are rearranged in matrix form as:

$$\{y\} = \begin{Bmatrix} y_1 \\ \dots \\ y_i \\ \dots \\ y_M \end{Bmatrix} = \begin{bmatrix} 1 & x_1 & x_1^2 & \dots & x_1^{L-1} \\ \dots & \dots & \dots & \dots & \dots \\ 1 & x_i & x_i^2 & \dots & x_i^{L-1} \\ \dots & \dots & \dots & \dots & \dots \\ 1 & x_M & x_M^2 & \dots & x_M^{L-1} \end{bmatrix} \begin{Bmatrix} c_0 \\ \dots \\ c_i \\ \dots \\ c_{L-1} \end{Bmatrix} = [M]\{c\} \quad (5.19)$$

Considering that the setting of the problem in matrix form does not need a linear functional relation between  $y$  and  $x$ . A linear combination of basis functions of  $x$  is also suitable. Typically, there are more measurements than unknowns ( $M > L$ ), so that an overdetermined set of equations can be defined and measurements are noisy. It is worth mentioning that when the number of unknowns  $L$  exceeds the number of equations  $M$ , the problem is definitely underdetermined. Thus, the inverse problem cannot lead to a unique solution and additional information has to be provided or the number of unknowns has to be reduced. On the other hand, when  $M > L$  the problem can not only be overdetermined, but also be even determined or underdetermined, depending on the eventual presence of analogous measurements which do not provide additional information. Therefore, the rank of the matrix in Equation (5.19) actually determines if the problem is overdetermined or underdetermined. But in practical applications, the sole determination of the rank of a matrix can be misleading due to the presence of measurement noise.

In similar conditions the SVD of the matrix can provide more valuable information about the type of inverse problem. As a matter of fact, the condition number  $\kappa$  which is the ratio between the maximum and minimum absolute values of singular values, can be computed to evaluate whether the matrix is noninvertible ( $K = \infty$ ), ill-conditioned ( $K$  very large) or invertible (small  $K$ ). In ill-conditioned problems the small singular values magnify



the errors, so considering only the subset of the largest singular values can reduce their effect. The selection of the number of singular values to be maintain is usually depends on sorting of the singular values and identification of jumps [13].

Assuming that a curve fitting the measured data has been found and the functional relation between  $y$  and  $x$  in Equation (5.18) has been established, there will be an error (or residual) corresponding to the  $i$ -th measurement. It can be computed as difference between the predicted ( $y_{i,pred}$ ) and the measured ( $y_{i,meas}$ ) value of  $y$ :

$$\varepsilon_i = y_{i,pred} - y_{i,meas} \quad (5.20)$$

Therefore, the objective of the analysis is the estimation of the unknown coefficients ( $c_0, c_1, \dots, c_{L-1}$ ) from the measured data in a way able to minimize the sum of the residuals when all measurements are considered.

Different definitions for the residuals can be selected, considering that the selected error definition has an influence on the estimation of the unknown parameters. For instance, when the data are characterized by the presence of very large and very small values in the same set, the computation of the residuals according to Equation (5.20) skew the inversion towards the largest values. Hence, one of the following definitions of residual can be considered as an alternative:

$$\varepsilon_i = \frac{y_{i,pred} - y_{i,meas}}{y_{i,pred}} \quad (\text{proportional error}) \quad (5.21)$$

$$\varepsilon_i = \log(y_{i,meas}) - \log(y_{i,pred}) \quad (\text{log difference}) \quad (5.22)$$

Additional error definitions can be found in the literature [76].

A global evaluation of the quality of the fit can be obtained from the computation of the norm of the vector of residuals  $\{\varepsilon\}$ :

$$\{\varepsilon\} = \begin{Bmatrix} \varepsilon_1 \\ \dots \\ \varepsilon_i \\ \dots \\ \varepsilon_M \end{Bmatrix} \quad (5.23)$$

The generic n-norm is given by:

$$L_n = \sqrt[n]{\sum_i |\varepsilon_i|^n} \quad (5.24)$$

The order of the norm is related to the weight placed on the larger errors, in other words the higher the order of the norm, the higher the weight of the larger errors. Three notable norms are:

$$L_1 = \sum_i |\varepsilon_i| \quad (5.25)$$

$$L_2 = \sqrt{\sum_i |\varepsilon_i|^2} = \sqrt{\{\varepsilon\}^T \{\varepsilon\}} \quad (5.26)$$

$$L_\infty = \max(|\varepsilon_1|, \dots, |\varepsilon_i|, \dots, |\varepsilon_M|) \quad (5.27)$$

The  $L_1$  norm provides a powerful solution, since it is not sensitive to a few large errors in the data. The  $L_2$  norm is compatible with additive Gaussian noise present in the data and the  $L_\infty$  norm considers only the largest error and is the most sensitive to errors in the data.

Based on the previous definitions, the least squares solution of the inverse problem can be defined as the set of values of the coefficients  $(c_0, c_1, \dots, c_{L-1})$  that minimizes the  $L_2$  norm of the vector of residuals. Therefore, setting the derivative of this  $L_2$  norm with respect to  $\{c\}$  equal to zero, under the assumption that  $[M]^T [M]$  is invertible the least squares solution provides the following estimate of the model parameters:

$$\{c\} = ([M]^T[M])^{-1}[M]^T\{y_{meas}\} = [M]^+\{y_{meas}\} \quad (5.28)$$

The least squares method is a standard approach to the approximate solution of overdetermined systems. It works well when the uncertainties affect the dependent variable. If substantial uncertainties affect also the independent variable, the total least square approach has to be adopted. This method is able to consider the observational errors on both dependent and independent variables. More mathematical details of the method can be found in the literature [75].

### 5.3 Classification of OMA Techniques

A classical distinction between Modal identification methods is based on the domain of implementation. OMA methods directly based on time histories of the output signals are referred to as time domain methods. Methods based on spectral density functions and Fourier transform of signals are, instead, referred to as frequency domain methods. Even if this distinction may look artificial, since they simply consider different representations of the same signal and it is always possible to transform signals from one domain to the other, there are some differences in terms of practical applications. In fact, time domain methods are usually better conditioned than the frequency domain counterpart. This is mainly related to the effect of the powers of frequencies in frequency domain equations. Moreover, time domain methods are usually more suitable for handling noisy data, and they avoid most signal processing errors such as leakage if applied directly to raw time domain data. On the other hand, in noisy measurement conditions, averaging is easier and more efficient in frequency domain.

Another distinction is between Single Degree Of Freedom (SDOF) and Multiple Degree Of Freedom (MDOF) methods based on the assumption about the number of modes determining the structural response. When in a certain frequency band only one mode is assumed to be important and the structural response in that frequency range depends only on that mode, the parameters of this mode can be determined separately, leading to the SDOF methods. Even if these methods are very fast and characterized by a low computational burden, the SDOF assumption is a reasonable approximation only if the modes of the system are well decoupled. On the other hand, MDOF methods are necessary when dealing with close coupled modes or even coincident modes to properly identify the different modes contributing to the overall structural response.

## **5.4 Operational Modal Analysis in the Frequency Domain**

### **5.4.1 The Basic Frequency Domain (Peak-Picking) Method**

The most undemanding method for modal parameter estimation from output-only data is the Basic Frequency Domain (BFD) method [77], also called the Peak-Picking method. In the past, it has been widely used for identification purposes in civil engineering and a practical implementation was made by Felber [78]. The name of the method is related to the fact that natural frequencies are determined as the peaks of the Power Spectral Density (PSD) plots, obtained by converting the measured data to the frequency domain by the Discrete Fourier Transform (DFT).

The BFD technique is a SDOF method for OMA. In fact, it is based on the assumption that, around a resonance, only one mode is dominant. When it happens, taking

into account the following expression for the Frequency Response Function (FRF) and that the input spectrum is assumed to be constant.

$$[H(\omega)] = \sum_{r=1}^N \left[ \frac{[A]_r}{j\omega - \lambda_r} + \frac{[A]_r^*}{j\omega - \lambda_r^*} \right] \quad (5.29)$$

being  $[A]_r$  the residue matrix,  $N$  the number of modes and  $\lambda_r$  the  $r$ -th eigenvalue. The output spectrum matrix, which can be expressed as follows:

$$[G_{yy}(\omega)] = \sum_{k=1}^N \sum_{r=1}^N \left[ \frac{[R_k]}{j\omega - \lambda_r} + \frac{[R_k^*]}{j\omega - \lambda_r^*} \right] [C] \left[ \frac{[R_s]}{j\omega - \lambda_s} + \frac{[R_s^*]}{j\omega - \lambda_s^*} \right]^H \quad (5.30)$$

can be approximated by considering only the contribution of the dominant mode, for example the  $r$ -th mode, as:

$$[G_{yy}(\omega)] \approx \frac{[R_r]}{j\omega - \lambda_r} + \frac{[R_r^*]}{j\omega - \lambda_r^*} \quad (5.31)$$

where the residues are related to the mode shape.

It is clear that in this case the power spectral density (PSD) matrix is of rank one. Therefore, at resonance any column of the PSD matrix can be considered as an estimate of the corresponding mode shape, up to a scaling factor being the input unmeasured.

From a practical point of view, first to identify the peaks corresponding to structural resonances, the trace of the PSD matrix (the sum of the autospectra) at each discrete frequency value is computed. Then, the mode shapes associated to the identified frequencies are obtained from one of the columns of the PSD matrix. A reference sensor for the computation of the cross-spectral densities with all other measurement channels has to be selected considering that reference sensor cannot be a sensor placed at a node of the mode shape. Depending on the geometry of the structure and the adopted sensor layout, a single reference sensor could be insufficient to identify all the modes and at least a couple of reference sensors with different orientation have to be adopted.

Additionally, Identification of actual natural frequencies can be carried out by looking not only at peaks of the spectra but also by inspecting the coherence function between two channels, defined as:

$$\gamma_{rs}^2(f) = \frac{|G_{rs}(f)|^2}{G_{rr}(f)G_{ss}(f)} \quad (5.32)$$

and assuming values between 0 and 1;  $G_{rs}(f)$  is the value of the cross-spectrum between channels  $r$  and  $s$  at the frequency  $f$ , while  $G_{rr}(f)$  and  $G_{ss}(f)$  are the values of the auto-spectra of channel  $r$  and channel  $s$ , respectively, at the same frequency.

If  $f$  is a resonant frequency, the coherence function is close to one because of the high signal-to-noise ratio at that frequency. This characteristic is helpful in the discrimination between real eigenfrequencies and peaks due to disturbances. Also, the coherence function can be useful for the identification of the nature of a mode. With the combination of information from spectra and coherence functions even it is possible to identify closely spaced modes. However, the success of the identification process heavily depends on the geometry of the structure and the skill of the analyst. Also, when the peaks in the spectra are not clear for instance in the case of noisy measurements, the results of modal identification suffer a certain degree of subjectivity.

The BFD method allows the evaluation of the modal properties and the accuracy of the estimated eigenfrequencies depends on the frequency resolution of the spectra. In other words, to obtain good natural frequency estimates, a fine frequency resolution is necessary. In order to estimate damping ratios from the spectra, it is suggested to use the half-power bandwidth method [77]. However, a number of studies have shown that they are not accurate [79, 80].

In summary, this method is very simple and not demanding from computational point of view which makes it a useful analysis tool for the analyst, especially during field tests, to get a quick insight about effectiveness of measurements and results of dynamic identification [13]. However, it suffers some drawbacks due to the SDOF assumption. The BFD technique works well when damping is low and modes are well-separated, but if these



conditions are violated it may lead to inaccurate results. In fact, the method, instead of the actual mode shapes, identifies the Operational Deflection Shapes (ODSs) which are a combination of all mode shapes. They are a good approximation of actual mode shapes only if one mode is dominant at the considered frequency. In case of closely-spaced modes, ODS is the superposition of multiple modes. Another important drawback is that the selection of eigenfrequencies can become a subjective task if the spectrum peaks are not very clear. Moreover, eigenfrequencies are estimated on a local basis by looking at single spectra and a fine frequency resolution is required in order to obtain a good estimation of the natural frequency.

#### **5.4.2 The (Enhanced) Frequency Domain Decomposition**

The main drawbacks of the BFD method have been overcome by the introduction of the Frequency Domain Decomposition (FDD) technique [69]. This method was originally applied to FRFs and was known as Complex Mode Indicator Function (CMIF) in order to point out its ability to detect multiple roots and possibility count the number of dominant modes at a certain frequency [81]. The method has been then better systematized by Brincker and applied to response spectrum data.

A theoretical verification of the method is based on the modal expansion of the structural response:

$$\{y(t) = [\Phi]\{p(t)\}\} \quad (5.33)$$

where  $[\Phi]$  is the modal matrix and  $\{p(t)\}$  the vector of modal coordinates. From Equation (5.33), the correlation matrix of the responses can be computed:

$$R_{yy}(\tau) = E [\{y(t + \tau)\}\{y(t)\}^T] = [\Phi][R_{pp}(\tau)][\Phi]^T \quad (5.34)$$

The PSD matrix can be obtained from Equation (5.34) by taking the Fourier transform:

$$[G_{yy}(\omega)] = [\Phi][G_{pp}(\omega)][\Phi]^H \quad (5.35)$$

Taking into account that the Singular Value Decomposition (SVD) of the PSD matrix at a certain frequency  $\omega$  the following factorization can be derived:

$$[G_{yy}(\omega)] = [U][\Sigma][V]^H \quad (5.36)$$

where  $[U]$  and  $[V]$  are the unitary matrices holding the left and right singular vectors and  $[\Sigma]$  is the matrix of singular values which should be arranged in descending order. Since

the PSD is a Hermitian and positive definite matrix,  $[U] = [V]$  and the decomposition of Equation (5.36) can be rewritten as:

$$[G_{yy}(\omega)] = [U][\Sigma][U]^H \quad (5.37)$$

The comparison between Equations (5.35) and (5.37) demonstrate that it is possible to identify a one-to-one relationship between singular vectors and mode shapes; furthermore, the singular values are related to the modal responses which can be used to define the spectra of equivalent SDOF systems characterized by the same modal parameters as the modes contributing to the response of the MDOF system under investigation. As mentioned before, the SVD provides the singular values arranged in descending order, so near a resonance the first singular value contains the information about the dominant mode at that frequency. Moreover, since the number of nonzero elements in  $[\Sigma]$  is the rank of the PSD matrix at the considered frequency, this feature is used to identify closely spaced or even coincident modes. In other words, the number of dominant singular values (the rank of the output PSD matrix) at a certain frequency the number of modes that give a significant contribution to the structural response at that particular frequency are equivalent.

Assuming at the frequency  $\omega$ , only one mode is dominant and also the selected frequency is associated to the peak of resonance of the  $k$ -th mode, the PSD matrix

approximates to a rank one matrix and there will be only one term on the right side of Equation (5.37):

$$[G_{yy}(\omega)] = \sigma_1 \{u_1\} \{u_1\}^H \quad \omega \rightarrow \omega_k \quad (5.38)$$

In such a case, the first singular vector  $\{u_1\}$  is an estimate of the mode shape of the k-th mode:

$$\{\hat{\phi}_k\} = \{u_1(\omega_k)\} \quad (5.39)$$

and the corresponding singular value  $\sigma_1$  belongs to the auto power spectral density function of the corresponding SDOF system. In case of repeated modes, the PSD matrix rank is equal to the number of multiplicity of the modes.

By comparing the mode shape estimate  $\{\hat{\phi}_k\}$  at the peak with the singular vectors associated to the frequency lines around the peak, the singular values whose singular vectors show a correlation with  $\{\hat{\phi}_k\}$  higher than a user-defined threshold can be identified, which called MAC Rejection Level. Such singular values define the equivalent SDOF PSD function. The Modal Assurance Criterion (MAC) is used as a measure of the correlation between two modal vectors [82]. This equivalent SDOF PSD function is used, when

applying the Enhanced Frequency Domain Decomposition (EFDD) algorithm [83, 84], to estimate the modal damping ratio and obtain an estimate of the natural frequency which is independent of the frequency resolution of the spectra computed by the Fast Fourier Transform (FFT) algorithm. In fact, an approximated correlation function of the equivalent SDOF system can be obtained by the inverse Fourier transform of the equivalent SDOF PSD function. From the free decay function of the SDOF system, the damping ratio can be calculated by the logarithmic decrement technique. A similar procedure is adopted in order to extract natural frequencies, carrying out a linear regression on the zero crossing times of the equivalent SDOF system correlation function and taking into account the relation of damped and un-damped natural frequency [13].

The FDD method allows to overcome the typical drawbacks of the BFD technique such as identification of closely spaced modes. However, it worth to mention that in this case the mode shape estimates could be biased. The singular vectors are forced to be orthogonal by the SVD, if the experimental mode shapes are also orthogonal the obtained estimates are unbiased. However, this is not always true; in such a case, estimation of the mode shape for the closely spaced modes are biased and the bias mainly affects the weak mode, while the mode shape estimate for the dominant mode is still good. The larger the difference between the first and second singular value, the smaller the error due to the bias. Hence, the mode shape estimates should be obtained from singular vectors at frequencies characterized by the largest difference between the first and second singular value. This frequency might be different from the frequency of the peak in the presence of closely spaced modes.

The method described above is the classical implementation of the FDD/EFDD method, however, alternate methods are possible to find in the literature [85, 86]. In particular, an alternative implementation of FDD based on EVD instead of SVD is also available [87]. It is worth mentioning the so-called Frequency-Spatial Domain Decomposition (FSDD) [62] as another variants of the FDD method, where spatial filtering has been applied to enhance the estimation of modal frequencies and damping ratios. The FSDD makes use of the mode shapes estimates computed via SVD of the output PSD matrix to enhance PSDs. The use of the estimated mode shapes as weighting vectors gives, results in an enhanced PSD which can be approximated as a SDOF system therefore, a SDOF curve fitter may be used to estimate the natural frequency and the damping ratio of the considered mode.

## **5.5 Spectral Kurtosis Estimation of Harmonic Excitations**

### **5.5.1 Theoretical Background**

The Spectral Kurtosis Estimator (SK) is a higher order unbiased statistical estimator associated with an accumulated Power Spectral Density (PSD) estimate, it is given by [88]:

$$SK = \frac{M+1}{M-1} \left( \frac{MS_2}{S_1^2} - 1 \right), \quad (5.40)$$

where  $S_1(f_k) = \sum_{i=1}^M P_i(f_k)$  represents the sum at each frequency bin,  $f_k, i = 0, N/2$ , of  $M$  consecutive FFT raw power estimates, and  $S_2(f_k) = \sum_{i=1}^M P_i^2(f_k)$  the sum of their squares. It is worth mentioning that in the case of a pure Gaussian time domain signal, statistical expectation of the SK estimator is unity at each frequency bin, although the power spectrum may have an arbitrary spectral shape.

In order to quantify the expected statistical fluctuations of the SK estimator around its unity mean, the exact analytical expressions of the infinite series of the statistical moments of the SK estimator can be obtained [88]. Its first four centralized standard moments in terms of the accumulation length  $M$  as follows:

$$\mu_1 = 1; \mu_2 = \frac{4M^2\Gamma(M+2)}{(M-1)\Gamma(M+4)}; \mu_3 = \frac{16M^3(5M-7)\Gamma(M+2)}{(M-1)^2\Gamma(M+6)}; \mu_4 = \frac{24M^4(2M^3+196M^2-370M+156)\Gamma(M+2)}{(M-1)^3\Gamma(M+8)} \quad (5.41)$$

where  $\Gamma(z) = \int_0^\infty t^{z-1} e^{-t} dt$  is the Euler's gamma function.

However, the variance  $\mu_2 \equiv \sigma^2$  of the SK estimator in Equation (5.41) is not sufficient for assigning standard symmetric deviations about the mean. A series expansion of  $\mu_3$  shows that the probability density function (PDF) of the SK estimator has a skewness that does not vanish faster than  $10/\sqrt{M}$ . Hence, the asymmetry of the PDF distribution around its mean must be taken into consideration, for small accumulation lengths  $M$ , in

order to estimate the true asymmetric statistical fluctuations of the SK estimator about its mean[88].

For  $M \geq 24$ , accurate detection thresholds of non-Gaussian spectral components corresponding to a preferred probability of false alarm (PFA) can be computed by providing a 4-moment Pearson Type IV approximation of the SK probability density function (PDF). This approach can be generalized and used for  $6 \leq M \leq 23$  by either deriving a 3-moment Pearson Type IV approximation or a more computationally convenient Pearson Type III (gamma distribution) approximation which can provide accurately enough PFA thresholds for most practical applications [88].

The Pearson Type III approximation of the SK cumulative probability distribution function (CF), assuming the shortcut notations  $\alpha = \frac{\mu_3}{2\mu_2}$ ,  $\beta = 4 \frac{\mu_2^3}{\mu_3^2}$ , and  $\delta = 1 - \frac{2\mu_2^2}{\mu_3}$ , can be written in the following form1:

$$CF(\xi, M) = \gamma\left(\beta, \frac{\xi - \delta}{\alpha}\right) / \Gamma(\beta) \quad (5.42)$$

where  $\gamma(\beta, x) = \int_0^x t^{\beta-1} e^{-t} dt$  is the incomplete gamma function. From Equation (5.42) the non-Gaussian SK detection thresholds,  $\xi_{lower} < 1$  and  $\xi_{upper} > 1$ , may be computed by equating  $CF(\xi_{lower}, M)$  and, respectively  $1 - CF(\xi_{upper}, M)$  to a desired PFA level, or to the standard  $3\sigma$  PFA probability of 0.13% on each side of the unity mean.



It is worth pointing out that the SK estimator is able to flag non-Gaussian spectral components and characterize their temporal dynamics relative to the integration time. If the excitation is relatively slowly decaying harmonic oscillations such as quasi-stationary harmonic excitation, the SK values will be bounded between the  $[0, 1]$  interval. On the other hand, in the case of a transient harmonic or Gaussian excitation which are rapidly decaying harmonic or stochastic oscillations, the SK takes a value larger than unity.

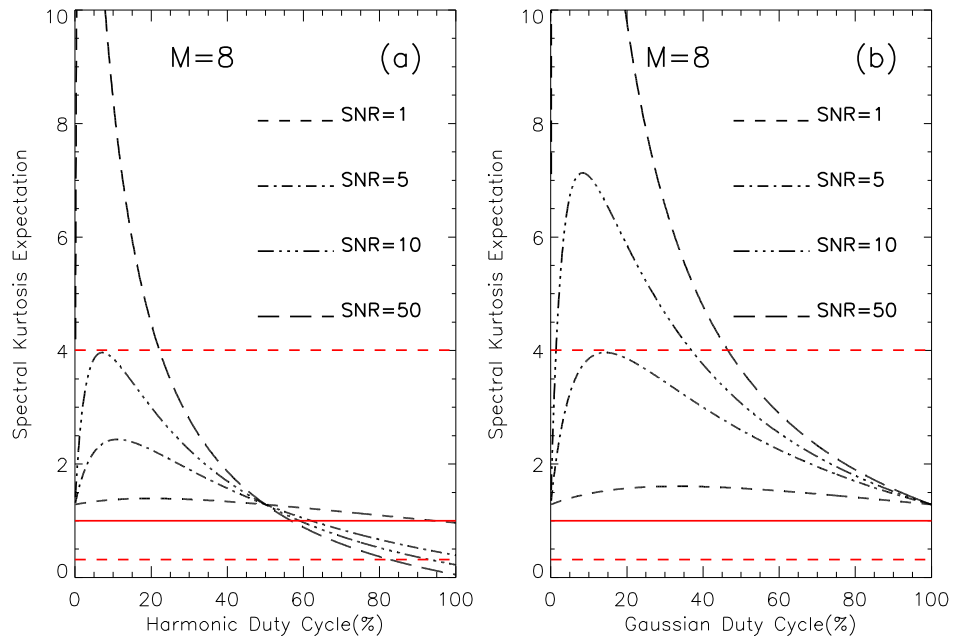


**Figure 5.2** SK expectations as function of duty-cycle relative to the integration time for the case of a harmonic excitation, (a), and a stochastic excitation, (b), for different signal to noise ratios. The red horizontal line shows the unity SK expectation for a stationary stochastic excitation and the red dashed lines marks the 0.13% PFA thresholds in the case of  $M=8$  accumulated PSD estimates.

The theoretical SK expectations [89] as function of duty-cycle has been demonstrated in Figure 5.2 for different signal to noise ratios. Theoretical SK expectations can be defined as the ratio between the integrated time domain signal envelope and the area bounded between the minimum and maximum amplitude of the signal. According to Figure

5.2, in the case illustrated here which is sum of only  $M=8$  consecutive PSD estimates, it can be concluded that the ability of the SK estimator to discriminate various types of spectral components is limited to relatively high SNR and duty-cycle harmonic system responses. Hence, the SK estimator is potentially more efficient in detecting harmonic or stochastic transients. Moreover, where similar plots are shown for  $M=1000$  it has been illustrated that with the accumulation numbers, the efficiency of the SK estimator increases [89].

### **5.5.2 The Experimental Data Set**

To better serve the purpose of this study, which is to provide a proof of concept for the applicability of the methods it proposes, dynamic response of the concrete box bridge due to different moving truck load scenarios and El-Centro earthquake as illustrated in Section 2.4 has been analyzed which thus allows immediate comparison between undamaged and damaged bridge.

However, the Data from Dynamic Analysis of the bridge using Lusas Bridge software contains only pure oscillation of the structure without any background noise, which is not identical to a real dataset collected from sensors. Thus, to demonstrate the full potential of the SK analysis, results presented in this section are based on a hybrid simulation in which, the original data streams were digitally mixed with two computer generated narrow band harmonic signals. For instance, Figure 5.3 presents the data obtained from dynamic analysis without any background noise, and Figure 5.4 shows the data in the presence of added noise based on the above mentioned assumption. It is worth noticing that without noise, the SK estimator is flat but well above unity, while in the

presence of added noise, SK deviates from unity only in the low frequency region, where the eigenfrequencies are located.

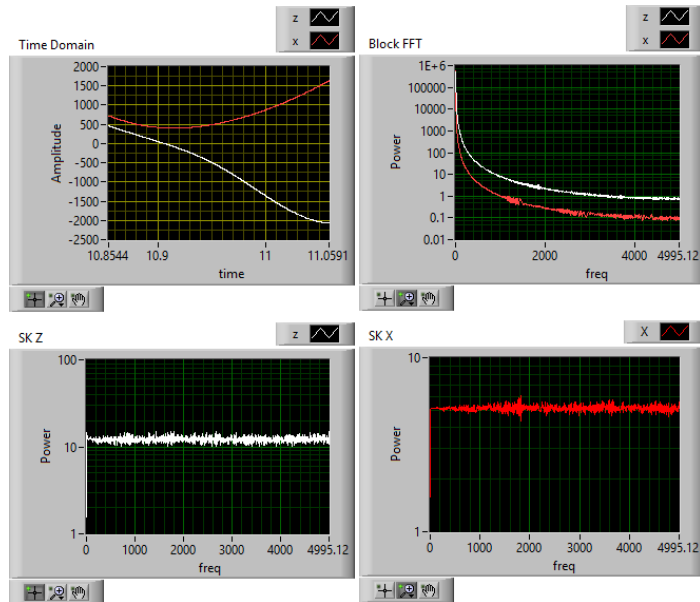


**Figure 5.3** Data set without background noise.

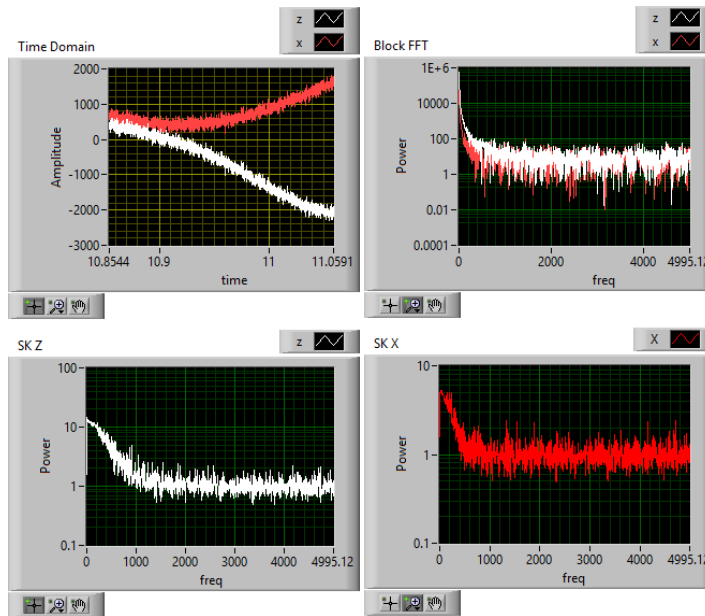


**Figure 5.4** Data in the presence of added noise.

In the next step of analysis, the data generated from moving truck over the bridge with the speed of 54 kph has been used. The data spans a time segment of only about 12

seconds, corresponding to the duration of the truck movement. This time interval is not satisfactory for the type of analysis done on the proposed algorithm with respect to the stated natural modal frequencies of the bridge. High time resolution of the data sets a large observational bandwidth (0-5000Hz) while the fundamental modes of the system are confined in the (0-50)Hz, a bandwidth for which an acquisition interval of  $dt=0.01$  seconds (100 samples per seconds=100Hz) is needed. However, with such sampling rate, the entire data set would provide only about 1200 time samples, which are appropriate for producing one single PSD estimate with a frequency resolution of about 0.1Hz (1024 samples needed) or 4 PSD estimates with about 0.4Hz resolution (256 samples needed for each), this number is insufficient for a potent Spectral Kurtosis statistics. The decimated time series (0.01s resolution) and corresponding PSD for 1024 samples without damage is shown in Figure 5.5 and with damage is shown in Figure 5.6 noting that 0.1% Gaussian white noise has been added to the original data.

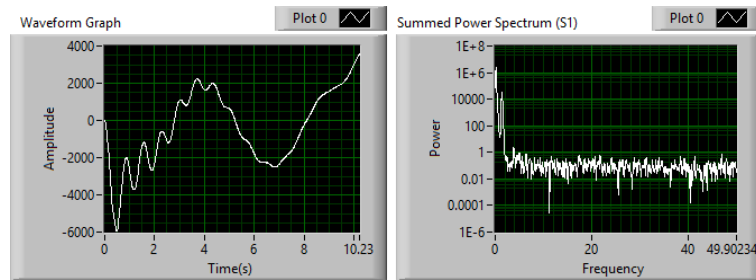


**Figure 5.5** Decimated time series and corresponding PSD for 1024 samples without damage.

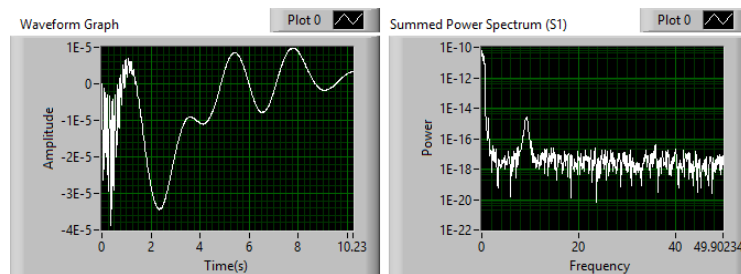


**Figure 5.6** Decimated time series and corresponding PSD for 1024 samples with damage.

By comparing the data with and without damage, It can be noticed that the damage introduces a distinct PSD peak around 10Hz. when building the SK estimator out of only 4 PSD blocks available, the noise fluctuations are reduced at the expense of reduced frequency resolution. However, the change in both spectrum and SK are visible from no damage to damage (see Figure 5.7). Since the SK statistics is based on only 4 PSD samples, the advantage of SK analysis over classical spectrum analysis is not clearly shown.

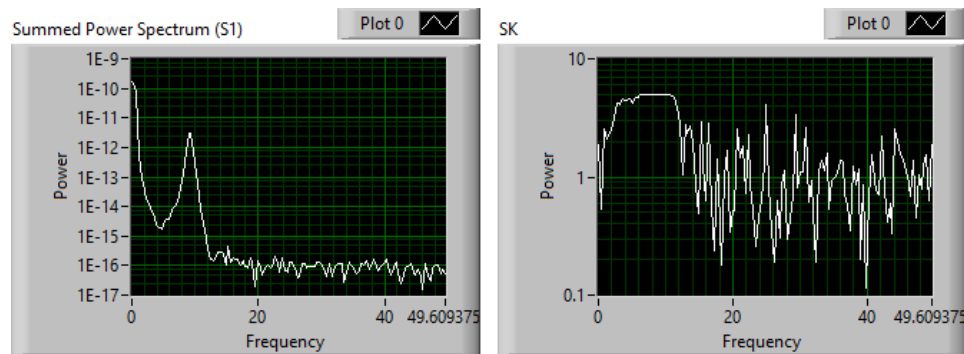


**Figure 5.7** Damaged detected using both SK analysis and classical spectrum analysis.

The SK-S1 diagram without and with damage has been presented in Figure 5.8. Although, they look different, no clear conclusion can be made due to the absence of a reasonable statistics and time history. As a result, a longer time series of data with 10ms resolution is used in order to build enough SD consecutive blocks to improve statistics and build a time history.

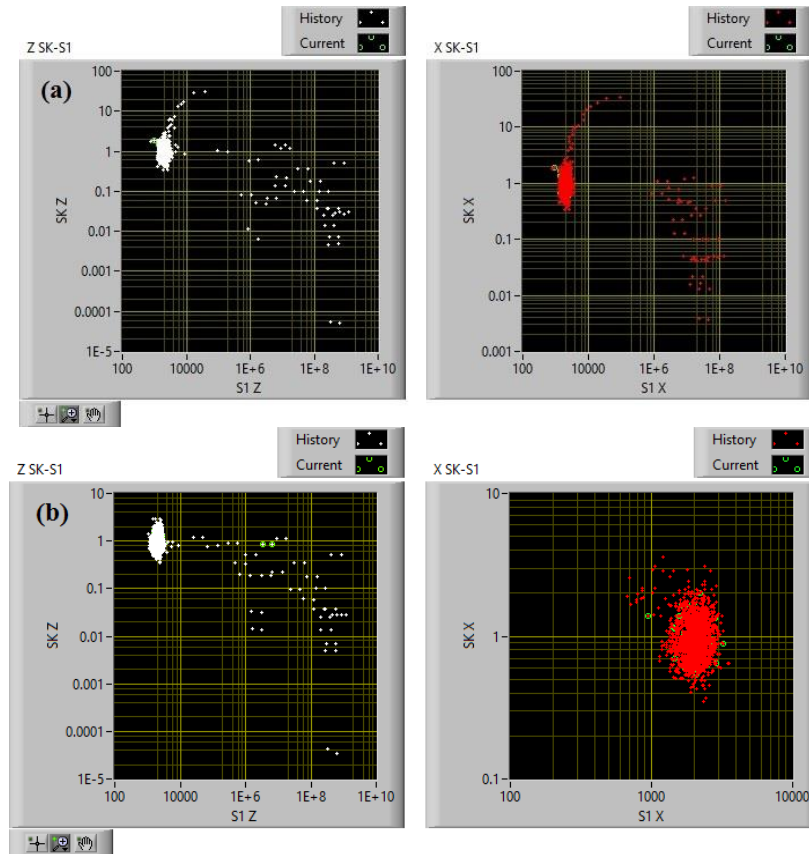


**Figure 5.8** SK-S1 diagram without(a) and with damage(b) based on the bridge dynamic response in X and Z directions.

For this purpose, SK analysis has been carried out on the data obtained from the dynamic response of the bridge under Moving truck with the speed of 1.125 m/s (or 4 kph) which provides 160 seconds time series of data and under El-Centro earthquake which provides 60 seconds time series of data (see Section 2.4 for the dynamic analysis details). Figure 5.9 presents the data obtained from the moving truck scenario with the speed of 1.125 m/s (or 4 kph) on both damaged and undamaged bridge. Figure 5.10 shows the data obtained from response of the bridge due to El-Centro earthquake ground motion. In above mentioned loading scenarios, the data from bridge without any defects shows larger deviation from  $SK=1$ , which are not observed in the data of the bridge with defect as expected. Utilizing these two longer time series of data from the bridge with and without

defect couldn't provide a convincing proof of concept for the applicability of the proposed method. This might be due to the following reasons:

- Location and type of structural damage chosen might not have a detectable effect on modal parameters of the bridge.
- Dynamic Analysis of the bridge using Lusas Bridge software contains only pure oscillation of the structure without any background noise, which is not identical to a real dataset.
- IMD plus Moving Load Analysis instead of actually simulating excited oscillations just provides static displacements for subsequent positions of a truck load.

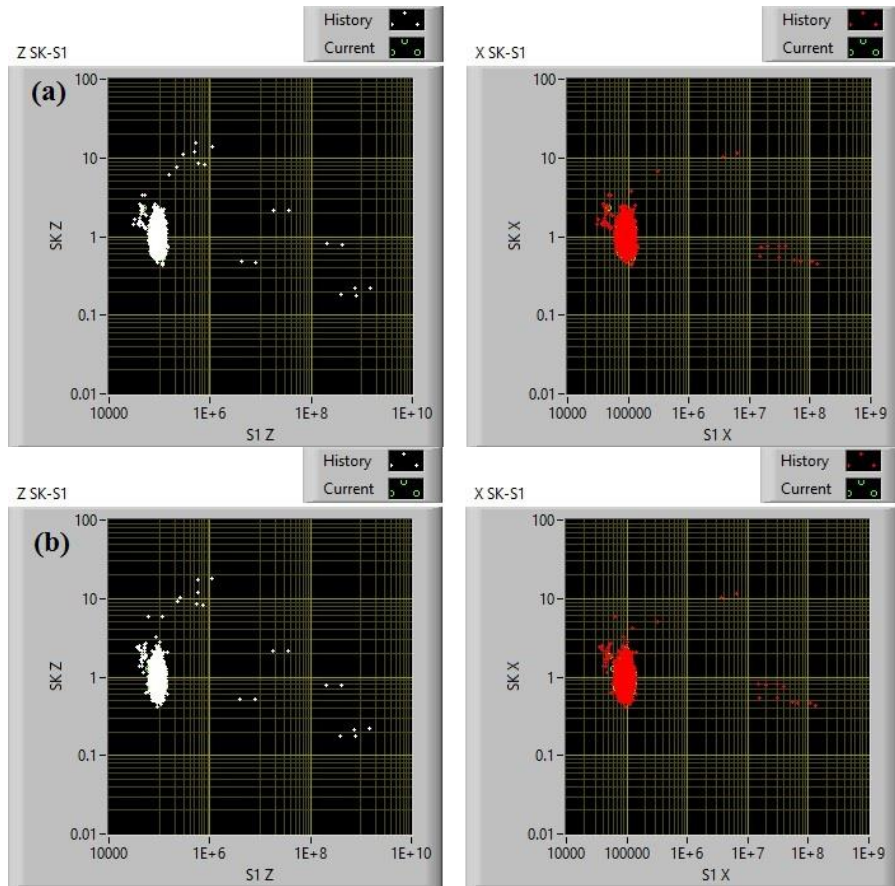


**Figure 5.9** SK-S1 diagram without(a) and with damage(b) based on the bridge dynamic response due to the moving truck in X and Z directions.

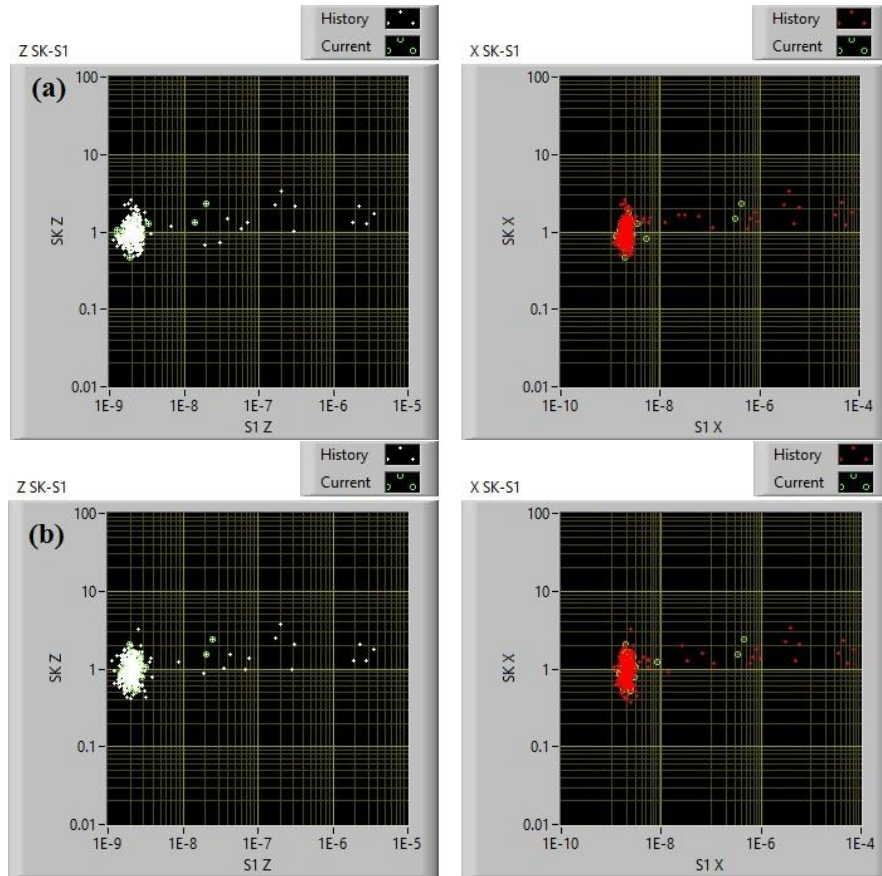


**Figure 5.10** SK-S1 diagram without(a) and with damage(b) based on the bridge dynamic response due to El-Centro earthquake in X and Z directions.

Thus, in order to better serve the purpose of this study and provide a cogent proof of concept for the applicability of the methods it proposes, a publicly available data set, (see acknowledgements section), has been used which thus allows immediate comparison with previously published results based on the same dataset [90, 91]. The data set refers to a suspended flexible steel structure and consists of a set of simultaneous measurements acquired on 30 parallel channels, out of which the first two represent the recorded input time series (8523 data samples per channel, 1024Hz acquisition rate) of two white noise shakers simultaneously used to excite the structure, while the rest of data channels represent the acceleration response of 28 distributed sensors. The particular choice of this



experimental data set was motivated by the fact that it contains not only the records of the response sensors, but also the input forces, and thus allows an immediate comparison of the modal parameters derived from the output only method presented in this study with the original state-space parameter estimation performed by [91] on the same data set.

### 5.5.3 Data Analysis

In the first stage of the data analysis, each data channel has been divided in  $M=8$  contiguous time domain blocks ( $N=1024$  data samples each) and, by means of a Hanning windowed FFT, produced  $M=8$  PSD estimates for each channel, and built the accumulated spectra,  $S_1$ , the accumulated squared power,  $S_2$ , and the Spectral Kurtosis estimator, SK, according to Equation (5.40). As an experimental validation of the theoretical expectations presented in the previous section, the accumulated power spectra (top panel) and the SK estimators (bottom panel) corresponding to the input force time series are shown in Figure 5.11.

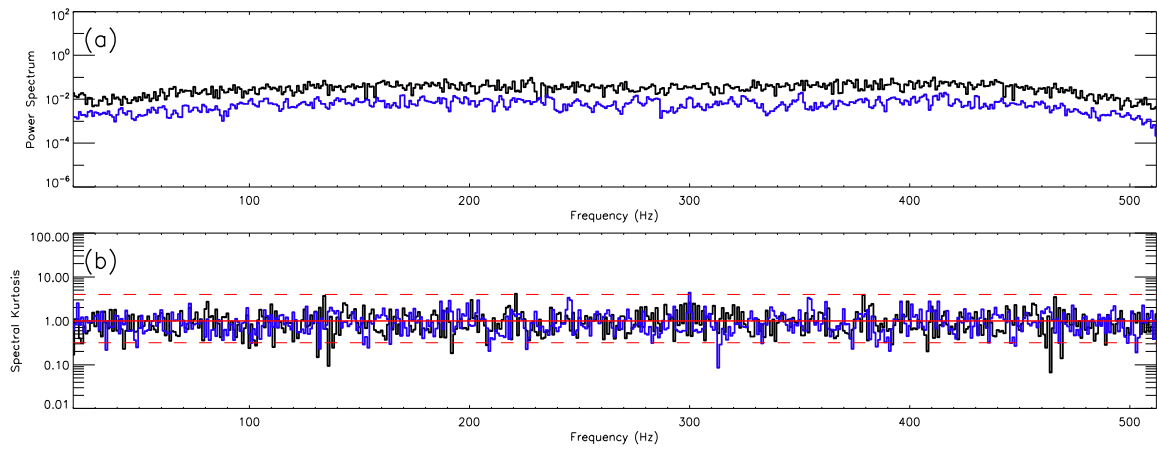


**Figure 5.11** Top panel: Accumulated FFT power spectra over  $M=8$  consecutive contiguous time blocks corresponding to the two input force data channels. Bottom panel: SK estimators corresponding to the same data channels. The red horizontal line shows the unity expectation for the K estimator, and the two horizontal red dashed lines indicate the standard  $M=8$  lower (0.318) and upper (4.005) SK thresholds (0.13% probability of false alarm) computed using the Pearson Type III approximation provided by Equation(5.42).

The top panel plots shows that the power spectra of the two input channels are featureless, while the bottom panel plots confirms the stochastic nature of the input forces by showing that, indeed, their associated SK estimators are bounded, in the limit of the expected statistical fluctuations, by the lower and upper theoretical SK thresholds corresponding to  $M=8$ . In contrast, the upper panel of Figure 5.12 shows that the accumulated PSD spectra for the first two response channels present different degrees of excitation of individual oscillation modes, which more or less overlapped.

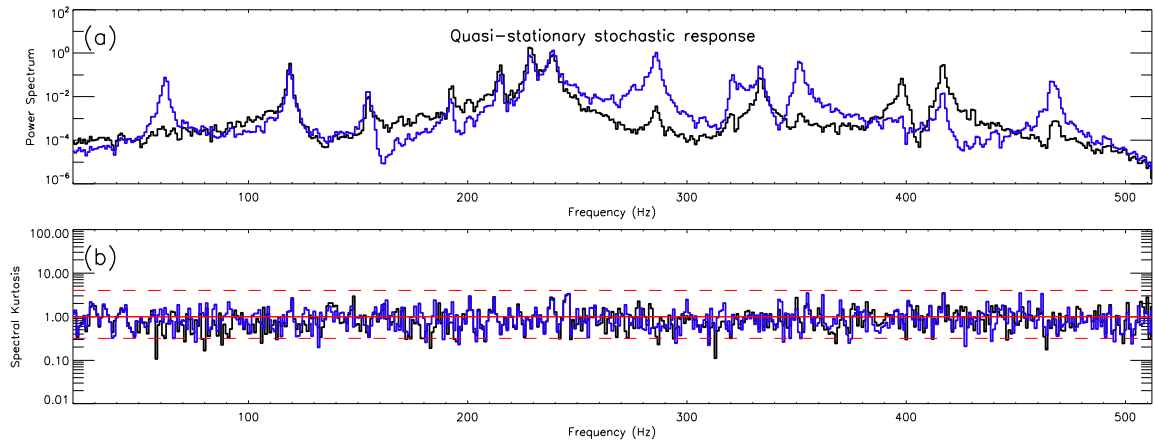


**Figure 5.12** Top panel: Accumulated FFT power spectra over  $M=8$  consecutive contiguous time blocks corresponding to the first two response data channels, channel 1 (black solid line), and channel 2 (blue solid line). Bottom panel: SK estimators corresponding to the same data channels. The red horizontal line shows the unity expectation for the  $K$  estimator, and the two horizontal red dashed lines indicate the standard  $M=8$  lower (0.318) and upper (4.005) SK thresholds (0.13% probability of false alarm) computed using the Pearson Type III approximation provided by Equation(5.42).

However, the plots shown in the bottom panel of Figure 5.12 reveal that, in the limit of the same expected statistical fluctuations, no spectral peak is associated with a statistical significant deviation of the SK estimator from the unity value expected in the case of a Gaussian time domain oscillations.

Thus, it can be concluded that the analyzed data set corresponds to a purely stochastic response of the system, which is consistent with the stochastic nature of the input

forces used to excite the system. It is also worth noting that the SK estimator provides straightforward and theoretically objective means to validate the stochastic nature of a system response without any need to make assumptions about the unknown statistical nature of the driving forces, which would not have been possible limiting the analysis to the first order statistics spectral description of the data provided by the PSD estimate alone [92].

However, due to the pure statistical nature of this particular data set to demonstrate the full potential of the SK analysis, the subsequent results has been presented based on a hybrid simulation in which, the original experimental data streams were digitally mixed with two computer generated narrow band harmonic signals. Therefore, a quasi-stationary harmonic response characterized by a relatively slow exponential decay (0.85% duty-cycle) and harmonic transient response characterized by a relatively fast exponential decay (0.11% duty-cycle) have been simulated.

The result of the SK analysis shown in bottom panel of Figure 5.13, which is consistent with the theoretical expectations presented in Figure 5.2, fully demonstrates the ability of the SK estimator objectively discriminate the deterministic or non-stationary system responses, performance that could not have been achieved solely based on the analysis of the spectral peaks present in the upper panel accumulated spectral power plots.

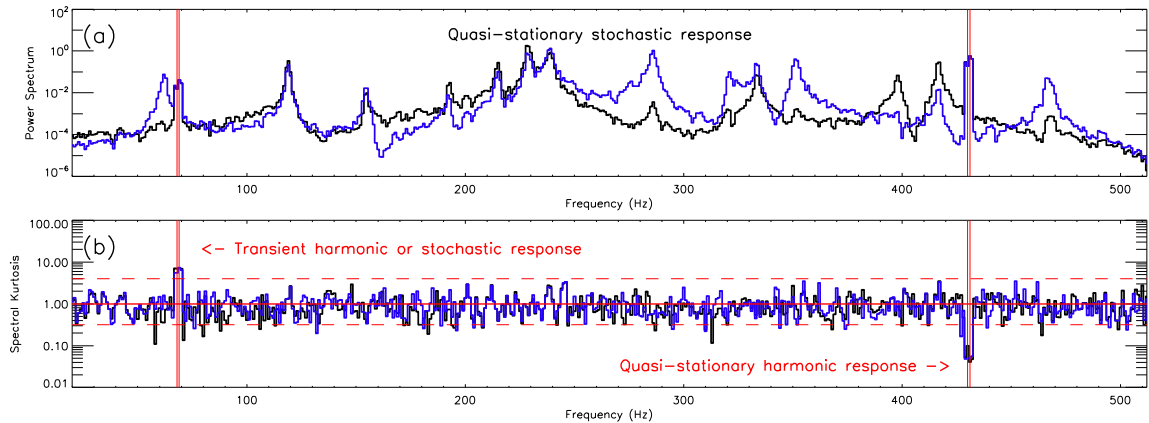


**Figure 5.13** Automatic harmonic line identification-Upper panel: Accumulated FFT power spectra over  $M=8$  consecutive contiguous time blocks corresponding to channel 1 (black) and channel 2 (blue). The red vertical lines indicate the frequency channels flagged by the Spectral Kurtosis analysis illustrated in panel (b). Bottom panel: Spectral Kurtosis estimators corresponding to the two channels shown in the upper panel. The SK expectation value of unity corresponding to a Gaussian input is shown by the red horizontal line. The two horizontal dashed lines represent the standard lower (0.318) and upper (4.005) SK thresholds (0.13% probability of false alarm) corresponding to an accumulation length  $M=8$ . The red vertical lines flag the frequency channels at which the SK thresholds are crossed by all 28 data channels.

In conclusion, the higher order spectral analysis involving the SK estimator is a more direct and computationally efficient alternative to discriminate deterministic or non-stationary stochastic signals than other available statistical methods routinely employed in operational modal analysis, such as time kurtosis analysis involving narrow bandwidth filter bank channelization, or EFDD methods involving inverse FFT as, for example, described in [93]. However, for the reader interested in applying an exclusive time domain modal analysis method in which automatic detection of non-Gaussian signals is pursued, we refer to [94] where equivalent theoretical formulae involving the computation of theoretical time domain detection thresholds of desired PFA are provided.

Nevertheless, one more practical aspect that one may consider when adopting one method or another is that the SK definition given by Equation (5.40) is naturally compatible with a data flowing computational paradigm and thus an SK flagging algorithm is

conceptually simple to be embedded in processors capable of real-time blind detection of harmonic response and damage detection [88].

## **5.6 A Maximum Likelihood Curve Fitting Method for Frequency Domain Decomposition**

### **5.6.1 Theoretical Background**

In this section, a new curve fitting maximum likelihood method will be demonstrated. In which, the statistical nature of statistical fluctuations that affect power spectra obtained by FFT has been taken into consideration. This method provides more reliable and accurate means for mode identification and estimation of modal parameters in operational modal analysis.

The proposed method first has been theoretically developed for the purpose of automatic decomposition of astronomical radio spectra as a linear superposition of an unknown number of overlapping individual spectral spikes which assumed to have Gaussian bell shapes [95]. It is based on the assumption that the FFT of response signal to stochastic excitation is a superposition of decaying resonant modal contributions. Consequently, the Gaussian superposition has been replaced with a linear superposition of  $n$  partially overlapping Lorentz spectral peaks in the original spectral decomposition algorithm development [95].

$$s_k = s_0 + \sum_{i=1}^n a_i \left[ 1 + \left( \frac{f_k - b_i}{c_i} \right)^2 \right]^{-1} \quad (5.43)$$

being  $S_0$  the background noise level,  $n$  the number of spectra peaks,  $a_i$ ,  $b_i$  and  $c_i$  the Lorentzian parameters which are unknown and have to be determined in order to obtain accurate estimates of the number of fundamental modes and their characteristic parameters,  $f_{0i} = \sqrt{b_i^2 + c_i^2}$  the natural mode frequencies, , and  $\xi_i = 1/\sqrt{1 + (b_i/c_i)^2}$  the relative damping ratios.

An original statistical estimator has been introduced in order to find a Maximum Likelihood solution of such frequency domain decomposition problem, which is called Sample to Model Ratio (SMR) [95]. For every frequency  $f_k$  , it is defined as the ratio between the accumulated power  $S_k$ , and the yet to be determined most likely spectral model  $s_k$ , as follows:

$$\rho_k = S_k / s_k \quad (5.44)$$

In the case of the true spectral model, and assuming that time domain noise normally distributed, the SMR estimator is expected to fluctuate around unity since a

probability distribution function found to be a gamma distribution of unit mean and  $1/M$  variance,

$$G(\rho_k) = M^M e^{-M\rho_k} \rho_k^{M-1} \Gamma(M)^{-1} \quad (5.45)$$

which provides the probabilities to observe a local SMR deviations above the mean,  $p_a = \text{prob}(\rho_k > 1)$ , and below the mean  $p_b = \text{prob}(\rho_k < 1)$ ,

$$p_a = \gamma(M, M) [\Gamma(M)]^{-1}; \quad p_b = 1 - \gamma(M, M) [\Gamma(M)]^{-1} \quad (5.46)$$

The Maximum Likelihood solution for the unknown set of free parameters may be obtained by minimizing the negative Log Likelihood function:

$$\lambda(s_0, a_{1..N}, b_{1..N}, c_{1..N}) = 2M \sum_{k=1}^N \{ S_k / s_k + \text{Ln}(s_k) - (1 - 1/M) \text{Ln}(S_k) \} \quad (5.47)$$

and the goodness of fit may be estimated by evaluating a ChiSq-like estimator associated with the  $\nu$  degrees of freedom of the minimization problem (number of frequency bins minus number of free model parameters):

$$\chi_\nu^2 = M \frac{1}{N} \sum_{k=1}^N (1 - \rho_k)^2 \quad (5.48)$$

The goodness of fit estimator defined by Equation (5.48) has a probability to be equal or larger than the observed one given by:

$$p(\chi_\nu^2) = \gamma\left(\frac{M}{M+3}, \frac{\nu}{2}, \frac{M}{M+3} \frac{\nu}{2} \chi_\nu^2\right) \left[ \Gamma\left(\frac{M}{M+3} \frac{\nu}{2}\right) \right]^{-1} \quad (5.49)$$

which reduces to a standard ChiSq probability only in the limit of a large  $M$ .

To address the well-known problem of computational sensitivity of the ML minimization problem relative to the initial conditions, a more robust standard least-square fit in a first stage can be performed using the statistically justified weights  $w_k = (M+1)/S_k^2$ , followed by a second stage ML minimization of Equation (5.47). However, it is necessary to estimate the true number of individual modes  $n$  in order to have a well-stated ML problem which is also a free parameter that has to be determined from



the data. As an alternative to the peak-picking method, which is biased in principle and not well-suited for an automated frequency domain decomposition algorithm, an additional statistical estimator,  $\eta_a$ , defined as the mean of a given number of systematic SMR deviations. In a compact region of the observed spectrum, SMR deviations are all above unity and situation that may indicate a missing peak in the model function used to fit the spectrum [95]. Hence, if the true number of spectral peaks is correctly estimated, there is practically a null probability for such compact regions to deviate from unity more than a hard limit that can be expressed solely in terms of the accumulation length  $M$  and the number of spectral points belonging to such region [92].

### **5.6.2 Algorithm Implementation and Validation**

To demonstrate the suitability of the curve fitting algorithm described above for operational modal analysis, the same division of the 28 response data channels in  $M$  contiguous time domain blocks has been used, and built the  $28 \times 28$  accumulated cross-correlation matrix associated with the response data channels. Following a standard FDD approach [96], the singular value decomposition (SVD) of the cross-correlation matrix was performed, and thus 28 SVD spectra was obtained, those being associated with the largest 6 SVD values being shown on the top panel of Figure 5.14, which indicate that the dominant SVD spectrum (thick black line) contains all spectral peaks visible on least one of the channel-based power spectra like those displayed in Figure 5.11 (a).

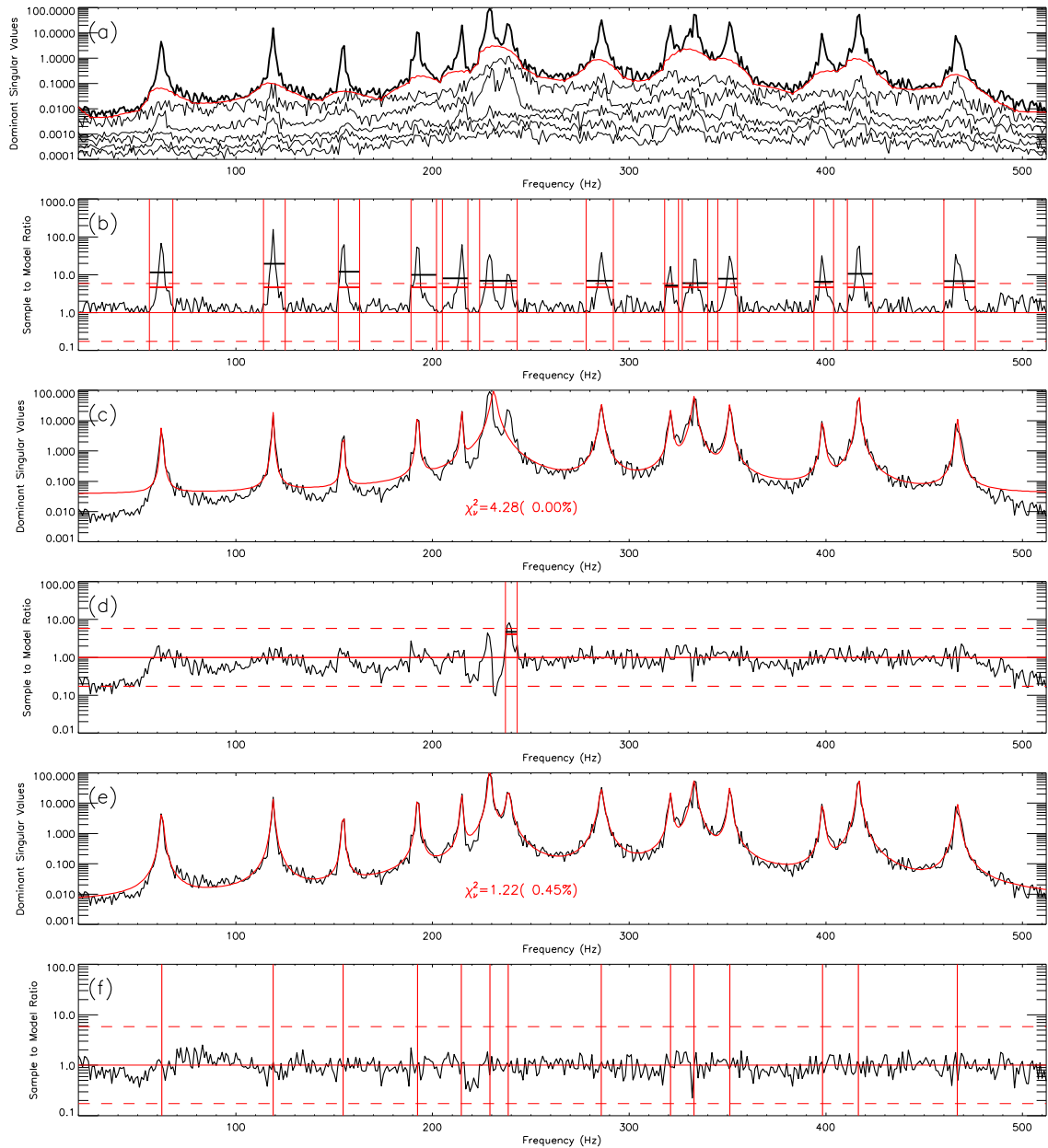


**Figure 5.14** Illustration of the automated ML FDD algorithm steps. Panel (a) The dominant SVD spectrum (thick black line), its base envelope (red solid line), and the next 6 SVD spectra (black thin line). Panel (b): the SMR deviations corresponding to the base envelope model. A number of 13 compact regions (bounded vertical red lines) found to have mean SMR deviations (black segments) larger than the 0%PFA limits (red horizontal segments). Panel (c): ML solution corresponding to the 13 peak model suggested by the initial SMR analysis. The goodness of fit value and its associated probability are indicated in the figure inset. Panel (d): SMR deviations corresponding to the 13 peaks model suggesting the location of a missing peak. Panel (e): Final ML solution corresponding to the 14 peak model. The goodness of fit value and its associated probability are indicated in the figure inset. Panel (f) the final SMR spectrum showing that all deviations around unity are bounded by the 0% PFA limits (red dashed horizontal lines, also show in panel (c) corresponding to a single SMR deviation above or below unity. The red vertical lines indicate the location of the location of the spectral peaks.

In the next step of analysis, the dominant SVD spectrum has been divided by the lower spectral envelope (red solid line), which is considered as the first order approximation of the spectral model, and produce the SMR spectrum shown on Figure 5.14 panel (b). The SMR spectrum is then used to automatically flag 13 distinct compact regions (delimited by vertical red lines) for which the averaged SMR deviations (horizontal black solid segments) were found to be larger than the 0%PFA limits (horizontal red solid segments), which were computed for  $M=8$  and their lengths  $l$  (according to the formulae provided by [95]). The lower and upper  $\sim 0\%$  PFA limits for any single SMR deviation (region of  $l=1$ ) are indicated for reference by dashed horizontal red lines in Figure 5.14 (b). By visual comparison of Figure 5.14 (a) and (b) it can be noticed that 12 of the 14 SVD peaks are clearly associated with a distinct SMR compact region, except for two partially overlapped peaks around 230Hz, which consistently correspond to the same compact SMR region.

In the next step of the algorithm, a model function comprising a flat  $s_0$  background and 13 peaks (Equation (5.43)) is constructed, the initial Lorentzian guess parameters are set to values consistent with the SMR regions, and the minimization of log-likelihood function defined by Equation (5.47) is performed in order to obtain the ML solution (red continuous line) illustrated in of Figure 5.14(c). In the plot inset we show the associated goodness of fit estimator  $\chi_v^2 = 4.28$ , which correspond to a 0% probability to observe a larger value for the existent model, which is an indication of a poor fit, conclusion consistent with the fact that the automatically generated 13 peaks spectral model actually missed one of the true peaks of the SVD spectrum.

In the next step of the algorithm a new SMR spectrum, shown in Figure 5.14(d), is constructed by dividing the SVD spectrum by the 13 peaks ML solution and one missing peak is automatically identified at the correct location, as marked by the two vertical lines. As a consequence, the spectral model is amended by adding the missing peak and a new log-likelihood minimization is performed to derive the solution shown in Figure 5.14(e). As expected, the new solution is characterized by a smaller goodness of fit value,  $\chi_v^2 = 1.22$ , which, according to Equation (5.49) correspond to a 0.45% probability to observe a larger deviation for the same model and another realization of the noise fluctuations.

As a final validation of the algorithm, we display in Figure 5.14(f) the final SMR spectrum showing that all deviations around unity are bounded by the 0% PFA limits (red dashed horizontal lines) corresponding to a single SMR deviation above or below unity.

For a quantitative assessment, the ML modal parameters, i.e. the natural frequencies and relative damping ratios, are displayed in Table 5.1, where they are compared with original modal parameters derived from the same data set by using a Multivariable Subspace Identification (MOESP) estimation method involving both the input and output channels [90].

The quantitative comparison with the references values shows an excellent agreement in terms of natural frequency estimations (less than 1% relative difference), while the relative damping ratios disagree more, with a general trend of the ML damping ratios being overestimated relative to the MOESP values. The ML method, however, fails to resolve the 156.45 Hz mode, which may be just an intrinsic limitation of any OMA method lacking full information about the true input forces.

**Table 5.1** Comparison Between the Modal Parameters Estimated by Maximum-Likelihood Fit of the Dominant Singular Value Decomposition Spectrum with the Original State-space Estimates Obtained by [90].

	Natural Frequency Estimates (Hz)			Damping Ratio Estimates (%)		
	Reference	ML fit	Relative difference (%)	Reference	ML fit	Relative difference (%)
1	62.22	62.36	0.23	0.67	0.92	38.00
2	118.90	118.90	0.00	0.20	0.44	118.54
3	154.49	154.53	0.03	0.08	0.15	81.93
	<b>156.45</b>			<b>0.25</b>		
4	192.44	192.45	0.01	0.22	0.22	-1.57
5	214.94	214.68	-0.12	0.23	0.17	-26.87
6	229.35	229.11	-0.11	0.11	0.27	145.64
7	239.33	238.54	-0.33	0.26	0.47	81.74
8	286.79	285.84	-0.33	0.19	0.35	84.44
9	321.14	321.00	-0.04	0.15	0.20	36.15
10	333.98	332.96	-0.31	0.24	0.33	35.96
11	352.33	351.24	-0.31	0.26	0.19	-27.54
12	398.18	398.36	0.05	0.17	0.16	-8.34
13	417.59	416.63	-0.23	0.13	0.16	23.84
14	467.49	466.92	-0.12	0.16	0.19	16.23

Note: The outlined row corresponds to a spectral mode not resolved by the ML fitting method.

## 5.7 Conclusions

Experimental methods based on modal analysis under ambient vibrational excitation are often employed to detect structural damages of mechanical systems. An extensive literature review has been crucial for the identification of effective procedures of operational modal analysis. The mathematical background and the main characteristics of the methods have been deeply discussed in this chapter. Many of the frequency domain methods, such as

Basic Frequency Domain (BFD), Frequency Domain Decomposition (FFD), or Enhanced Frequency Domain Decomposition (EFFD), use as first step a Fast Fourier Transform (FFT) estimate of the power spectral density (PSD) associated with the response of the system. In this chapter, it is shown that higher order statistical estimators such as Spectral Kurtosis (SK) and Sample to Model Ratio (SMR) can be successfully employed not only to more reliably discriminate the response of the system against the ambient noise fluctuations, but also to better identify and separate contributions from closely spaced individual modes. Moreover, it is shown that a SMR-based Maximum Likelihood curve fitting algorithm improve the accuracy of the spectral shape and location of the individual modes and, when combined with the SK analysis, it provides efficient means to categorize such individual spectral components according to their temporal dynamics as harmonic or stochastic system responses to unknown ambient excitations.

## CHAPTER 6

### CONCLUSIONS AND FUTURE WORK

#### 6.1 Conclusions

Structural Health Monitoring, damage detection and localization of bridges using Wireless Sensor Networks (WSN) are studied in this thesis. This research is motivated by the need to improve the efficiency and accuracy of the current highway bridge inspection and maintenance practice. The application of SHM on bridge structures will enable the condition of the bridge to be constantly monitored and prevent unnecessary costly and emergent maintenance. To this end, wireless monitoring systems provide a new approach and enhance the use of current SMH systems by maximizing the lifetime of the system, the accuracy of the sensed data, and the system reliability, and minimizing the system cost.

An extensive literature review of Structural Health Monitoring, Vibration-Based Damaged Detection techniques and Operational Modal Analysis is first provided. By comparing the relative merits and shortcomings of the various methods proposed to date, promising techniques and areas that need further research are identified.

Finite Element Analysis (FEA) has been carried out using LUSAS Bridge Plus software to simulate the behavior of a scaled down reinforced concrete frame, 3-span bridge and an in-service 6-span precast segmental box girder bridge. Model development for each structure is demonstrated. Element types used in the models are covered along with the constitutive assumptions and parameters for the various materials in each section. Besides, Geometry of the models, loading and boundary conditions are illustrated. The mode shapes obtained from eigenvalue frequency analysis are presented. For the 3-span bridge Moving Load analysis has been carried out using the IMDPlus facility and Seismic

Response of the bridge under El Centro earthquake ground motion is presented. Furthermore, Static and Dynamic Finite Element analysis of the 6-Span Precast Segmental Box Girder Bridge has been carried out. Finite Element Analysis results for each model thoroughly demonstrated in each section. The Finite Element Analysis performed in this chapter is employed in the next chapters.

A preliminary study in designing and setting up a test-bed for the research on SHM of bridges utilizing Wireless Sensor Networks is presented in chapter 3. The test-bed encompasses the physical model and FE model of a scaled down reinforced concrete frame from chapter 2. The design and setup of the physical model are presented in detail. The reinforced concrete frame was excited by sine excitation using the shaking table at six different frequencies and the time history data were measured using five MEMS accelerometers with the help of wireless sensing system. To show overall data quality of the measured acceleration, a sample time histories of 15 seconds are provided. It is concluded from the plot results that the developed wireless sensing system is capable of measuring the dynamic response of the RC frame structure with reliable precision level.

Designing a SHM system is a systematic work integrating various expertise. In chapter 4, first the design criteria of SHM for a large-scale bridge is outlined. The commonly used types of sensory systems is then introduced. As a new and potentially promising sensing, transmission and monitoring system method, wireless monitoring is specially described in this chapter. Moreover, design and realization of power harvesting and power usage optimization for self-sustainable operation of SMH monitoring systems using wireless sensor networks is briefly discussed. Finally, the long-term Structural Health Monitoring System using Wireless Sensor Networks (WSNs) for the in-service



highway bridge is introduced. The results obtained from the FEA has been utilized to determine sensor locations and measurement types and could effectively minimize the number of sensors, data for transmission, and volume of data for processing.

Experimental methods based on modal analysis under ambient vibrational excitation are often employed to detect structural damages of mechanical systems.. Many of the frequency domain methods, such as Basic Frequency Domain (BFD), Frequency Domain Decomposition (FFD), or Enhanced Frequency Domain Decomposition (EFFD), use as first step a Fast Fourier Transform (FFT) estimate of the power spectral density (PSD) associated with the response of the system. In chapter 5, it is shown that higher order statistical estimators such as Spectral Kurtosis (SK) and Sample to Model Ratio (SMR) can be successfully employed not only to more reliably discriminate the response of the system against the ambient noise fluctuations, but also to better identify and separate contributions from closely spaced individual modes. Moreover, it is shown that a SMR-based Maximum Likelihood curve fitting algorithm improve the accuracy of the spectral shape and location of the individual modes and, when combined with the SK analysis, it provides efficient means to categorize such individual spectral components according to their temporal dynamics as harmonic or stochastic system responses to unknown ambient excitations.

## **6.2 Recommendations for Future Work**

This study has demonstrated the potential of using wireless sensor technology for long term and real-time structural health monitoring and post-event damage detection. Meanwhile, this study also identified key issues and tasks, as listed below, that must be addressed before the proposed damage detection algorithm and wireless monitoring system can be applied

to the new stadium that State of Qatar will build in preparation for the 2022 World Cup. The research on structural health monitoring using WSNs, damage identification and sensor placement process is still a novel field of study, especially for long term monitoring of bridges. Based on the research in this study, the following tasks and topics are recommended for future work:

- Validating the accuracy of results obtained from Finite Element Analysis of the RC frame by using lab-scale experimental results.
- Identifying modal parameters of the frame such as: natural frequencies, modal shapes and damping ratios.
- Improving the initial FE model utilizing Finite Element Model updating techniques.
- Development of different type of damage cases in the form of saw cuts perpendicular to the longitudinal axis of the beam. Comparing modal test results of the damaged frames to the updated FE model for the subsequent studies of damage detection.
- Deployment of proposed Structural Health Monitoring system using Wireless Sensor Networks on the in-service highway bridge located in Qatar and Identifying modal parameters of the bridge.
- Applying the proposed damage detection and localization technique proposed in this study to the in-service highway bridge for long term monitoring.
- Performing FE model updating to provide the basis for the future use of the updated model to predict the capacity and remaining life of the aforementioned bridge.

## APPENDIX A

### CONSTRUCTION OF REINFORCED CONCRETE FRAME

The RC frame used for all the lab experiments mentioned above was constructed at University of Qatar. The pictures below show the step by step building of the frame from assembling the form-work to curing. The frame was cast and cured under standard conditions. It was design to have dimension to match the test bed of shaking table along with frame legs to be able to fix it on the shaking table. The frame was cured in a steam room 28 days after pouring.

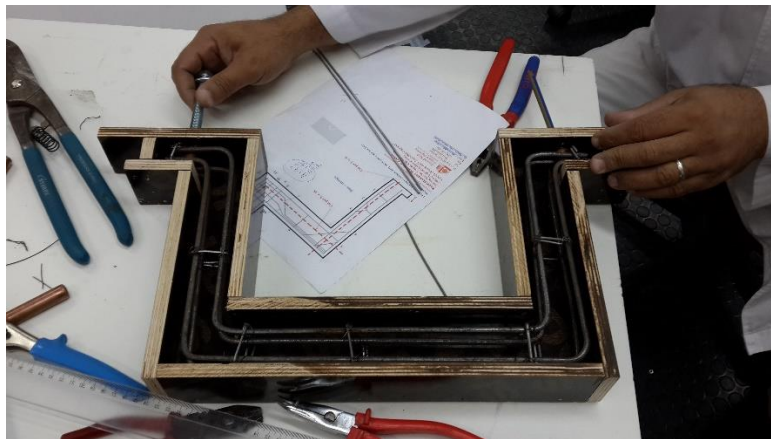


**Figure A.1** Reinforcement assembly.



**Figure A.2** The wood works and reinforcement for the RC frame.



**Figure A.3** Preparation of the concrete.



**Figure A.4** Pouring the concrete.



**Figure A.5** Curing of the frame.

## APPENDIX B

### CHARACTERISTICS OF THE IRIS MOTE PLATFORMS AND THE MEASUREMENT SENSORS EMBEDDED IN THE MTS400 CROSSBOW BOARD

**Table B.1** Technical Specifications of the IRIS mote platforms

Processor/Radio	XM2110CA	Remarks
CPU	ATmega1281	
Program Flash Memory	128 KB	
Measurement (Serial) Flash	512 KB	
RAM	8KB	
Analog to Digital Converter	10 bit ADC	8 channel, 0-3V input
Processor current draw	8mA	Active Mode
	$< 8\mu\text{A}$	Sleep Mode
Radio frequency band	2405 MHz to 2480 MHz	
Transmit (TX) data rate	250 kbps	
Radio frequency power	3 dBm (typ)	
Radio current draw	16 mA	Receive
Radio Range	300m	
Power	2AA batteries	
External power	2.7 – 3.3V	
Size (in)	2.25 x 1.25 x 0.25	Excluding battery pack
(mm)	58 x 32 x 7	Excluding battery pack
Weight (oz)	0.7	Excluding batteries
(grams)	18	Excluding batteries

**Table B.2** Characteristics of the Humidity and Temperature Sensor

Sensor Type	Sensirion SHT11	
Channels	Humidity	Temperature
Range	0 to 100%	-40°C to 80°C
Accuracy	±3.5% RH (typical)	±0.5°C
Operating Range	3.6 to 2.4 volts	
Interface	Digital Interface	

**Table B.3** Characteristics of the Barometric Pressure and Temperature Sensor

Sensor Type	Intersema MS5534	
Channels	Pressure	Temperature
Range	300 to 110 mbar	-10°C to 60°C
Accuracy	±3.5%	±0.5°C
Operating Range	3.6 to 2.4 volts	
Interface	Digital Interface	

**Table B.4** Characteristics of the Light Sensor

Sensor Type	Taos TSL2550
Channels	Light
Range	400 – 1000 nm
Operating Range	3.6 to 2.7 volts
Interface	Digital Interface

**Table B.5** Characteristics of the Accelerometer Sensor

Sensor Type	Analog Devices ADXL202JE
Channels	X (ADC1), Y (ADC2)
Range	$\pm 2g$
Sensitivity	167 mV/g, $\pm 17\%$
Resolution	2mg (0.002g) RMS
Offset	$V_{Battery}/2 \pm 0.4V$
Operating Range	3.6 to 3.0 volts
Interface	Analog Interface

## APPENDIX C

### 1940 EL CENTRO EARTHQUAKE RECORD

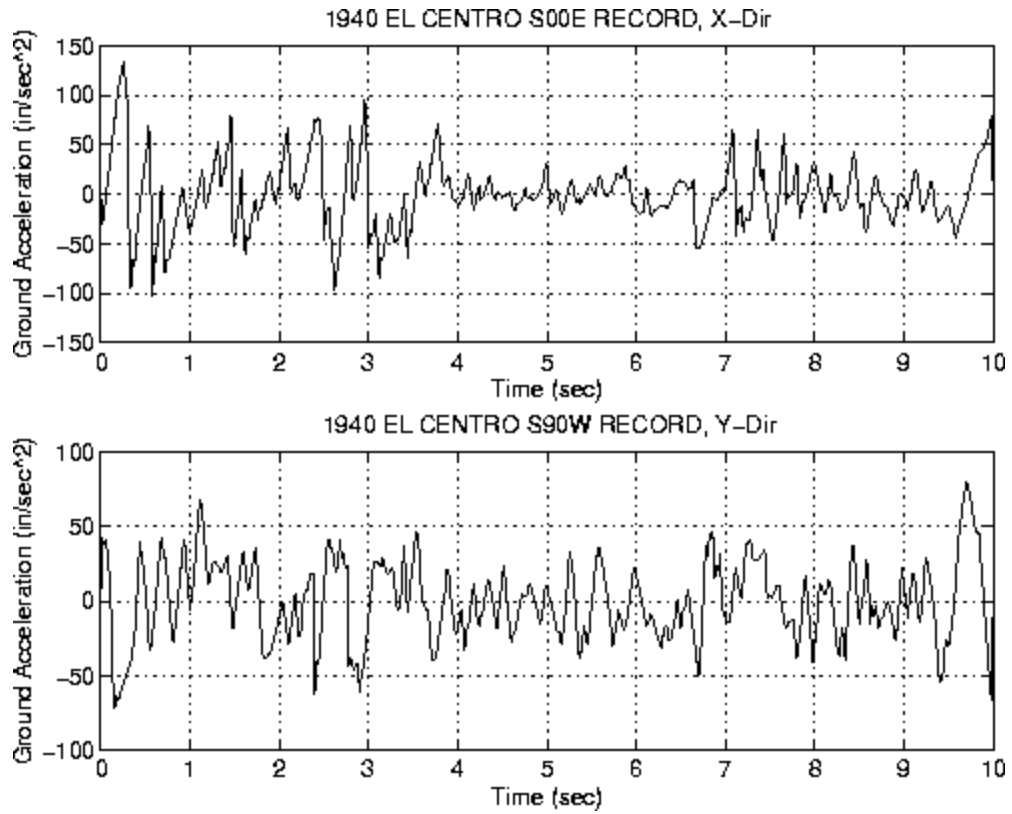


**Figure C.1** Ten second sample of the ground motion accelerograms extracted from the 1940 El Centro record.



## REFERENCES

- [1] S. B. CHASE and J. A. LAMAN, "Dynamics and Field Testing of Bridges," 2000.
- [2] "Report Card for America's Infrastructure," American Society of Civil Engineers, <http://www.infrastructurereportcard.org/bridges/2013>.
- [3] FHWA, National Bridge Inventory (NBI), <http://www.fhwa.dot.gov/bridge/nbi/defbr11.cfm2011>.
- [4] NBIS, "National Bridge Inspection Standards, Code of Federal Regulations," *U.S. Government Printing Office via GPO Access*, 2015.
- [5] M. Moore, D. Rolander, B. Graybeal, B. Phares, and G. Washer, "Highway bridge inspection: State-of-the-Practice Study," *Federal Highway Administration, ed., Department of Transportation*, 2001.
- [6] M. Moore, B. M. Phares, B. Graybeal, D. Rolander, and G. Washer, "Reliability of visual inspection for highway bridges, volume I: Final report," 2001.
- [7] S. Chase, "The Role of Sensing and Measurement in Achieving FHWA'S Strategic Vision for Highway Infrastructure," in *Sensing Issues in Civil Structural Health Monitoring*, F. Ansari, Ed., ed: Springer Netherlands, 2005, pp. 23-32.
- [8] C. R. Farrar and K. Worden, "An introduction to structural health monitoring," *Philosophical Transactions of the Royal Society A: Mathematical, Physical and Engineering Sciences*, vol. 365, pp. 303-315, 2007.

- [9] B. F. Spencer Jr and S. Cho, "Wireless smart sensor technology for monitoring civil infrastructure: technological developments and full-scale applications," in *Proceedings of World Congress on Advances in Structural Engineering and Mechanics, Seoul, Korea, 2011*, pp. 18-23.
- [10] S. W. Doebling, C. R. Farrar, M. B. Prime, and D. W. Shevitz, "Damage Identification and Health Monitoring of Structural and Mechanical Systems from Changes in Their Vibration Characteristics: A Literature Review," Los Alamos National Laboratory LA-13070-MS, 1996.
- [11] H. Sohn, C. R. Farrar, F. M. Hemez, D. D. Shunk, D. W. Stinemates, B. R. Nadler, *et al.*, *A review of structural health monitoring literature: 1996-2001*: Los Alamos National Laboratory Los Alamos, NM, 2004.
- [12] D. J. Ewins, *Modal testing: theory, practice and application* vol. 2.
- [13] C. Rainieri and G. Fabbrocino, *Operational Modal Analysis of Civil Engineering Structures*: Springer, 2014.
- [14] E. Parloo, P. Verboven, P. Guillaume, and M. Van Overmeire, "Force identification by means of in-operation modal models," *Journal of Sound and Vibration*, vol. 262, pp. 161-173, 2003.
- [15] C. R. Farrar and K. Worden, *Structural health monitoring: a machine learning perspective*: John Wiley & Sons, 2012.
- [16] A. Deraemaeker, E. Reynders, G. De Roeck, and J. Kullaa, "Vibration-based structural health monitoring using output-only measurements under changing environment," *Mechanical systems and signal processing*, vol. 22, pp. 34-56, 2008.
- [17] F. Magalhães, A. Cunha, and E. Caetano, "Vibration based structural health monitoring of an arch bridge: from automated OMA to damage detection," *Mechanical Systems and Signal Processing*, vol. 28, pp. 212-228, 2012.

- [18] "LUSAS Bridge Case Studies," <http://www.lusas.com/case/bridge/index.html>, Sept. 25, 2014.
- [19] K.-J. Bathe, *Finite element procedures*: Klaus-Jurgen Bathe, 2006.
- [20] S. P. Shah, *Fracture mechanics of concrete: applications of fracture mechanics to concrete, rock and other quasi-brittle materials*: John Wiley & Sons, 1995.
- [21] M. Bangash, "Concrete and concrete structures: numerical modelling and applications," 1989.
- [22] "Crossbow Wireless Sensors Network," <http://www.moog-crossbow.com>, Apr. 1, 2015.
- [23] J. M. Brownjohn and T.-C. Pan, "Identifying loading and response mechanisms from ten years of performance monitoring of a tall building," *Journal of performance of constructed facilities*, vol. 22, pp. 24-34, 2008.
- [24] L. Sun, Z. Sun, D. Dan, and Q. Zhang, "Large-span bridge and their health monitoring systems in China," in *Proceeding of 2007 International Symposium on Integrated Life-Cycle Design and Management of Infrastructure*, 2007, pp. 79-95.
- [25] J. Ko and Y. Ni, "Technology developments in structural health monitoring of large-scale bridges," *Engineering structures*, vol. 27, pp. 1715-1725, 2005.
- [26] S.-P. Chang, J. Yee, and J. Lee, "Necessity of the bridge health monitoring system to mitigate natural and man-made disasters," *Structure and Infrastructure Engineering*, vol. 5, pp. 173-197, 2009.
- [27] Y. Ni, K. Wong, and Y. Xia, "Health checks through landmark bridges to sky-high structures," *Advances in Structural Engineering*, vol. 14, pp. 103-119, 2011.
- [28] Y. Xia, Y. q. Ni, P. Zhang, W. y. Liao, and J. m. Ko, "Stress development of a supertall structure during construction: Field monitoring and numerical analysis,"

*Computer-Aided Civil and Infrastructure Engineering*, vol. 26, pp. 542-559, 2011.

- [29] A. E. Aktan, F. N. Catbas, K. A. Grimmelsman, and M. Pervizpour, "Development of a model health monitoring guide for major bridges," *Report submitted to: Federal Highway Administration Research and Development*, 2002.
- [30] B. Hofmann-Wellenhof, H. Lichtenegger, and J. Collins, *Global positioning system: theory and practice*: Springer Science & Business Media, 2012.
- [31] J. R. Casas and P. J. Cruz, "Fiber optic sensors for bridge monitoring," *Journal of Bridge Engineering*, vol. 8, pp. 362-373, 2003.
- [32] J. M. Seim, E. Udd, W. L. Schulz, and H. M. Laylor, "Health monitoring of an Oregon historical bridge with fiber grating strain sensors," in *1999 Symposium on Smart Structures and Materials*, 1999, pp. 128-134.
- [33] Y. Ni, Y. Xia, W. Liao, and J. Ko, "Technology innovation in developing the structural health monitoring system for Guangzhou New TV Tower," *Structural Control and Health Monitoring*, vol. 16, pp. 73-98, 2009.
- [34] T. S. Austin, M. M. Singh, P. J. Gregson, J. P. Dakin, and P. M. Powell, "Damage assessment in hybrid laminates using an array of embedded fiber optic sensors," in *1999 Symposium on Smart Structures and Materials*, 1999, pp. 281-288.
- [35] E. I. Cohen, S. A. Mastro, C. P. Nemarich, J. F. Korczynski Jr, A. W. Jarrett, and W. C. Jones, "Recent developments in the use of plastic optical fiber for an embedded wear sensor," in *1999 Symposium on Smart Structures and Materials*, 1999, pp. 256-267.
- [36] Y.-L. Lo and F.-Y. Shaw, "Development of corrosion sensors using a single-pitch Bragg grating fiber with temperature compensations," in *5th Annual International Symposium on Smart Structures and Materials*, 1998, pp. 64-72.
- [37] S. Vurpillot, N. Casanova, D. Inaudi, and P. Kronenberg, "Bridge spatial displacement monitoring with 100 fiber optic deformation sensors: Sensors

network and preliminary results," in *Smart Structures and Materials' 97*, 1997, pp. 51-57.

- [38] A. Stewart, G. Carman, and L. Richards, "Health monitoring technique for composite materials utilizing embedded thermal fiber optic sensors," *Journal of composite materials*, vol. 39, pp. 199-213, 2005.
- [39] R. Sun, Z. Sun, and L. Sun, "Design and performance tests of a FBG-based accelerometer for Structural Vibration Monitoring," in *The Proceeding of 4th China-Japan-US Symposium on Structural Control and Monitoring*, 2006.
- [40] Y. L. Xu and Y. Xia, *Structural health monitoring of long-span suspension bridges*: CRC Press, 2011.
- [41] K. RHKJM and K. Pister, "Mobile networking for smart dust," in *ACM/IEEE International Conference on Mobile Computing and Networking (MobiCom 99)*, Seattle, 1999.
- [42] R. M. Kling, "Intel mote: an enhanced sensor network node," in *Int'l Workshop on Advanced Sensors, Structural Health Monitoring, and Smart Structures*, 2003, pp. 12-17.
- [43] R. M. Kling, "Intel motes: advanced sensor network platforms and applications," in *Microwave Symposium Digest, 2005 IEEE MTT-S International*, 2005, p. 4 pp.
- [44] I. F. Akyildiz, W. Su, Y. Sankarasubramaniam, and E. Cayirci, "Wireless sensor networks: a survey," *Computer networks*, vol. 38, pp. 393-422, 2002.
- [45] J. Yick, B. Mukherjee, and D. Ghosal, "Wireless sensor network survey," *Computer networks*, vol. 52, pp. 2292-2330, 2008.
- [46] B. Spencer, "A study on building risk monitoring using wireless sensor network MICA mote," in *First International Conference on Structural Health Monitoring and Intelligent Infrastructure, Japan*, 2003, pp. 353-363.

- [47] M. Ruiz-Sandoval, T. Nagayama, and B. Spencer Jr, "Sensor development using Berkeley Mote platform," *Journal of Earthquake Engineering*, vol. 10, pp. 289-309, 2006.
- [48] J. A. Rice and B. Spencer Jr, "Structural health monitoring sensor development for the Imote2 platform," in *The 15th International Symposium on: Smart Structures and Materials & Nondestructive Evaluation and Health Monitoring*, 2008, pp. 693234-693234-12.
- [49] J. P. Lynch, K. H. Law, A. S. Kiremidjian, T. W. Kenny, E. Carryer, and A. Partridge, "The design of a wireless sensing unit for structural health monitoring," in *Proceedings of the 3rd International Workshop on Structural Health Monitoring*, 2001, pp. 12-14.
- [50] J. P. Lynch, A. Sundararajan, K. H. Law, A. S. Kiremidjian, T. W. Kenny, and E. Carryer, "Computational core design of a wireless structural health monitoring system," *Proceedings of Advances in Structural Engineering and Mechanics (ASEM'02)*, pp. 21-23, 2002.
- [51] V. M. Karbhari and F. Ansari, *Structural health monitoring of civil infrastructure systems*: Elsevier, 2009.
- [52] S. Jang, H. Jo, S. Cho, K. Mechitov, J. A. Rice, S.-H. Sim, *et al.*, "Structural health monitoring of a cable-stayed bridge using smart sensor technology: deployment and evaluation," *Smart Structures and Systems*, vol. 6, pp. 439-459, 2010.
- [53] J. P. Lynch and K. J. Loh, "A summary review of wireless sensors and sensor networks for structural health monitoring," *Shock and Vibration Digest*, vol. 38, pp. 91-130, 2006.
- [54] Y. Gao and B. F. Spencer Jr, "Structural health monitoring strategies for smart sensor networks," Newmark Structural Engineering Laboratory. University of Illinois at Urbana-Champaign. 1940-9826, 2008.

- [55] R. Kling, R. Adler, J. Huang, V. Hummel, and L. Nachman, "Intel Mote-based sensor networks," *Structural Control and Health Monitoring*, vol. 12, pp. 469-479, 2005.
- [56] "ACTEL, Low-Power Flash FPGAs Handbook Igloo Handbook," [http://www.actel.com/documents/IGLOO\\_HB.pdf](http://www.actel.com/documents/IGLOO_HB.pdf), 2009.
- [57] S. Roundy, B. P. Otis, Y.-H. Chee, J. M. Rabaey, and P. Wright, "A 1.9 GHz RF transmit beacon using environmentally scavenged energy," *optimization*, vol. 4, p. 4, 2003.
- [58] J. M. Brownjohn, "Assessment of structural integrity by dynamic measurements," University of Bristol, 1988.
- [59] F. Benedettini, D. Zulli, and R. Alaggio, "Frequency-veering and mode hybridization in arch bridges," in *Proceedings of the 27th International Modal Analysis Conference*, 2009.
- [60] R. Cantieni, "Experimental methods used in system identification of civil engineering structures," in *Proceedings of the International Operational Modal Analysis Conference (IOMAC)*, 2005, pp. 249-260.
- [61] K. Thibert, C. E. Ventura, M. Turek, and S. Guerrero, "Dynamic soil-structure interaction study of a reinforced concrete high-rise building," in *Proceedings of the 2nd International Operational Modal Analysis Conference*, 2007.
- [62] Y. Tamura, A. Yoshida, L. Zhang, T. Ito, S. Nakata, and K. Sato, "Examples of modal identification of structures in Japan by FDD and MRD techniques," in *Proc 1st international operational modal analysis conference, Copenhagen*, 2005.
- [63] L. F. Ramos, L. Marques, P. B. Lourenço, G. De Roeck, A. Campos-Costa, and J. Roque, "Monitoring historical masonry structures with operational modal analysis: Two case studies," *Mechanical Systems and Signal Processing*, vol. 24, pp. 1291-1305, 2010.

- [64] R. Brincker, P. H. Kirkegaard, P. Andersen, and M. Martinez, "Damage detection in an offshore structure," Dept. of Building Technology and Structural Engineering, Aalborg University 1994.
- [65] L. B. Ibsen and M. Liingaard, "Output-only modal analysis used on new foundation concept for offshore wind turbine," in *The International Operational Modal Analysis Conference*, 2005.
- [66] M. Baptista and P. Mendes, "Use of Ambient Vibration Tests for Structural Identification: 3 Case Studies," in *1st International Operational Modal Analysis Conference*, 2005.
- [67] P. Reynolds, P. Mohanty, and A. Pavic, "Use of operational modal analysis on empty and occupied stadia structures," in *1st International Operational Modal Analysis Conference*, 2005.
- [68] S.-E. Rosenow, S. Uhlenbrock, and G. Schlottmann, "Parameter extraction of ship structures in presence of stochastic and harmonic excitations," in *Proceedings of International Operational Modal Analysis Conference, Copenhagen, Denmark*, 2007.
- [69] R. Brincker, P. Andersen, N. Møller, and H. Herlufsen, "Output-only Modal Testing of a car body subject to Engine Excitation," *Proc. of the 18th International Modal Analysis Conference, San Antonio, Texas*, 2000.
- [70] B. Peeters, J.-S. Servaye, and J. Cock, "Truck Applications of Operational Modal Analysis," *Proceedings of The 26th IMAC, Orlando, Florida, USA*, 2008.
- [71] N. Møller, R. Brincker, and P. Andersen, "Modal extraction on a diesel engine in operation," in *The International Modal Analysis Conference*, 2000, pp. 1845-1851.
- [72] T. Uhl, M. Petko, G. Karpiel, and A. Klepka, "Real time estimation of modal parameters and their quality assessment," *Shock and Vibration*, vol. 15, pp. 299-306, 2008.



- [73] J. S. Bendat and A. G. Piersol, *Random data: analysis and measurement procedures* vol. 729: John Wiley & Sons, 2011.
- [74] W. Heylen, S. Lammens, and P. Sas, *Modal Analysis Theory and Testing: Division of Production Engineering, Machine Design and Automation, Katholieke Universiteit Leuven*, 1994.
- [75] G. H. Golub and C. F. Van Loan, *Matrix computations* vol. 3: JHU Press, 2012.
- [76] J. C. Santamarina and D. Fratta, *Discrete signals and inverse problems: an introduction for engineers and scientists*: John Wiley & Sons, 2005.
- [77] J. S. Bendat and A. G. Piersol, "Engineering applications of correlation and spectral analysis," *New York, Wiley-Interscience, 1980. 315 p.*, vol. 1, 1980.
- [78] A. J. Felber, "Development of a hybrid bridge evaluation system," University of British Columbia, 1993.
- [79] B. Peeters, "System Identification and Damage Detection in Civil Engineering," 2000.
- [80] C. Rainieri, G. Fabbrocino, and E. Cosenza, "Some remarks on experimental estimation of damping for seismic design of civil constructions," *Shock and Vibration*, vol. 17, pp. 383-395, 2010.
- [81] C. Shih, Y. Tsuei, R. Allemang, and D. Brown, "Complex mode indication function and its applications to spatial domain parameter estimation," *Mechanical Systems and Signal Processing*, vol. 2, pp. 367-377, 1988.
- [82] R. J. Allemang and D. L. Brown, *A Correlation Coefficient for Modal Vector Analysis*, 1982.
- [83] R. Brincker, L. Zhang, and P. Andersen, "Modal identification of output-only systems using frequency domain decomposition," *Smart materials and structures*, vol. 10, p. 441, 2001.

- [84] S. Gade, N. Møller, H. Herlufsen, and H. Konstantin-Hansen, "Frequency domain techniques for operational modal analysis," in *Proceedings 1st IOMAC Conference*, 2005, pp. 26-27.
- [85] J. Rodrigues, R. Brincker, and P. Andersen, "Improvement of frequency domain output-only modal identification from the application of the random decrement technique," in *Proc. 23rd Int. Modal Analysis Conference, Dearborn, MI*, 2004.
- [86] N.-J. Jacobsen, P. Andersen, and R. Brincker, "Applications of frequency domain curve-fitting in the EFDD technique," in *Proceedings IMAC XXVI Conference*, 2008.
- [87] R. Brincker and L. Zhang, "Frequency domain decomposition revisited," in *Proceedings of the third international operational modal analysis conference. Porto Novo*, 2009.
- [88] G. M. Nita and D. E. Gary, "Statistics of the spectral kurtosis estimator," *Statistics*, vol. 122, pp. 595-607, 2010.
- [89] G. M. Nita, D. E. Gary, Z. Liu, G. J. Hurford, and S. M. White, "Radio Frequency Interference Excision Using Spectral-Domain Statistics," *Publications of the Astronomical Society of the Pacific*, vol. 119, pp. 805-827, 2007.
- [90] M. Abdelghani, C. T. CHOU, and M. Verhaegen, "Using subspace methods in the identification and modal analysis of structures," in *Proceedings of SPIE, the International Society for Optical Engineering*, 1997, pp. 1392-1398.
- [91] M. Abdelghani, M. Basseville, and A. Benveniste, "In-operation damage monitoring and diagnostics of vibrating structures, with applications to offshore structures and rotating machinery," in *Proceedings of SPIE, the International Society for Optical Engineering*, 1997, pp. 1815-1821.
- [92] G. M. Nita, M. Mahgoub, S. Sharyatpanahi, N. Cretu, and T. M. El-Fouly, "Higher Order Statistical Frequency Domain Decomposition for Operational Modal Analysis," presented at the 7th International Conference on Structural Health Monitoring of Intelligent Infrastructure, 2015.

- [93] N.-J. Jacobsen, P. Andersen, and R. Brincker, "Eliminating the influence of harmonic components in operational modal analysis," in *Proceedings IMAC XXV Conference*, 2007.
- [94] G. M. Nita and D. E. Gary, "The generalized spectral kurtosis estimator," *Monthly Notices of the Royal Astronomical Society: Letters*, vol. 406, pp. L60-L64, 2010.
- [95] G. M. Nita, G. D. Fleishman, D. E. Gary, W. Marin, and K. Boone, "Fitting FFT-derived Spectra: Theory, Tool, and Application to Solar Radio Spike Decomposition," *The Astrophysical Journal*, vol. 789, p. 152, 2014.
- [96] R. Brincker, L. Zhang, and P. Andersen, "Modal identification from ambient responses using frequency domain decomposition," in *Proc. of the 18<sup>th</sup> International Modal Analysis Conference (IMAC), San Antonio, Texas*, 2000.